Investigation of a superthermal ultracold neutron source based on a solid deuterium converter for the TRIGA Mainz reactor

Dissertation
zur Erlangung des Grades
"Doktor der Naturwissenschaften"
im Promotionsfach Kernchemie

am Fachbereich Chemie, Pharmazie und Geowissenschaften
der Johannes Gutenberg-Universität Mainz

vorgelegt von
Dipl.-Phys. Thorsten Lauer
aus Ellerstadt

Mainz, 2010

Yes We Can

In remembrance of my grandfather

R.Lauer

Abstract

Research in fundamental physics with the free neutron is one of the key tools for testing the Standard Model at low energies. Most prominent goals in this field are the search for a neutron electric dipole moment (EDM) and the measurement of the neutron lifetime. Significant improvements of the experimental performance using ultracold neutrons (UCN) require reduction of both systematic and statistical errors. The development and construction of new UCN sources based on the superthermal concept is therefore an important step for the success of future fundamental physics with ultracold neutrons. Significant enhancement of today available UCN densities strongly correlates with an efficient use of an UCN converter material. The UCN converter here is to be understood as a medium which reduces the velocity of cold neutrons (CN, velocity of about 600 m/s) to the velocity of UCN (velocity of about 6 m/s).
Several big research centers around the world are presently planning or constructing new superthermal UCN sources, which are mainly based on the use of either solid deuterium or superfluid helium as UCN converter.
Thanks to the idea of Yu.Pokotilovsky, there exists the opportunity to build competitive UCN sources also at small research reactors of the TRIGA type. Of course these smaller facilities don't promise high UCN densities of several 1000 UCN/cm^3, but they are able to provide densities around 100 UCN/cm^3 for experiments.
In the context of this thesis, it was possible to demonstrate succesfully the feasibility of a superthermal UCN source at the tangential beamport C of the research reactor TRIGA Mainz. Based on a prototype for the future UCN source at the Forschungs-Neutronenquelle Heinz Maier-Leibnitz (FRMII) in munich, which was planned and built in collaboration with the Technical University of Munich, further investigations and improvements were done and are presented in this thesis.
In parallel, a second UCN source for the radial beamport D was designed and built. The comissioning of this new source is foreseen in spring 2010. At beamport D with its higher thermal neutron flux, it should be possible to increase the available UCN densities of 4 UCN/cm^3 by minimum one order of magnitude.

In parallel to the source developement at beamport D and to the characterisation of the solid deuterium converter, the existing and upgraded UCN source was used for the investigation of new neutron optical devices and the development of new materials based on enriched ^{11}B for fundamental physics with ultracold neutrons. These new materials show high neutron optical potentials of more than 308 neV and may be, due to their low absorption a breakthrough in UCN transport and storage. Their use in fundamental neutron physics can increase significantly the performances of upcoming experiments like the EDM experiments, e.g., the n2EDM experiment currently under construction at the Paul Scherrer Institute (PSI).

Zusammenfassung

Das freie Neutron ist eines der Schlüsselwerkzeuge für den Test des Standard Models bei niedrigsten Energien. Die Suche nach einem Elektrischen Dipolmoment (EDM) des Neutrons und die Messung der Neutronenlebensdauer stehen hierbei an erster Stelle. Beide Experimente bedienen sich der Speicherung von ultrakalten Neutronen (UCN) und sind mittlerweile an ihren systematischen und statistischen Grenzen angelangt. Die Entwicklung und der Aufbau neuartiger UCN Quellen, basierend auf dem superthermischen Prinzip, ist deshalb ein bedeutender Schritt für den weiteren Erfolg der Grundlagen Forschung mit ultrakalten Neutronen.
Eine deutliche Steigerung der heute erreichbaren UCN Dichten ist vor allem von der Wahl eines geeigneten UCN Konverter-Materials abhängig. Unter dem Begriff des UCN Konverters verbirgt sich die Eigenschaft einer Substanz, kalte Neutronen mit einer Geschwindigkeit von rund 600 m/s auf eine Geschwindigkeit von 6 m/s abzubremsen. Mehrere große Forschungzentren weltweit befinden sich zum jetzigen Zeitpunkt in Planung oder im Bau neuer UCN Quellen, die hauptsächlich auf der Verwendung von festem Deuterium oder superflüssigem Helium als zukünftigem Konverter Material basieren. Dank der Ideen von Yu. Pokotilovsky gibt es jedoch die Möglichkeit, konkurenzfähige UCN Quellen auch an kleinen leistungsschwächeren Forschungsreaktoren vom Typ TRIGA aufzubauen. Diese kleineren UCN Quellen versprechen zwar nicht UCN Dichten von über 1000 UCN/cm^3, liefern jedoch mit Dichten von ca. 100 UCN/cm^3 eine gute Basis für fundamentale Experimente mit ultrakalten Neutronen.

Im Rahmen dieser Arbeit konnte die Machbarkeit einer superthermischen UCN Quelle am tangentialen Strahlrohr C des Forschungreaktor TRIGA in Mainz gezeigt werden. Ein mit der Technischen Universität München geplanter und aufgebauter Prototyp einer zukünftigen UCN Quelle an der Forschungs-Neutronenquelle Heinz Maier-Leibnitz (FRMII) diente hierbei als Grundlage für die in dieser Arbeit dargstellten Ergebnisse.
Unter Einbeziehung aller relevanten Daten wurde eine weitere UCN Quelle für das zur Zeit noch freie radiale Strahlrohr D aufgebaut, deren Inbetriebnahme zu Beginn des Jahres 2010 geplant ist. Auf Grund des höheren thermischen Neutronenflusses an Strahlrohr D, sollten aller Voraussicht nach die momentan zur Verfügung stehenden UCN Dichten von 4 UCN/cm^3 an Strahlrohr C um mindestens einen Faktor 10 an Strahlrohr D übertroffen werden können.

Parallel zur Entwicklung einer neuen UCN Quelle und zu der Charakterisierung von festem Deuterium als UCN Konverter, konnte der bestehende Prototyp zur Entwicklung neuer neutronenoptischer Komponenten und zur Entwicklung neuartiger UCN kompatibler Materialien basierend auf hochangereichertem ^{11}B genutzt werden. Diese neuen Materialien könnten dank ihres hohen neutronenoptischen Potentials von gemessenen 308 neV und ihrer geringen Absorption einen Durchbruch für die Speicherung und den Transport von ultrakalten Neutronen bedeuten. Zukünftige Experimente wie das neue n2EDM Experiment, das sich zur Zeit am Paul Scherrer Institut in der Aufbauphase befindet, werden ihre Effizienz mit Einsatz dieser Beschichtungen deutlich erhöhen.

Contents

List of Figures

List of Tables

Chapter 1

Introduction

In 1959, Zel'dovich predicted the possibility to store neutrons with very low kinetic energy in material bottles [1]. Such neutrons are known now as ultracold neutrons. In 1969, the existence of ultracold neutrons was succesfully proven with a storage experiment by a group of physicists at the Dubna research reactor [2].
Due to the long storage time which is close to the lifetime of the free neutron and the neutrons's electric neutrality, ultracold neutrons have been convenient tools for the investigation on the low energy fundamental physics since those days.
Starting from the vertical extraction of a few ultracold neutrons from the low energy tail of the neutron spectrum at research reactors like FRMI in Munich [3], the need for stronger UCN sources resulted in the realisation of two different ideas:

While Golub and Pendelbury proposed the idea of a so called superthermal UCN source based on superfluid helium [4], Steyerl invented and built a phase space transforming turbine [5], which is able to slow down neutrons from 100 m/s to the UCN region. The neutron turbine was later installed at the "niveau D " of the institute Laue Langevin in Grenoble [6], where up to now important flagship experiments on fundamental physics with ultracold neutrons are ongoing studying the properties of free neutron. These experiments are and were related with the search for an electric dipole moment of the neutron [7, 8], the measurement of the neutron lifetime with highest precision [9, 10], the neutron quantum levels in the earth gravitational field [11], and the dark matter search [12] to give some examples.
Besides the succesful and impressive start of the UCN turbine which got the standard tool for the production of ultracold neutrons, the idea of Golub and Pendelbury had a not promising prolongation due to technical problems of the UCN extraction from the superfluid helium converter volume.

Experiments like the search for an electric dipole moment of the free neutron are today not only limited by systematical effects, they are even stronger limited statistically due to low available UCN density.
For that reason, several institutes around the world took up the old ideas of Golub and Pendelbury and started to develop the "next generation" UCN sources which should be

capable to increase the available neutron densities by several orders of magnitude.
The most promising designs at PSI, FRMII, Los Alamos, and ILL are based on solid deuterium [13, 16, 14, 15] and superfluid helium [17, 18, 19] as UCN converters.
The main part of this PhD thesis deals with the investigation of solid deuterium as UCN converter, by using the existing prototype UCN source which is located at the tangential beamport C of the TRIGA Mainz reactor and the further development and installation of an upgraded UCN source at the radial beamport D. This new UCN source, which will start its operation in spring 2010, will be the work horse for the physics with ultracold neutrons at Mainz.
Chapter 2 will give a short overview on some basics going along with ultracold neutrons as well as their production.
The used prototype source, which was built in collaboration with the Department E18 of the Technical University of Munich, and the experimental results of the source parameters will be presented in chapter 3 and 4.
The concept and the design of the new inpile cryostat for beamport D will be explained in chapter 6.
Finally, chapter 7 reports about all ideas and developments, which were realized for the improvement of the source performance and creation of infrastructure for experiments at the pulsed UCN source at the TRIGA Mainz.

Chapter 2

Ultracold neutrons and ways to obtain them

2.1 Basics of ultracold neutrons

Neutrons are termed ultracold if their kinetic energy is small enough to be recflected under all angles of incidence from a material surface. Due to their neutrality, such neutrons are sensitive to almost all fundamental interactions. This property makes UCN an ideal tool to investigate all four fundamental forces with high precision.

Weak interaction

Within the frame of electroweak interaction, the decay of the neutron can be represented as transformation of one of its down quarks to anti-neutrino, electron, and up quark via exchange of a heavy vector boson of weak interaction. Finally this leads to the following reaction:

$$n \rightarrow p + e + \bar{\nu}_e + 783keV \tag{2.1}$$

The decay is theoretically described by the Standard Model of particle physics with semileptonic vector and axial vector currents implementing the following parameters: $|V_u d|$, the first element of the quark mixing matrix, which can be expressed as

$$|V_{ud}|^2 = \frac{K}{G^2{}_F \tau_n (1+3\lambda^2) f (1+RC)} = \frac{(4908.7 \pm 1.9)s}{\tau_n (1+3\lambda^2)} \tag{2.2}$$

and $\lambda = g_A/g_V$, the ratio of the current coupling strengths together with a time reversal violation phase Φ, G_F, the Fermi decay constant, known from muon decay and τ_n, the free neutron lifetime.

A proof of the assumptions from this model or extended new theories beyond the Standard Model always results in a test of the unitarity of the CKM matrix.

$$\begin{pmatrix} d' \\ s' \\ b' \end{pmatrix} = \begin{pmatrix} V_{ud} & V_{us} & V_{ub} \\ V_{cd} & V_{cs} & V_{cb} \\ V_{td} & V_{ts} & V_{tb} \end{pmatrix} \cdot \begin{pmatrix} d \\ s \\ b \end{pmatrix} \tag{2.3}$$

As expressed in eqn.2.2 besides the neutron lifetime also the ratio of the couplings has to be known. This value can be extracted from the probability distribution of the beta decay parameterized in terms of the neutron spin, the energy and momentum of the decay products:

$$W dE_e d\Omega_e d\Omega_\nu \sim p_e E_e (E_0 - E_e)^2 dE_e d\Omega_e d\Omega_\nu \times \left[1 + a\frac{\vec{p}_e\vec{p}_\nu}{E_e E_\nu} + b\frac{m_e}{E_e} + \langle\vec{\sigma}_n\rangle\left(A\frac{\vec{p}_e}{E_e} + B\frac{\vec{p}_\nu}{E_\nu} + D\frac{\vec{p}_e \times \vec{p}_\nu}{E_e E\nu}\right)\right]$$

In this equation the coefficients a, b, A, B, D are derived from experiments measuring correlations between the neutron spin and its decay products:

a	=	$\frac{1-\lvert\lambda\rvert^2}{1+3\lvert\lambda\rvert^2}$	=	-0.103 ± 0.0029	electron - antineutrino asymmetry
a	=	0	=	0	Fierz interference
A	=	$-2\frac{\lvert\lambda\rvert^2+\lvert\lambda\rvert\cos\Phi}{1+3\lvert\lambda\rvert^2}$	=	-0.1173 ± 0.0013	spin-electron asymmetry
B	=	$2\frac{\lvert\lambda\rvert^2-\lvert\lambda\rvert\cos\Phi}{1+3\lvert\lambda\rvert^2}$	=	-0.981 ± 0.004	spin-anti neutrino asymmetry
D	=	$\frac{\lvert\lambda\rvert\sin\Phi}{1+3\lvert\lambda\rvert^2}$	=	$-4 \pm 6 \cdot 10^{-4}$	T-odd triple-product

Table 2.1: Parametrization of the free neutron decay. Φ is the angle between the couplings g_A and g_V. Equations and values are taken from [20]

For the actual value with the highest accuracy, A, the ratio λ of the axial to the vector coupling constant can be derived as

$$\lambda = -1.2750 \pm 0.0009 \tag{2.4}$$

Together with the averaged neutron lifetime published by the Particle Data Group of

$$\bar{\tau}_n = 885.7 \pm 0.8 \ s \tag{2.5}$$

and the actual values for $|V_{us}|$ and $|V_{ub}|$ new limits for the violation of the CKM unitarity have been reported [21]

$$\Delta = |V_{ud}|^2 + |V_{us}|^2 + |V_{ub}|^2 - 1 = 0.0084 \pm 0.0028 \tag{2.6}$$

with a 3σ deviation from zero.

However, the most recent lifetime experiment published from Serebrov et.al. [10] with a deviation of six sigma from the PDG average value corrects this violation and give together with the shown values for A a proof of the unitarity.
That's why new measurements of the neutron lifetime with acurracies better than 1 s

are necessary, to clarify the present state of the art.

Gravitational interaction

Compared to the energies which play a mayor role in standard particle physics, the energy of ultracold neutrons is so small that gravity is a non negligible force. With a mass of $m_n = 1.67 \cdot 10^{-27} kg$ the potential of a neutron at a height h in the earth's gravitational field is given as

$$V_g = m_n \cdot g \cdot h \approx 102 \, (\frac{neV}{m}) \cdot h \tag{2.7}$$

where g≈9.81 m/s^2 is the gravitational acceleration. This means that a neutron with a kinetic energy of 100 neV can rise up 1m until it comes to rest. This method is used in the so called gravitational spectrometer which was used in chapter 3 for the determination of the pseudo optical potential of solid deuterium [22].

Magnetic interaction

Although the neutron is electrically neutral, it has a magnetic moment μ_n coupled with its spin and therefore the neutron can interact with a magnetic field. In an inhomogenous magnetic field, the neutron feels the Stern-Gerlach force

$$\overrightarrow{F} = -\overrightarrow{\bigtriangledown}(-\overrightarrow{\mu}_n \cdot \overrightarrow{B}) = \overrightarrow{\mu}_n(\overrightarrow{\bigtriangledown}\overrightarrow{B}) \tag{2.8}$$

The orientation of this force depends on the projection of the neutron spin on the acting field. A magnetic field of 1 Tesla corresponds to a potential energy of ±60.3neV/T. Neutrons with spin parallel to the applied field are attracted those with spin antiparallel are repelled. This property makes it possible to trap polarized neutrons in a suitable magnetic bottle [23, 24].

Strong interaction and neutron optics

The strong interaction is responsible for the coupling of neutrons and protons in the nucleus. The potential which acts on a nucleon in a nucleus can be approximately described by a square well potential with a depth of ≈ 50MeV. The interaction of a free neutron with a nucleus is therefore much larger than the corresponding neutron energy (≈ 25meV). We consider the Schrödinger equation for the relative motion of the neutron and nucleus

$$-\frac{\hbar^2}{2\mu} \bigtriangledown_\eta^2 \Psi + [E - V(\eta)]\Psi = 0 \tag{2.9}$$

where $\eta = r - r_n$ and μ the reduced mass.

Unfortunately, the wavefunction of an incident neutron behaves different in presence or in absence of the interaction, which makes the use of perturbation technique impossible. Fortunately, due to its short range, the wavefunction of the neutron outside the

interaction region is only sligthly disturbed. This allowed Fermi in 1936 to introduce an equivalent potential as solution with neutron wavefunction outside the nucleus

$$U_F(\eta) = \frac{\mathbf{2}\pi\hbar^{\mathbf{2}}}{\mu}\mathbf{a}\delta(\eta) \tag{2.10}$$

where $\mathbf{a}$ represents the unbound scattering length of a neutron with a single nucleus, and $\delta(\mathbf{r})$ is a delta-function. Exchanging $V(\eta)$ with the introduced equivalent potential $U(\eta)$, one obtains for the solution of the Shrödinger equation Ψ_{sc} a function of the scattered wave produced by the nucleus.

$$\Psi_{sc}(r) = -\frac{a}{|\mathbf{r}-\mathbf{r_n}|}e^{ik|\mathbf{r}-\mathbf{r_n}|}e^{i\mathbf{k}\cdot\mathbf{r_n}} \tag{2.11}$$

Scattering from a collection of nuclei

Speaking about neutron scattering on a lattice, one speaks about scattering on a structure of bound nuclei which are in comparison to the previous discussed situation unable to recoil during the scattering. From eqn.2.10 we see, that the Fermi potential and therefore the scattering length are proportional to the reduced mass μ. In a system based on a huge number of bound nuclei, this reduced mass μ can be replaced by the neutron mass m_n. The scattering length on an unbound nucleus, $\mathbf{a}$, can be exchanged by the scattering length on a bound nucleus $\mathbf{b}$.

$$b = \frac{m_n}{\mu}a \tag{2.12}$$

Neutrons incident on a lattice see according to eqn.2.10 a huge quantity of δ-Fermi potentials

$$V_F = \frac{2\pi\hbar^2}{m_n}\sum_i b_i\delta(\mathbf{r}-\mathbf{r_i}) \tag{2.13}$$

where $\mathbf{r_i}$ is the position of the ith nucleus and the sum over i includes all nuclei.

Averaging over a volume of many nuclei, the isotope specific nuclei density N_i replaces the δ-function and we obtain the effective pseudo optical potential of a material surface which also is usually referred to as "Fermi potential".

$$V_F = \frac{2\pi\hbar^2}{m_n}\sum b_i N_i \tag{2.14}$$

Neutron optic

The main effect of this potential on the neutron is that its wave vector k will change inside a medium. As in light optics it is therefore possible to define a neutron refraction index

$$n = \frac{k_{in}}{k_{out}} \tag{2.15}$$

Conservation of energy determines its relation to the optical potential:

$$n^2 = 1 - \frac{V_F}{E_n} \tag{2.16}$$

Only a small number of elements have a neutron refraction index higher than one. Thus, for almost all materials, neutrons can be totally reflected on the external boundary of the material vacuum interface, a property which is used in neutron guide technique. Furthermore, neutrons with kinetic energies below the optical potential are reflected under all angles of incident (UCN). Such neutrons can be trapped inside material bottles. Tab.2.2 give an overview of Fermi potential values for some standard materials used in ultracold neutron physics. Due to the small but non-vanishing penetration depth of

Table 2.2: Characteristics of some standard materials used in UCN physics

element	ρ(g/cm^3)	b (fm)	σ_{tot}(barn)	V$_F$(neV)
^{58}Ni	8.8	14.4	4.6	335
BeO	3.0	13.6	6.6	261
Ni	8.8	10.6	4.49	252
Be	1.83	7.75	0.0076	252
Cu	8.5	7.6	3.78	168
Al	2.7	3.45	0.23	54
Pet	0.92	-0.84	0.06	-8.7
Ti	4.54	-3.34	6.09	-48
^{10}B	≈ 2	-0.1	3840	-3.2
^{6}LiF	2.635	7.65	940	125

neutrons scattered into the medium, the absorption cross-section σ_{tot} leads to possible losses per reflection which can described by

$$\eta = \frac{W}{V_F} \tag{2.17}$$

with $W = N_i \sigma_{tot}$ and σ_{tot} is the total absorption cross-section.

Today, ultracold neutrons are stored for several hundred seconds, using traps from materials with very small absorption cross sections (e.g., Fomblin [25, 10]) or by replacing the material optical potential by a magnetic field gradient acting on the magnetic moment [23]. The possibility of increased observation time, is one of the biggest advantages, which are used in a more accurate determination of the neutron lifetime and in searches for a neutron electric dipole moment.

2.2 UCN production

Due to the beta decay, neutrons exist in nature abundantly only in nuclei. To study the physics of the free neutron or to work finally with ultracold neutrons, one has to produce or set them free from nuclei. The production of a high flux of fast neutrons can be achieved either by a nuclear reaction which is used in spallation sources or by nuclear fission in reactors. Fast neutrons can be slowed down with the help of a moderator

type	Energy E [eV]	Velocity v [m/s]	Wavelength λ [nm]
UCN	$< 0.2 \cdot 10^{-6}$	< 6	> 64
VCN	$0.2 \cdot 10^{-6}$ ... $50 \cdot 10^{-3}$	6 ... 100	4 ... 64
CN	$0.05 \cdot 10^{-3}$ ... $25 \cdot 10^{-3}$	100 ... 2000	0.18 ... 4
thermal	...$25 \cdot 10^{-3}$	... 2200	... 0.18
epithermal	$25 \cdot 10^{-3}$ ... $500 \cdot 10^{3}$	2200 ... $1 \cdot 10^{7}$	... 0.08
fast	$> 500 \cdot 10^{3}$	$> 10^{7}$	

Table 2.3: Neutron terminology versus energy range

(H_2O,D_2O, graphite,...) to the thermal neutron energy range. The neutrons come into thermal equilbrium with the moderator at room temperature. By using a cold moderator based on liquid hydrogen, deuterium, or methane, it is possible to decrease the energy of thermal neutrons (25meV) in a second step to the energy of cold neutrons (2meV) which is still a factor of 10000 higher then the energy of ultracold neutrons. A further loss of energy can be achieved by the following methods:

- Extraction of UCN from the tail of the maxwell distribution of the cold neutron spectrum
- Inelastic downscattering of cold neutrons in a superthermal UCN source

The next subsection will try to describe both methods and their characteristics in more details.

2.2.1 From fast to ultracold in "a conventional way"

The energy spectrum of neutrons $d\Phi/dE$ which are in equilbrium with a moderator at temperature T_0 can be approximately described by

$$\frac{d\Phi}{dE} = \Phi_0 \cdot \frac{E}{(k_B T_0)^2} \cdot e^{-\frac{E}{k_B T_0}} \tag{2.18}$$

where Φ_0 represents the total neutron flux, E the neutron energy, k_0 the Boltzmann constant, and T_0 the moderator temperature. This approximation is valid for the assumption of a non-absorbing, infinite sized moderator. In reality (final size of moderator vessel, etc), not all neutrons are completely moderated. Therefore, the final neutron

spectrum has sligthly higher energies which corresponds to a higher moderator temperature.

From integration of (2.18) over the range of UCN energies, which are defined by the neutron optical wall potential V_F of the storage vessel used, one can obtain a UCN gas density in the moderator proportional to T_0^{-2}

$$\rho_{UCN} = \frac{\sqrt{2}}{3}\sqrt{m} \cdot \Phi_0 \cdot \left(\frac{V_F^{\frac{3}{2}}}{(k_B T_0)^2} \right) \tag{2.19}$$

If we take for example the high neutron flux in the reactor at the Institute Laue Langevin in Grenoble ($\Phi_0 = 1.5 \cdot 10^{15}\, cm^{-2} \cdot s^{-1}$) and insert the wall potential of beryllium ($V_F =$ 252 neV), we obtain a density of $\approx$ 130UCN/cm^{-3} in the moderator at $T_0 = 300K$. In the cold source at ILL with a temperature of 25K we obtain, although the thermal neutron flux at the position of the cold source is slightly reduced ($\approx 5 * 10^{14}\, cm^{-2} \cdot s^{-1}$), still a density of $\approx$ 5000UCN/cm^{-3}.

These numbers sound great for everybody who is thinking about physics with UCN, but reality shows a different picture: several loss mechanisms don't allow to get all UCNs from the huge production volume ($\approx$ 20 liters).

- Cold sources working materials are mostly D_2 or H_2 which results in losses due to absorption and upscattering
- Losses in windows
- Losses on the moderator walls
- Losses during transport to the experimental area ($>$ 20m away)

To overcome or reduce these losses, two ideas have been persued:

vertical extraction Since losses of neutrons in moderator- and window-materials depend on 1/v , neutrons with higher energies can be extracted with higher efficiency. Using a vertical guide dipping into the cold source makes it possible to decelerate faster neutrons with the help of gravity down to the ultracold neutron regime. First test of such a 17m long vertical guide dipping in the cold source at the ILL resulted in a storable density of 19UCN/cm^{-3} [6]. $\rightarrow$ Extraction efficiency 0.38%

neutron turbine The vertical guide concept was improved by increasing the usable neutron energy. By using the so called 'neutron turbine' which is able to transform neutrons with incident velocities in the range of $50 m/s$ down to the UCN regime it is possible to reduce neutron transit losses in the guide. Consisting of a wheel with 1.7 m diameter which is equipped with 690 bent and polished copper mirrors coated with nickel, the turbine setup was first tested by Steyerl and coworkers at

Figure 2.1: The UCN turbine at "niveau" D at the ILL in Grenoble. The vertical neutron guide enters the turbine in the center of the picture[48].

the Forschungsreaktor in Garching [5] before it was sent to ILL. The mirrors rotate in flight direction with a radial speed of 25 m/s which results in a velocity shift of the reflected neutrons. This technique provides so far the highest UCN density of $\approx 50\mathrm{UCN}/cm^{-3}$ which is available at the turbine exit [6] almost continously.

The ILL UCN facility [6] with its four UCN exit ports is up to now (after more than 20 years of operation) a unique facility which provides UCNs regularly to users. Nevertheless, after so many years, the most important experiments reached their statistical limits and physicists started looking for new sources. All developments in the region of conventional UCN production which depend on decelaration of neutrons in potential fields are limited to the initial UCN density inside the used cold sources. This fact is also well known under the name Liouville theorem, which says that the phase space density is constant under the action of a potential force. An increase in phase space density is only possible by means of nonconservative forces

2.2.2 The superthermal concept

One way to overcome the problem of fundamental limitation due to the Liouville theorem is to find systems which don't depend on transformation of the type mentioned above. In 1977, R. Golub and M. Pendlebury [4] proposed a new concept which exploits the inelastic downscattering of neutrons in apropriate media at low temperatures. In this so called "superthermal concept", neutrons loose their energy in one collision process and are therefore not in thermal equilbrium like neutrons in a standard moderator. As a result, the density of UCN corresponds to a temperature much lower than the actual moderator temperature. Instead of a neutron moderator such sources are working as neutron converters.

The simplest case of such a converter can be demonstrated by a two level system with an energy gap ΔE. A neutron can excite a quasi-particle from the lower state to the higher state by transfering the energy ΔE; vice versa, a quasi-particle from the higher state can fall down to the lower state by transfer of the energy ΔE to a neutron. Neutrons those energies fit exactly in the range of this gap can loose almost all of their energy and are downscattered to UCN. The probability for this downscattering process is given by the cross section $\frac{d\sigma}{dE}(E^* \rightarrow E_{UCN})$. The upscattering cross section $\sigma(E_{UCN} \rightarrow E^*)$ follows from the principle of detailed balance

$$\sigma(E_{UCN} \rightarrow E^*) = \frac{E_{UCN} + \Delta E}{E_{UCN}} \cdot e^{\frac{-\Delta E}{k_B T_{con}}} \cdot \sigma(E^* \rightarrow E_{UCN}) \tag{2.20}$$

with $\sigma(E^* \rightarrow E_{UCN})$ being the inelastic downscattering cross section and T_{con} the converter temperature.
From 2.20 it is obvious that the upscattering process gets negligible if one decreases the temperature of the converter down to the limit $T_{con} \ll E^*/k_B$. Without any other losses inside the converter material itself, the superthermal principle allows the production of high UCN densities.

Nowadays, the realization of powerful UCN sources is mainly based on two converter materials.

Superfluid helium-4 due to its non existing neutron absorption cross section allows to produce huge UCN densities inside the converter which are only limited by wall losses on the converter vessel and the finite neutron lifetime. Nevertheless, the work temperature of 0.6K makes it impossible to install a helium source close to a reactor core. The heatload due to gamma radiation would result in expensive and non economic realization.

Solid deuterium sources are currently under construction at PSI and at FRMII. Two sources are already under operation in Los Alamos and Mainz. Due to its non vanishing neutron absorption cross section of 0.4 barn (v_{UCN}=3m/s) the lifetime of an ultracold neutron inside solid deuterium is limited to $\approx 130ms$. This fact makes it impossible to accumulate high UCN densities inside the deuterium itself. As a consequence, systems based on solid deuterium either separate the production

and storage volume by a fast shutter system or work with a thin converter film, which is only a small part of the final storage volume.

2.3 Solid deuterium as converter

As pointed out in the introduction already, this thesis is dedicated to the investigation of a solid deuterium UCN source at the TRIGA Mainz. Therefore, I will mainly focus on the UCN production in solid deuterium. More details about UCN production in superfluid helium can be found elsewhere [19].

The production of ultracold neutrons in solid deuterium can be calculated using the product of the initial neutron spectrum $d\Phi/dE_0$ times the downscattering cross section mentioned already in eqn.2.20.

$$P = N_D \int_0^{E_{UCN}} \int_0^{\infty} \frac{d\Phi}{dE_0} \frac{d\sigma(E_0 \rightarrow E_{UCN})}{dE dE_0} dE_0 dE \tag{2.21}$$

In order to calculate the production over a solid deuterium volume one should not forget the atomic density N_D of solid deuterium.

2.3.1 UCN production cross section

In order to integrate eqn.2.21 we need an expression for the downscattering cross section $d\sigma/dE$ which describes the probability for UCN production. Following [26] and using the incoherent approximation, the inelastic downscattering cross section of neutrons inside solid deuterium can be described by the double differential

$$\begin{aligned} \frac{d\sigma(E_0 \rightarrow E_{UCN})}{dE dE_0} = \sigma_0 \frac{\tau}{2E_0} \cdot \frac{g(E_0 - E)}{(E_0 - E)(1 - e^{\frac{E-E_0}{k_B T_{con}}})} \cdot e^{-\frac{E0+E}{\mu\tau}} \\ \cdot [(E_0 + E + \mu\tau) \sinh \frac{2\sqrt{E_0 E}}{\mu\tau} \\ - 2\sqrt{E_0 E} \cosh \frac{2\sqrt{E_0 E}}{\mu\tau}] \end{aligned} \tag{2.22}$$

This equation assumes mainly one phonon process and a 100% ortho deuterium concentration. In 2.22, μ denotes the nuclear mass in units of the neutron mass, σ_0 the incoherent neutron cross section of deuterium (7.63 barn) and the characteristic energy τ corresponding to

$$\tau = \frac{\hbar^2}{2M\gamma} \tag{2.23}$$

with M the neutron mass and γ the Debye Waller factor which has to be calculated acording to

$$\gamma = \frac{\hbar^2}{2M} \int \frac{1}{\epsilon} \cdot Coth(\frac{\epsilon}{2k_B T}) g(\epsilon) d\epsilon \tag{2.24}$$

The last missing part for the final calculations is represented by the density of states $g(\epsilon)$ which can be described in a first approximation with the Debye model as

$$\gamma = \frac{3\epsilon^2}{(k_B T_D)^3} \tag{2.25}$$

According to [26], we assume for Deuterium a Debye temperature of 110K.

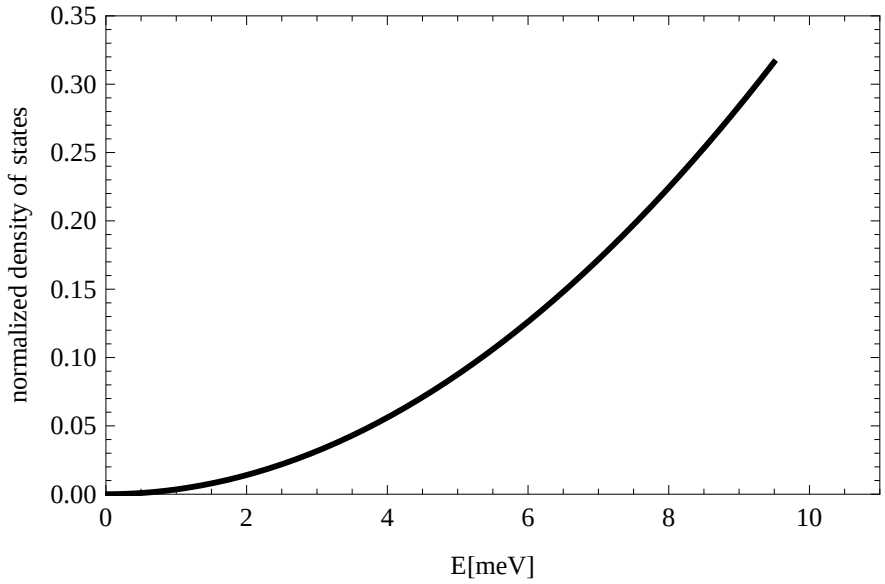

Figure 2.2: Normalized density of states using a standard Debye model with T_D=110K

An evaluation of eqn.2.22 by using the standard Debye model (eqn.2.25) gives some first impressions (Fig.2.3 and Fig.2.4) of the production cross section of solid deuterium. A comparison of a more realistic density of states model by Nielsen et al. [27] and the measured UCN data is given in chap.4.3.2.

From Fig.2.4 its clearly visible that using a solid deuterium converter close to a cold neutron source around 30K would increase the UCN output compared to a thermal neutron source by about a factor of 10. First tests of cold organic premoderators in front of the UCN converter were done in Mainz [28] in 2007. Based on these results, the operation of a premoderator is also planned for the final installation at the new UCN source at beamport D. More information about this topic can be found in chap.6.

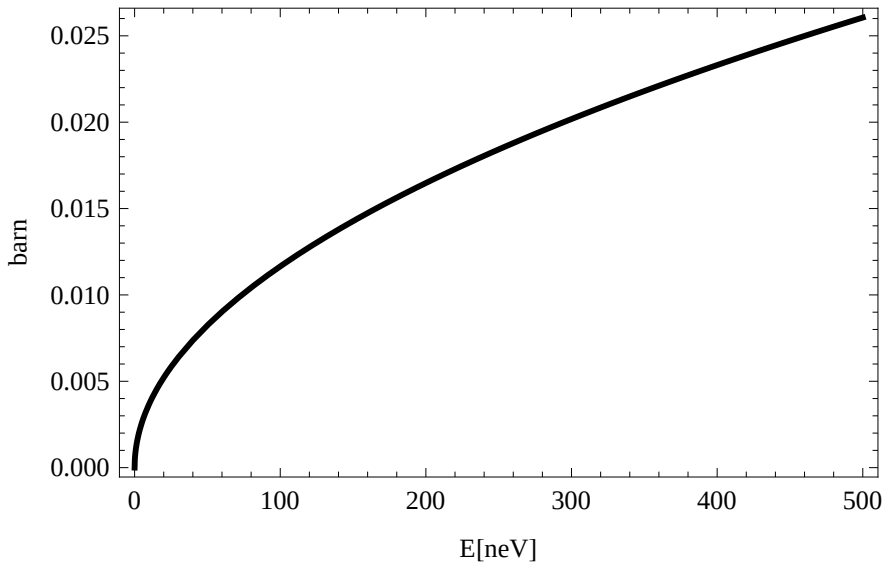

Figure 2.3: Behaviour of the integral downscattering cross section as a function of final neutron energy (0 through 500neV) using the standard Debye model with $T_D = 110K$ in a first approximation

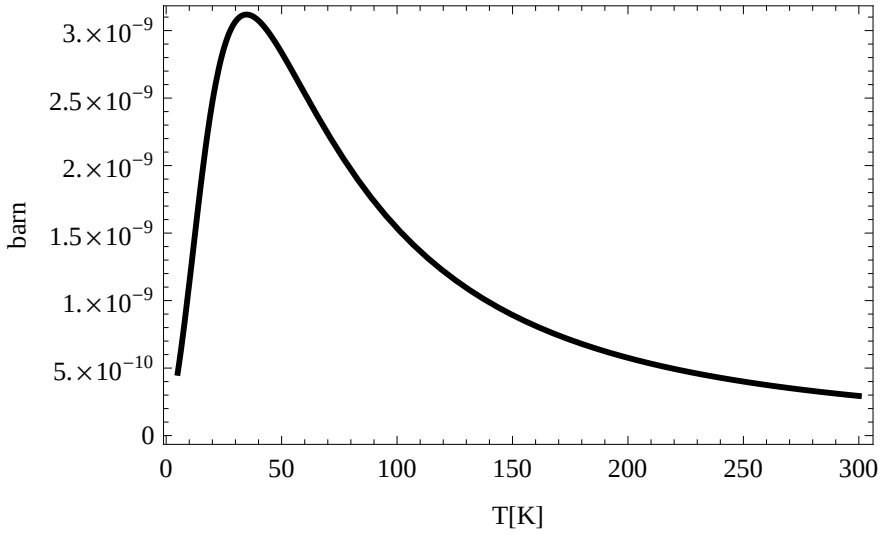

Figure 2.4: Variation of downscattering cross section as a function of the initial neutron spectrum temperature T

2.3.2 UCN losses

As already shown in eqn.2.20, there exists besides neutron downscattering also a neutron upscattering cross section which can be controlled by the converter temperature. Compared to helium, deuterium has in addidtion other non vanishing loss channels, which have to be taken into account.

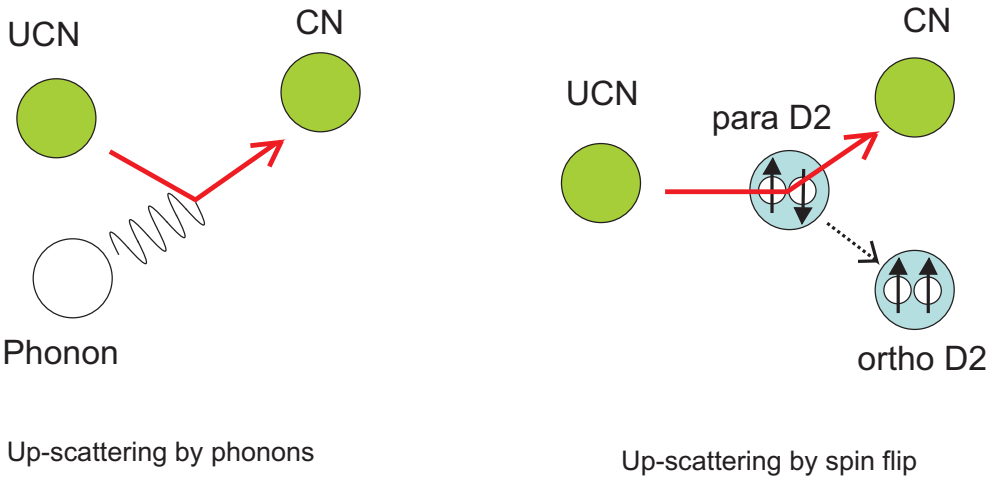

Figure 2.5: Up scattering loss mechanisms

UCN up-scattering by phonons Up-scattering of UCN via phonon excitations in solid deuterium leads to acceleration of the neutrons above the UCN range. The occupation of the excited states at a certain temperature is described by the Boltzman factor. The principle of detailed balance, eqn. 2.20, describes the correlation between the down- and upscattering cross sections as function of temperature. Reducing the temperature of the converter, Fig.2.6, shifts the balance towards production and makes this loss channel negligible. Below a converter temperature of 5K, the losses due to phonon upscattering get comparable with the all time existing absorption cross section.

UCN up-scattering by spin flip on para deuterium The D2 molecule exists in two different configurations. The anti-symmetric configuration is called ortho deuterium, J=even, the symmetric state, para deuterium, J=odd. The transition between the ortho ground state J=0 and the para J=1 state requires an energy of $E_{spinflip} = 7.5meV$ and a spin flip. In a scattering process of a produced UCN with a para deuterium molecule, the spin can be flipped, $J = 1 \rightarrow J = 0$, and the UCN gains the spin flip energy and leaves the UCN energy region.

In natural deuterium (deuterium at room temperature) the para concentration is about 33%. As can be seen in Fig.2.6, increasing the ortho concentration of the deuterium if one wants to use it as UCN converter is mandatory.

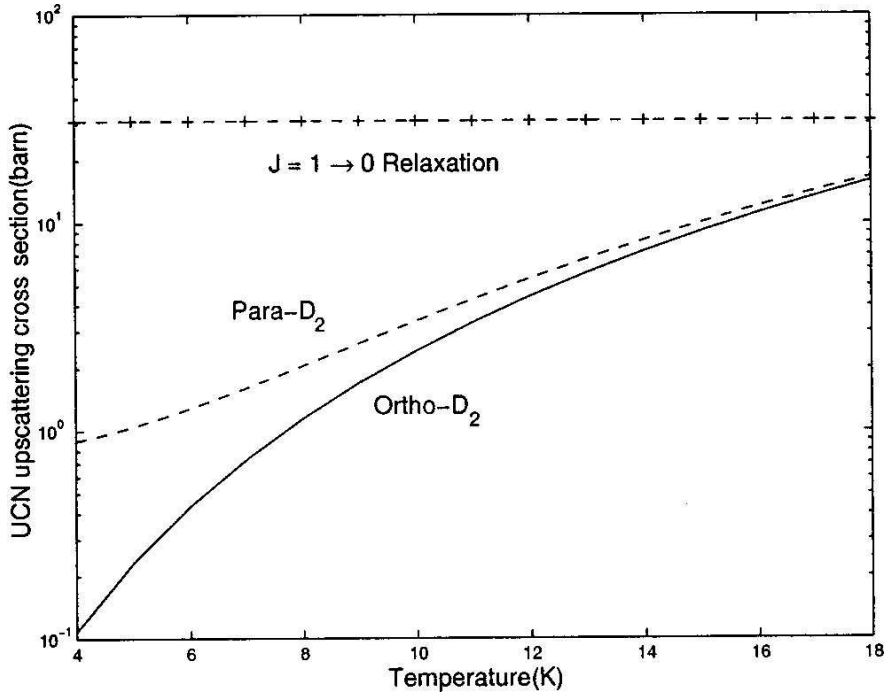

Figure 2.6: Upscattering cross-sections of solid deuterium (neutron velocity $\approx 8m/s$) for : i. the temperature dependent one phonon process on pure para (dashed line) and pure ortho (solid line) deuterium and ii. the temperature independent zero phonon process on natural (33% para) deuterium. The plot is taken from Ref.[29], where the zero phonon cross-sections were calculated for the first time.

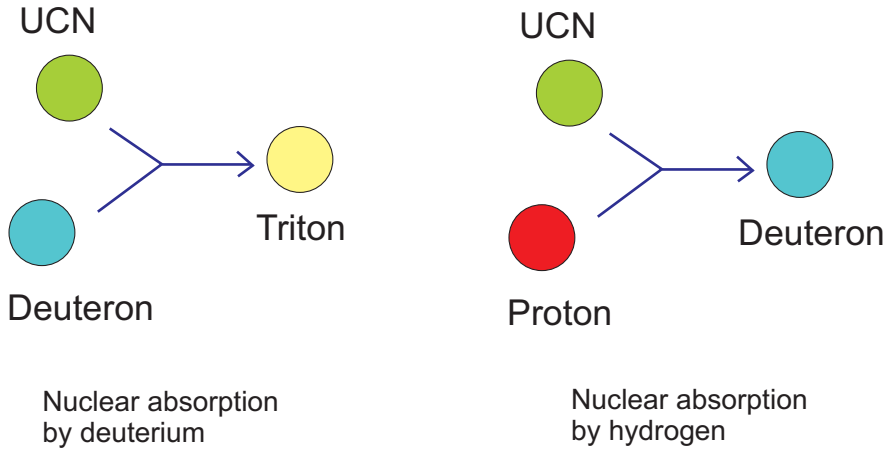

Figure 2.7: Absorption loss mechanisms

Nuclear absorption by deuterium As already mentioned, deuterium has a non negligible absorption cross section due to the reaction (d+$n \rightarrow t$+γ) This intrinsic loss mechanism cannot be avoided; hence the minimum attainable loss cross section is $\sigma_{abs}(therm.) = 5.19 \cdot 10^{-4} barn$.

Nuclear absorption by impurities In highly purified deuterium the most abundant impurities are hydrogen atoms. Due to its large absorption cross section of $\sigma_H(therm.) = 0.3326\ barn$, it is necessary to start with the lowest possible hydrogen content.

Summary

In a standard procedure the different neutron loss channels i inside the deuterium bulk are expressed by different neutron mean free paths

$$\lambda_i = \frac{1}{N_D \cdot \sigma_i} \tag{2.26}$$

with N_D the atomic number density of solid deuterium and σ_i the cross section of the loss channel for an given neutron velocity.
The total mean free path λ_{loss}, used for the calculations of the neutron output from the converter, can be written as the inverse sum of the individual loss mechanism $\lambda_{abs\ D}$, $\lambda_{abs\ H}$, $\lambda_{up\ phonon}$ and $\lambda_{up\ paraD2}$.

$$\frac{1}{\lambda_{\mathrm{loss}}} = \frac{1}{\lambda_{\mathrm{abs}}(\mathrm{D_2})} + \frac{1}{\lambda_{\mathrm{up}}(\mathrm{D_2})} + \frac{1}{\lambda_{\mathrm{abs}}(\mathrm{H_2})} + \frac{1}{\lambda_{\mathrm{para}}(\mathrm{D_2})}. \tag{2.27}$$

Together with the averaged ultracold neutron velocity v_{UCN} inside the ultracold neutron converter, which can be approximately calculated as

$$\bar{v}_{\mathrm{ucn}} = \frac{3}{4} \cdot \sqrt{2 \cdot (V_{\mathrm{F}}(\mathrm{guide}) - V_{\mathrm{F}}(\mathrm{sD_2}))/m_{\mathrm{n}}} \approx 3.0\ \mathrm{m/s}, \tag{2.28}$$

one obtains the neutron lifetime inside the deuterium bulk

$$\tau_n = \frac{\lambda_{loss}}{\bar{v}_{\mathrm{ucn}}}. \tag{2.29}$$

Based on the presented cross sections and an atomic density of $N_D \approx 2.5 \cdot 10^{22}/cm^3$, one can derive a mean free path of ultracold neutrons ($\bar{v}_{\mathrm{ucn}} = 3m/s$) inside a superthermal solid deuterium source at standard working parameters ($T_{con} = 6K$, $c_{para\ D} = 1.5\%$ and $c_H = 0.5\%$) as

$$\lambda_{loss} \approx 6.2\ cm. \tag{2.30}$$

In comparison with the possible lifetime inside a superfluid helium converter, this value corresponds to a rather short neutron lifetime of

$$\tau_n \approx 21\ ms. \tag{2.31}$$

This obvious drawback of solid deuterium is compensated by the larger phase space for neutron downscattering.

Anyhow, the goal of every superthermal ultracold neutron source based on solid deuterium should result in no further decrease of this "optimum" lifetime, which may happen due to multiple scattering inside a polycrystal converter.

2.4 UCN at a pulsed source, the reactor TRIGA in Mainz

Before I start with the description of the experimental setup in chap.3 for the investigation of a solid deuterium UCN source, I want to give a short introduction of our thermal neutron facility, the TRIGA Mainz and its special features concerning future experiments with ultracold neutrons.

2.4.1 UCN at pulsed neutron sources

One drawback of all superthermal UCN sources is the low operation temperature. Of course it is possible to cool down a solid deuterium crystal below 6K. Nevertheless, this "cooling" procedure close to a stationary strong neutron and gamma field like they exist at neutron sources like the FRMII or the ILL is connected with an expensive and powerful helium cooling facility. In 1995, Yu. Pokotilovsky [30] published his ideas about a pulsed solid deuterium UCN source at low power research reactors like the TRIGA type with its "pulse" mode operation opportunity (see next section). The main intention behind his idea was:

- Almost all experiments dealing with ultracold neutrons (lifetime, nEDM,...) are storage experiments and therefore have a cyclic character. This means, that the experimental setup has to be loaded with neutrons within a filling time. During the actual storage run no additional neutrons are needed. After a predefined storage time, the survived neutrons are detected and the whole procedure is continued. Therefore, the optimal UCN facilities for these types of experiments are pulsed sources with a high neutron peak intensity and typical repetition rates in the range of the storage times, normally a few minutes.
  Pulsed TRIGA reactors are able to produce pulses with every 5 min which makes them to excellent thermal neutron sources for pulsed UCN sources, see also Chap.4.4.

- The temperature of the converter is of great importance for the extraction of ultracold neutrons (chap.4.3.2). The nuclear heating problem which is not negligible in stationary research reactors is minimized at pulsed sources to the duration of the pulse ($\approx 30ms$) itself, see also Chap.6.3.

- There is no radiation background in the experimental area after the reactor pulse (reactor is switched "off").

2.4.2 The reactor TRIGA Mark II in Mainz

The TRIGA reactor in Mainz was for the first time critical in 1965. The name TRIGA includes the purpose of its design:

- **T**raining
- **R**esearch
- **I**sotope production
- **G**eneral **A**tomics

The TRIGA Mainz is a free standing swimming pool type reactor which provides four beamports, a thermal column and several radiation channels close to the reactor core which are used for radio chemical analysis. This reactor can be operated at a steady-state power of 100 kW or in pulsed mode with a maximum power of 250 MW and an energy release of 10 MWs [31].

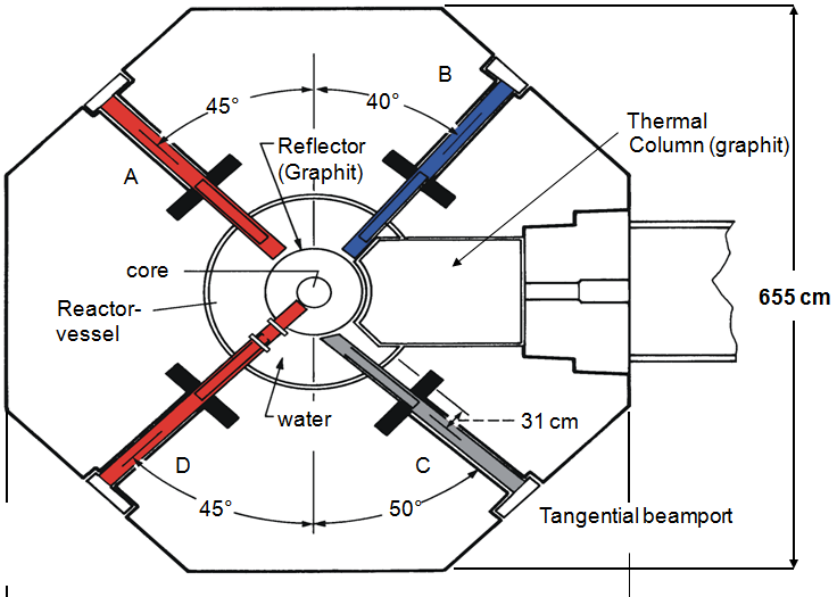

Figure 2.8: Scheme of the TRIGA Mainz. The existing prototype UCN source is located at the tangential beamport C. The new upgraded UCN source is installed at the radial beamport D which crosses the internal graphite reflector ring and ends close to the core.

76 fuel elements are actually installed in the reactor core. The used chemical composition Uranium (20% ^{235}U)-Zirconiumhydride (UZrH) combines the production of neutrons (nuclear fission) and their moderation (neutron scattering on hydrogen inside the Zr-matrix) within the fuel elements.

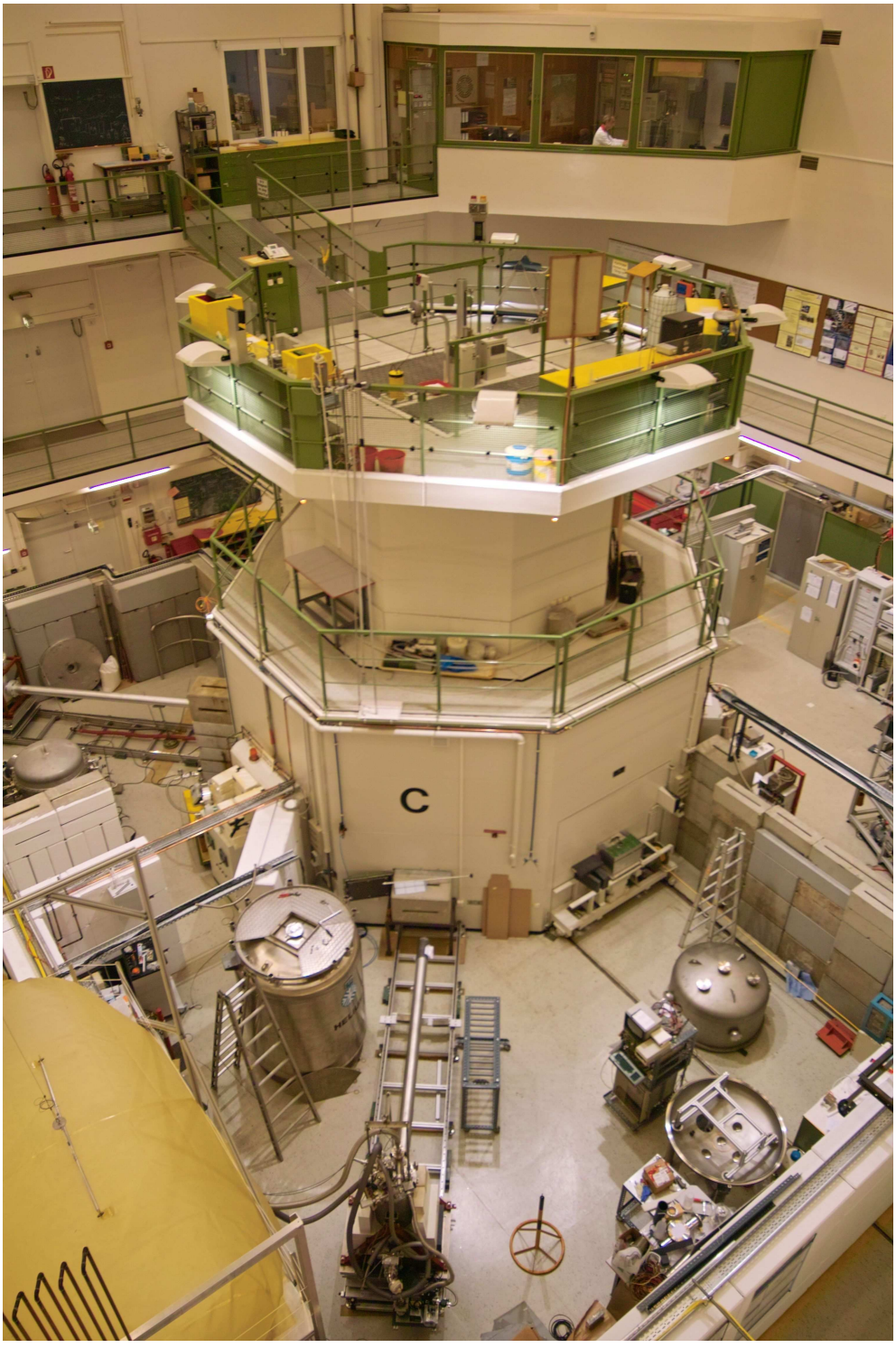

Figure 2.9: Actual picture of the TRIGA Mainz. View from top of the crane system on beamport C and the installed prototype inpile part of the solid D_2 source

In a standard water-cooled reactor, sudden removing of the control rods results in a not controlable chain reaction, leading finally to a melting of the fuel elements. This is because the neutrons from the fission reaction remain "cold" from interacting with the cold water around the fuel and maintain their ability for further fissioning of uranium atoms in the fuel. The mixing of fuel and moderator in one element, however, results in an inherent safety. Therefore, as the fuel temperature increases when the control rods are suddenly removed, the neutrons inside the hydrogen-containing fuel rod become warmer than the neutrons outside in the cold water. These warmer neutrons inside the fuel cause less fissioning in the fuel and escape into the surrounding water. Finally the reactor automatically reduces power within a few milliseconds, faster than any engineered device can operate.

Due to this inherent safety feature, the so-called prompt negative temperature coefficient, the TRIGA Mainz is able to increase its power rapidly "pulsed" to a maximum power level of 250 MW with a reactivity insertion of $2\rho/\beta$ in the pulse (in the language of reactor users termed 2 $ pulse), corresponding to a released energy of about 11 MWs.

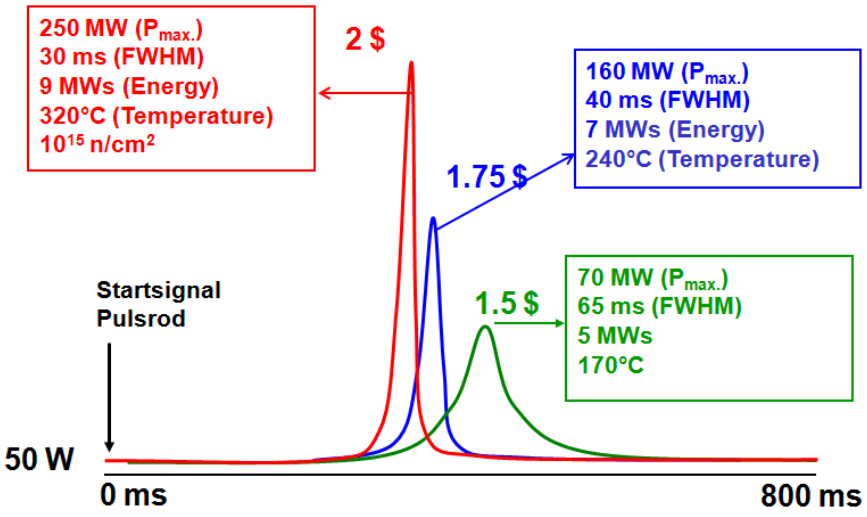

Figure 2.10: Schematical time sequences for different pulses at the TRIGA Mainz

Here, $\rho = \delta k/k$ is the reactivity with the effective multiplication factor k being the number of fissions in one generation divided by the number of fissions in the previous generation. The quantity β represents the number of delayed neutrons. For the TRIGA fuel elements with aluminium cladding and 8 % by weight U-ZrH the value of β is 0.0073 [31].
Depending on the pulse rod setting and the final reactivity the pulselength can vary between 30ms and 100ms (see Fig.2.10)

The actual neutron fluences The neutron fluences of the tangential and radial beamports C and D were measured with the help of neutron activation analysis. A detailed description of the measurement procedure can be found in [32]. On both beamports, the measurements were done in pulsed mode operation driving the reactor at a power of 6.5 MWs. The results of our measurements can be seen in Fig. 2.11

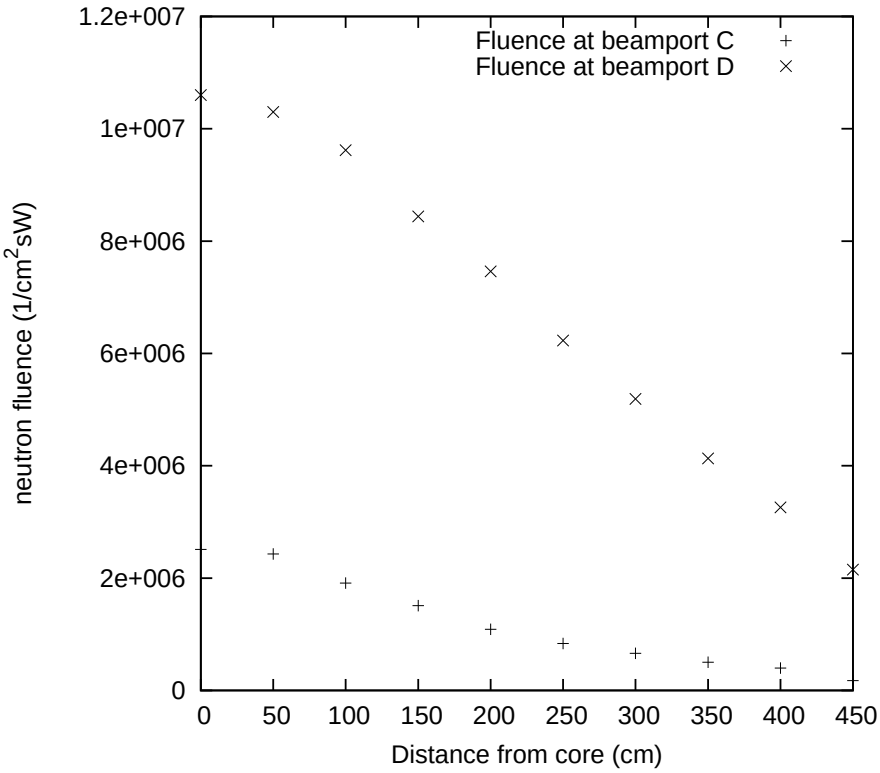

Figure 2.11: Thermal neutron fluences at beamport C and D during a 1.5$ pulse measured with gold foil activation analysis.

At the position of the deuterium converter (50mm away from the end of the beamport) a thermal neutron flux of $\approx 2 \cdot 10^{14} n/cm^2 s$ was measured at the tangential beamport C. This corresponds to a total number of $\approx 1.5 \cdot 10^{13} n/cm^2$. It's quite obvious that one would gain a factor of 4-5 in thermal neutron flux by installing a UCN source at beamport D. However this gain which is related to the smaller distance between the solid deuterium and the reactor core, might be compensated to our disadvantage by a stronger nuclear heating of the deuterium by fast neutrons and hard gammas (see also chap.6). Therefore, first attempts to understand the working principle of a solid deuterium UCN source under "real" reactor conditions were done at beamport C outside of the graphite reflector ring (see Fig.2.8).

Chapter 3

The prototype of a superthermal source based on sD_2 at reactor TRIGA Mainz Beamport C

The first steps in the direction to an UCN source at the TRIGA Mainz started in 2004. In order to investigate solid deuterium as UCN converter (under reactor conditions) for the future Mini-D_2 UCN source at the FRM II [16], a prototype source was designed and built in collaboration with the department E18 and Mainz. The first version was installed at the beamport C of the TRIGA Mainz at the end of 2004. After some technical problems, the first version was revised and the second version started its operation in January 2006. Several Diploma Theses and one PhD thesis [28] referred already to the design and the construction of the existing source setup. The experimental part of this thesis used the existing inpile cryostat of the UCN prototype source. Therefore, I will point out only a few important topics of that inpile cryostat before I will start with the discussion of an improved gas system for the future source at beamport D.

3.1 The experimental setup

The second upgraded setup which was constructed and installed in 2005 consisted of three main parts.

- **The inpile-cryostat** which in its last version contains a highly polished stainless steel (nocado) UCN guide. One end of the guide is closed by a converter cup cooled with liquid helium (to provide the cold part for freezing out solid deuterium from the gas phase). The other end is sealed by an aluminium exit window.
- **The deuterium gas handling system** includes several important parts necessary for safe handling of the deuterium gas. It consists of a storage vessel for the high purity deuterium gas, a 10K storage vessel (cooled by a cold head), a gas valves manifold containing and a huge number of pressure transducers.

- **The control system** in its first version was based on a commercial Simatic S7-400 controller to drive and monitor all valves and sensors of the gas system and cryostat.

3.1.1 The inpile-cryostat

The inpile-cryoytat (Fig.3.1) is made of two parts: the inpile tube, with external diameter of 140mm containing neutron guide with cold UCN converter inside and the vertical cryostat vessel for connection of all necessary support lines (deuterium gas, liquid helium/nitrogen, sensors). The whole setup is mounted on a carriage system which allows easily to move the source in and out of the reactor beamport.

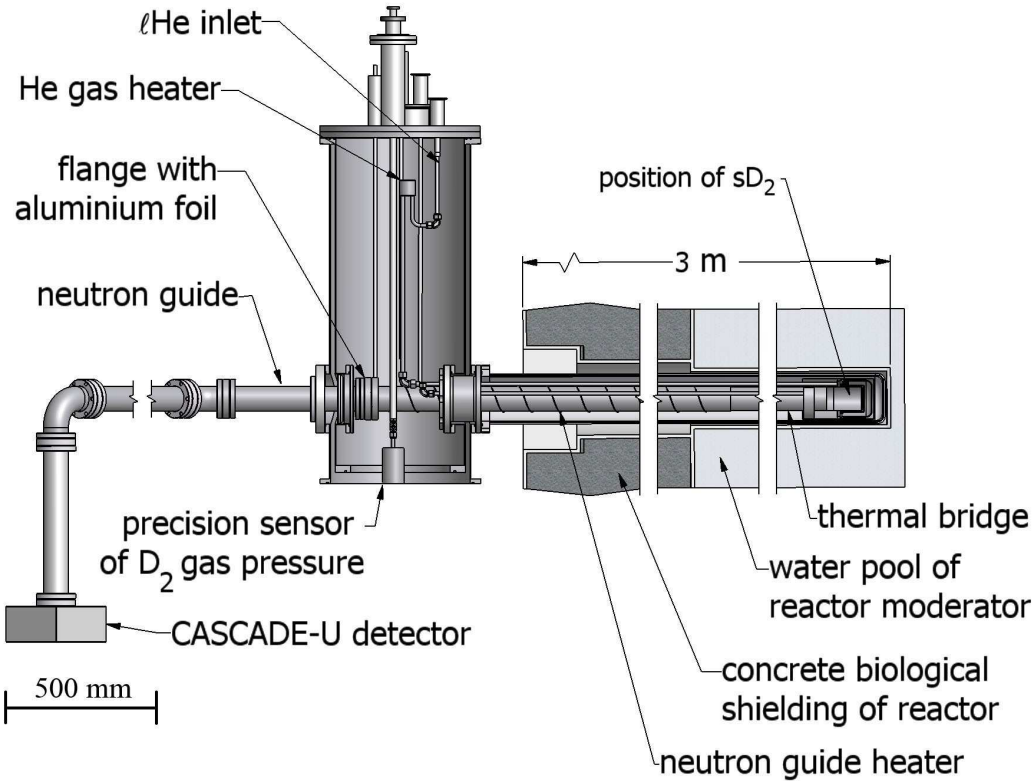

Figure 3.1: Sectional drawing of the sD2 UCN source. The vertical cryostat is mounted on a carriage (not shown) so that the whole setup can be moved in and out of the beamport.

3.1.2 The D_2 converter cup and the neutron guide system

The main part of the inpile cryostat consists of an electropolished stainless steel tube with a length of $\approx 3m$ and an inner diameter of 66mm which serves as transport guide for ultracold neutrons, produced in a solid deuterium crystal, frozen inside a double

walled converter cup at one end of the guide. The converter cup (Fig.3.3) is made of the same electro-polished tube and is welded to one end of the neutron guide situated close to the reactor reflector inside beamport C. With an internal length of 60mm the cup can keep up to $200cm^3$ of solid deuterium. Cooling of the cryogenic part below 10K is provided by a flow of liquid helium (actually by a flow of gas-liquid helium mixture) around the internal converter cup. The helium lines have a diameter of 10mm. To decrease the heat load from the surrounding vacuum tube at room temperature, the whole deuterium converter is closed by an aluminium shield cooled to 77K with liquid nitrogen. The manipulation of the frozen deuterium temperature was realised via heating of the incoming helium by a special gas heater. The heat load caused by

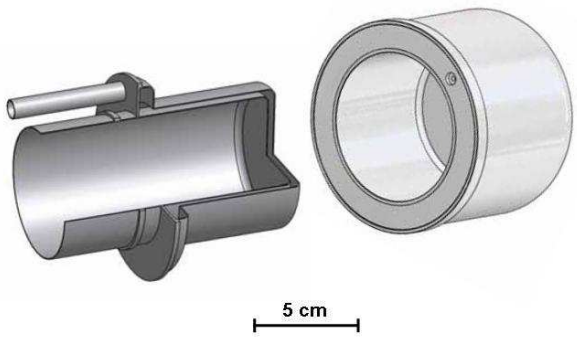

Figure 3.2: Left: Cut through the installed converter cup at the end of the neutron guide. Right: Aluminium premoderator vessel which fits exactly on the outer diameter of the converter cup.

thermal conductivity of the 2mm thick stainless steel tube of the neutron guide would increase the liquid helium consumption. On the other hand, it would also result in a cooling down of the neutron guide, resulting in a freezing of residual gas molecules (N_2, H_2 ...) on the inner surface of the neutron guide and therefore causing big losses of UCN travelling through the guide. To overcome this problem, the outer diameter of the neutron guide was machined to a thickness of 0.5mm on a length of 40cm directly behind the converter cup. This acted as an efficient thermal bridge which reduced the heatload on the converter cup from 30W/s to the minimal heatload of 75mW/s. In addition, the outer part of the neutron guide following the thermal bridge downstream was equipped with a heating wire to keep the rest of the UCN guide at room temperature.
As it was shown in Fig.2.4, the use of a cold neutron moderator near the deuterium converter can result in a gain in UCN production. Therefore, an exchangeable neutron

premoderator cup with an external diameter of 110mm was built. The vessel was built from aluminium and was also cooled after installation on the converter cup by the incoming helium flow.

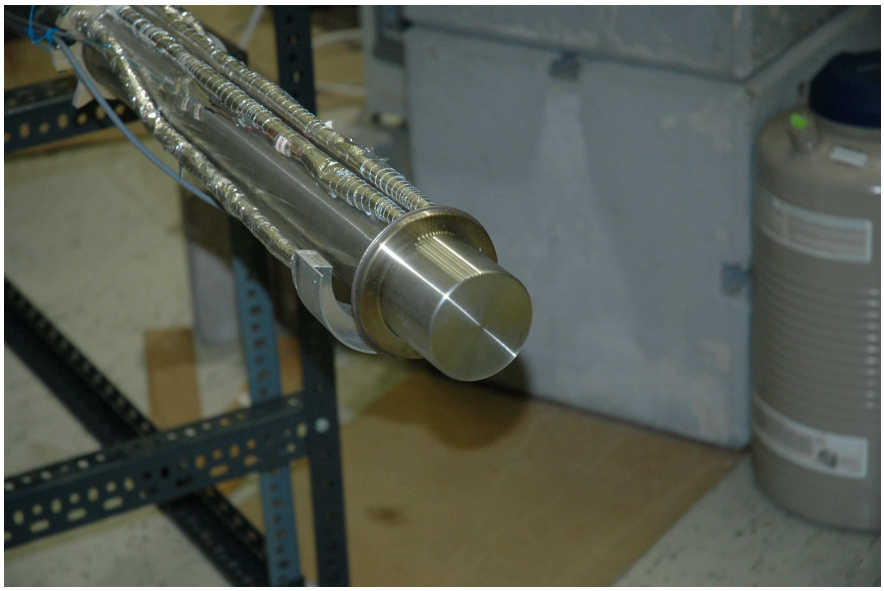

Figure 3.3: The deuterium converter cup after installation. The 10mm "liquid" helium lines on top of the neutron guide are covered with superisolation. A liquid nitrogen isolation shield can be mounted on the cooled holder behind the converter cup

3.1.3 The deuterium gas handling system

The deuterium gas handling system is an important part of the UCN source. It should provide the users with a safe processing of the flammable deuterium gas. Under processing one understands:

- storage of several hundred liters of D_2 gas
- preparation of very pure (98%) ortho D_2
- cleaning of D_2 gas from possible contaminations
- transfer of D_2 gas to the converter cup of the source (during freezing from the gas phase) and from the source back to the reservoir (evaporation of D_2 crystal)

To assure safe processing of these actions, the system was designed on the principle of a two barrier protection. The closed deuterium system is entirely mounted in a special overpressure vessel, filled with helium at a slightly higher pressure than the surrounding atmospheric pressure. As a result, deuterium gas leaking out from pipes (worst case) cannot mix with air and form an explosive mixture.
The first version of the deuterium gas system for the prototype source at beamport C

was designed at the department E18 at the Technical University, Munich. A detailed description of this system can be found elsewhere [28].
Based on the experience which could be gained during one and a half year of succesful operation, a new gas system for the future UCN source at beamport D was designed, built and finally tested in combination with the prototype inpile cryostat at beamport C. Several improvements were done which will be descibed in more detail.

- tubing was simplified by using standard certified Swagelok connection and Swagelok valves instead of big Stoehr valves for welding
- a premoderator gas handling system was included in the new system
- a new para/ortho converter based on Oxysorb® was installed
- storage of deuterium and premoderator gas is done in separate vessels outside the control system
- A new commercial Raman spectrometer was included and the Raman cell was directly connected to the deuterium gas system enabling online ortho/para analysis

Deuterium and vacuum system

A scheme of the control software of the deuterium and premoderator system can be found in Fig. 3.9. To improve the accessibility and the commutability of all components, we used instead of welded tubes like in the former system, the standard swagelok technique. This technique made the system more flexible and much more easily serviced without loosing its reliability. The deuterium parts of gas system can be evacuated by a oil free pump station including an Oerlicon EcoDry forepump and a TurboVac 50 turbomolecular pump. Unlike in the old system, the deuterium part has its own vacuum pumps which are used only to evacuate the deuterium lines, including storage vessel, the Raman cell, the zeolithe cleaning trap, the Oxysorb® system, and the deuterium system of the inpile cryostat. The premoderator lines and the helium barrier are pumped by their own vacuum stations.
To monitor vacuum and pressure inside all gas system parts, IONIVAC ITR90 and

Table 3.1: Equipment and working parameters of the new gas system for channel D

	deuterium	premoderator
storage volume	300l Al vessel	500l Al vessel
vacuum system	DryVac + Turbo pump	DryVac + Turbo pump
vacuum gauge	IONIVAC	IONIVAC
pressure transducer	CERAVAC	CERAVAC
Zeolith trap	intern	non
para/ortho converter	intern	extern
flow control for freezing	MKS	MKS
Maximal pressure in source	700mbar	700mbar

CERAVAC CTR90 transmitters from Oerlicon are installed. For the switching of the deuterium lines, all-metall Swagelok valves (normal closed) are installed.
Some main features of the new gas system are presented in tab.3.1

For safety reasons, overpressure valves (opening pressure 700mbar) and rupture discs (burst pressure 1.5bar) are installed between the in-pile cryostat and the gas system. This way, the dangerous build up of deuterium or premoderator gas pressure in the cryostat during unexpected melting of the frozen converter should be safely prevented.

A new ortho-para converter

As already mentioned, deuterium at standard conditions ("fresh from the bottle") contains 33% of para deuterium. Such concentrations would result in non negligible UCN losses due to spin flips [29].
The normal conversion from the 66% ortho deuterium at room temperature to the thermal equilibrium at cryogenic temperatures ($c_{o,T}$ around 98%) via the forbidden transition can be described by a linear differential equation as

$$\frac{dc_o}{dt} = K \cdot [c_{p,0} - (1 - c_{o,T})] \cdot e^{-K \cdot t} \rightarrow c_o(t) = (1 - c_{o,T} - c_{p,0}) \cdot e^{-K \cdot t} + c_{o,T}. \quad (3.1)$$

Here, K is the conversion coefficient, t the elapsed time, $c_{p,0}$ the initial para concentration and $c_{o,T}$ the final ortho concentration at a temperature T. Without a paramagnetic catalyst, the conversion coefficient K is $K_{nat} = 6 \cdot 10^{-4} h^{-1}$[33]. This corresponds to a conversion time of 6 months. By using paramagnetic catalysts as reported by groups from PSI [34] and Los Alamos [35], one can decrease the conversion time down to hours. Unlike the old gas system, in which an external para-ortho converter was used [28, 36], we designed a horizontal converter cell, Fig.3.4 with a volume of 0.5 liter, which was filled with two catridges of Oxysorb® (Cr_2O_3).

Apart from the lid of the converter cell, all other cryogenic parts are made from copper. For thermal isolation of the cryogenic system from the vacuum housing and the deuterium gas lines, the lid and the connection tubes are made from stainless steel. To prevent the Oxysorb powder leaking from the converter cell, a standard stainless steel sinter filter with a porosity of $5\mu m$ is soldered to the exit lid.

With a "10K" cold head (from Sumitomo) and an isolation vacuum better than $5 \cdot 10^{-6} mbar$ a converter vessel temperature of 7 K can be reached. Four Cernox^{TM} sensors distributed over the converter volume and one thermocoax heating wire around the connection of the neck from the 2nd stage of the cold head to the converter vessel allow to control the temperature of the system with an accuracy of 0.1 K.
The volume of the converter is big enough to liquefy almost 300 l of deuterium from the whole gas storage vessel $\sim$ around 14 mol (usually there are only 9mole of deuterium in the system). At minimal temperature, it takes around 5 hours to empty the storage vessel down to a minimal pressure of 3mbar. A determination of the conversion speed like it was done in [36, 28] was impossible because the para-ortho conversion starts already during pumping of the warm gas. The large surface of the Oxysorb which is increased in the horizontal arrangement of our setup favors the conversion. As a result, after 5 hours of pumping we obtain already an ortho concentration of 96%.

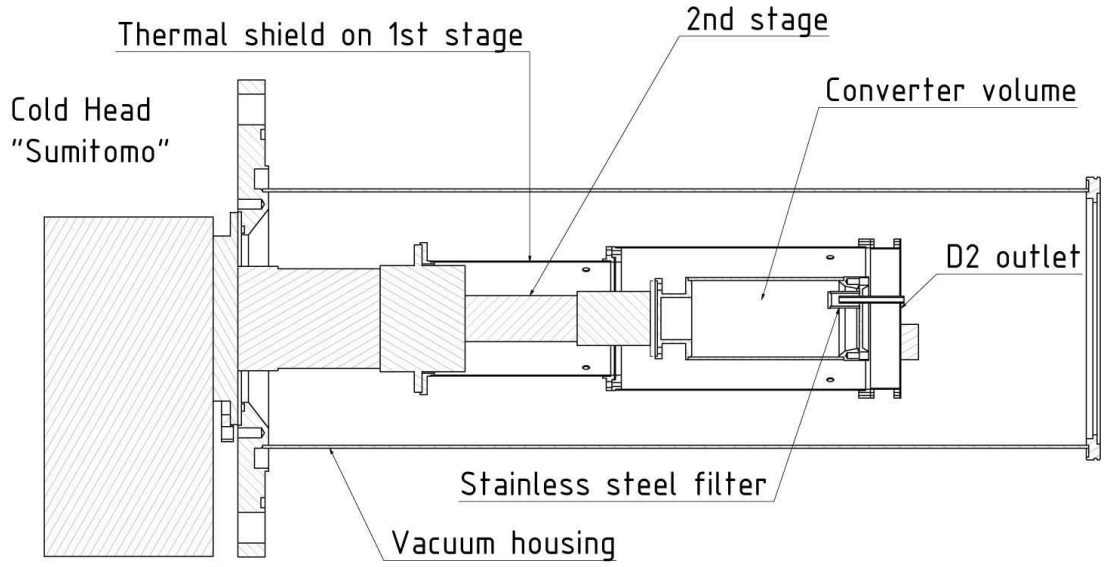

Figure 3.4: Sectional drawing of para-ortho converter. Cooling down to 8K is provided by a cold head from sumitomo

A further increase of the ortho concentration up to 98.2% was reached by the "boiling" procedure which is also described in [36] and [28]. After emptying of the storage vessel, the converter volume is isolated and its temperature is increased up to 22 K. The boiling of the D_2 ensures a good contact of the whole D_2 volume with the Oxysorb and enables further conversion which reaches its limit after 5 hours.

Raman spectroscopy

As described already in many publications [35, 34, 28], the ortho-deuterium concentration can be measured by using the Raman spectroscopy technique. Therefore, the commercially available Raman spectrometer 'Sentinel-II-532' (Fig.3.5) from Bruker Optics was purchased and installed close to the new deuterium gas system. As can be seen in Fig.3.5, the spectrometer is mounted in a standard 19 inch rack. It includes a 532nm laser with a maximum power of 100mW and a CCD grid spectrometer with a spectral resolution of $3.8cm^{-1}$ within a range from $80cm^{-1}$ to $3200cm^{-1}$. An external probe is connected via two optical fibres with the laser and the spectrometer. Due to the excitation and detection of the Raman light in one optical axis, a compact deuterium Raman head consisting of the external probe and a gas cell was built and directly connected to the deuterium system. For the gas cell, we used a standard Duran® glass vessel (length 150mm, diameter 20mm) coated with aluminium.
Fig.3.6 shows a Raman spectrum of the Raman cell filled with converted deuterium at a pressure of 800mbar which was obtained after an integration time of 10min.

After subtracting the background spectrum (empty cell) produced by the glas window of the cell, we get the pure deuterium spectrum, presented in Fig.3.7.

In order to determine the ortho deuterium concentration c_o, one can use, according to Ref.[33] the ratio, R, of the Raman intensities of the well known spin transitions J=0

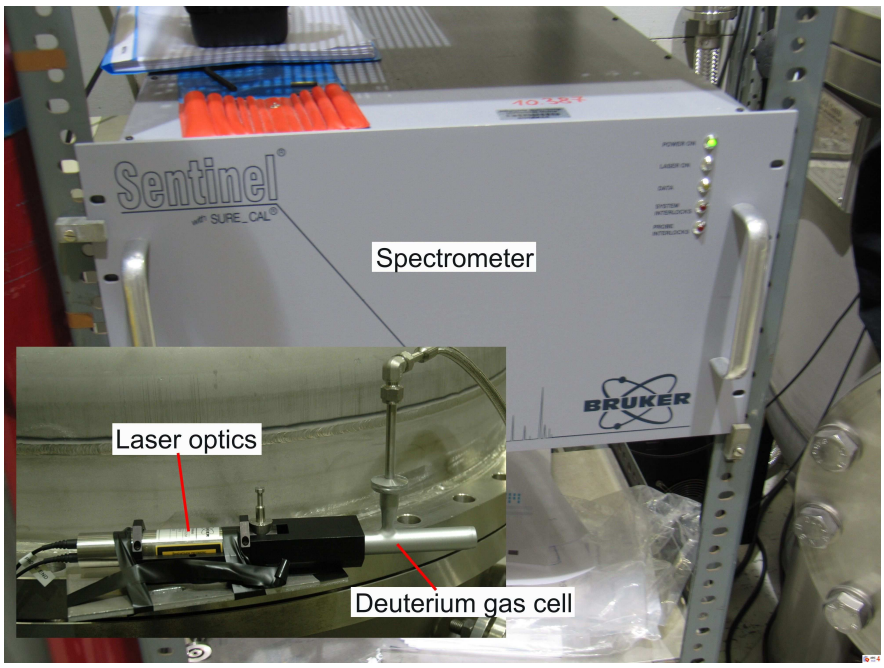

Figure 3.5: Background: Commercially available Raman spectrometer 'Sentinel-II-532'; left picture: Raman probe dismounted from its case.

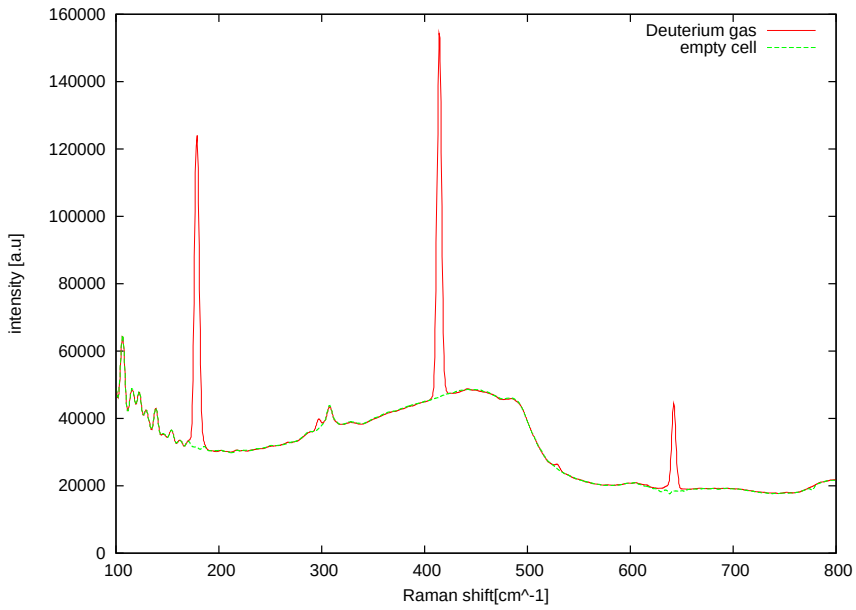

Figure 3.6: Raman spectra of converted D_2 gas at a pressure of 800mbar (red line) and of the empty Raman cell (green line). Only the D_2 rotational lines are shown.

(ortho) and J=1 (para). Together with the transistion frequencies which can be found

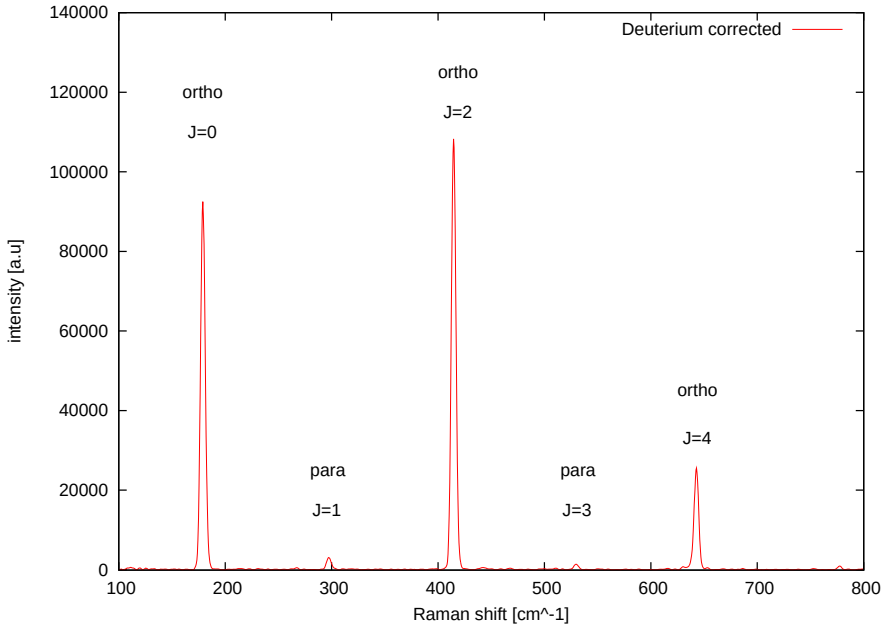

Figure 3.7: Raman spectrum of D_2 gas (800mbar). Only the D_2 rotational lines are shown. Taking the ratio of the integrals under the J=0 and J=1 peaks, the measured calibration factor k_{cal} of eqn.3.4, eqn.3.2 and eqn.3.3, one obtains a ortho concentration of 97.5%.

in literature [33], R is expressed as

$$R = \frac{S(0 \to 2)}{S(1 \to 3)} = \frac{5}{3}\frac{c_o}{1-c_o}\left(\frac{\omega - \omega_{02}}{\omega - \omega_{13}}\right)^3 \tau_{gas} \tag{3.2}$$

with ω the frequency of the initial laser light, ω_{02} and ω_{13} the frequencies of the ortho (J=0) and para (J=1) transistions and τ_{gas} a correction factor taking into account the distribution of the rotational states of the molecules.

Setting the right side of eqn.3.2 to a constant calibration factor k_{cal}

$$\frac{5}{3}\left(\frac{\omega - \omega_{02}}{\omega - \omega_{13}}\right)^3 \tau_{gas} = k_{cal}, \tag{3.3}$$

one can exclude the not well known spectral efficiency of the raman spectrometer. Using the well known ortho concentration of natural deuterium (66%) and the measured ratio of the ortho-para intensities (see Fig.3.8), k_{cal} can be calculated from

$$R_{nat} = \frac{S(0 \to 2)}{S(1 \to 3)} = 2 \cdot k_{cal}. \tag{3.4}$$

to be $k_{cal} = 0.76$.

With the used setup, it is possible to obtain within an integration time of 10min an accuracy of the ortho deuterium concentration of 0.5%. For possible contaminations

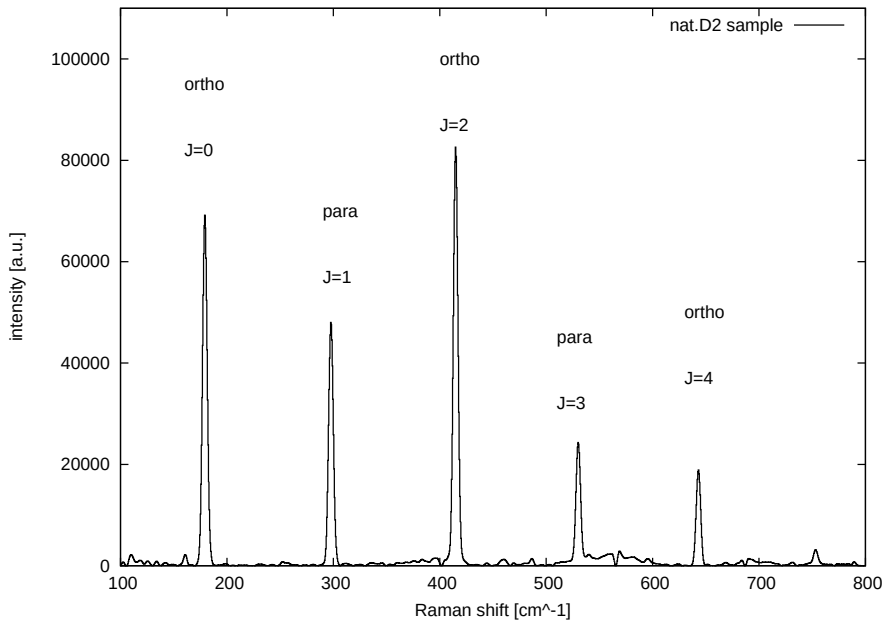

Figure 3.8: Raman spectrum of natural D_2 gas at a pressure of 600mbar.

	D_2		H_2		HD	
J	Exp	Literature	Exp	Literature	Exp	Literature
0	179	179.12	354.0	354.39	not visible	267.12
1	297.3	297.63	587.0	587.07	not visible	443.17
2	414.6	414.78	814.3	814.48	not visible	616.21
3	529.8	530.07	1034.9	1034.75	not visible	785.15

Table 3.2: Raman lines for the charateristic rotational states of deuterium and its possible main contaminations. The experimental values for D_2 were obtained from the data plotted in Fig.3.8. For hydrogen the values are taken from the data presented in Fig.5.5. The literature values are taken from [33].

of hydrogen and hydrogen-deuterium, we obtain an upper limit of 0.1%, which would result in negligible hydrogen induced losses which are far below the actual absorption losses in deuterium.

3.1.4 The control system

The safe and reliable operation of the new gas system is realized by a combination of the industrial standard SPS system Simatic S7-200 from Siemens and two digital and analog I/O cards from National Instruments. While the SPS system provides the control over all installed valves, the National Instrument (NI) cards are responsible for the readout of all sensor of the system. The control software is written under NI Labview which allows the easy and convenient handling of the gas system and a safe control of all situations during the experimental operations of the UCN source. Fig.3.9 shwos a screenshot of the actually implemented control software. For better visuality pumped

connection lines (< 0 mbar) are coloured green. All other pressurized lines are coloured blue. To asure a safe handling of the deuterium gas, e.g. pumping of deuterium out of the system, a special interlock system is implemented which close immediately the main valve, V1, sensor S1 feels any deuterium.

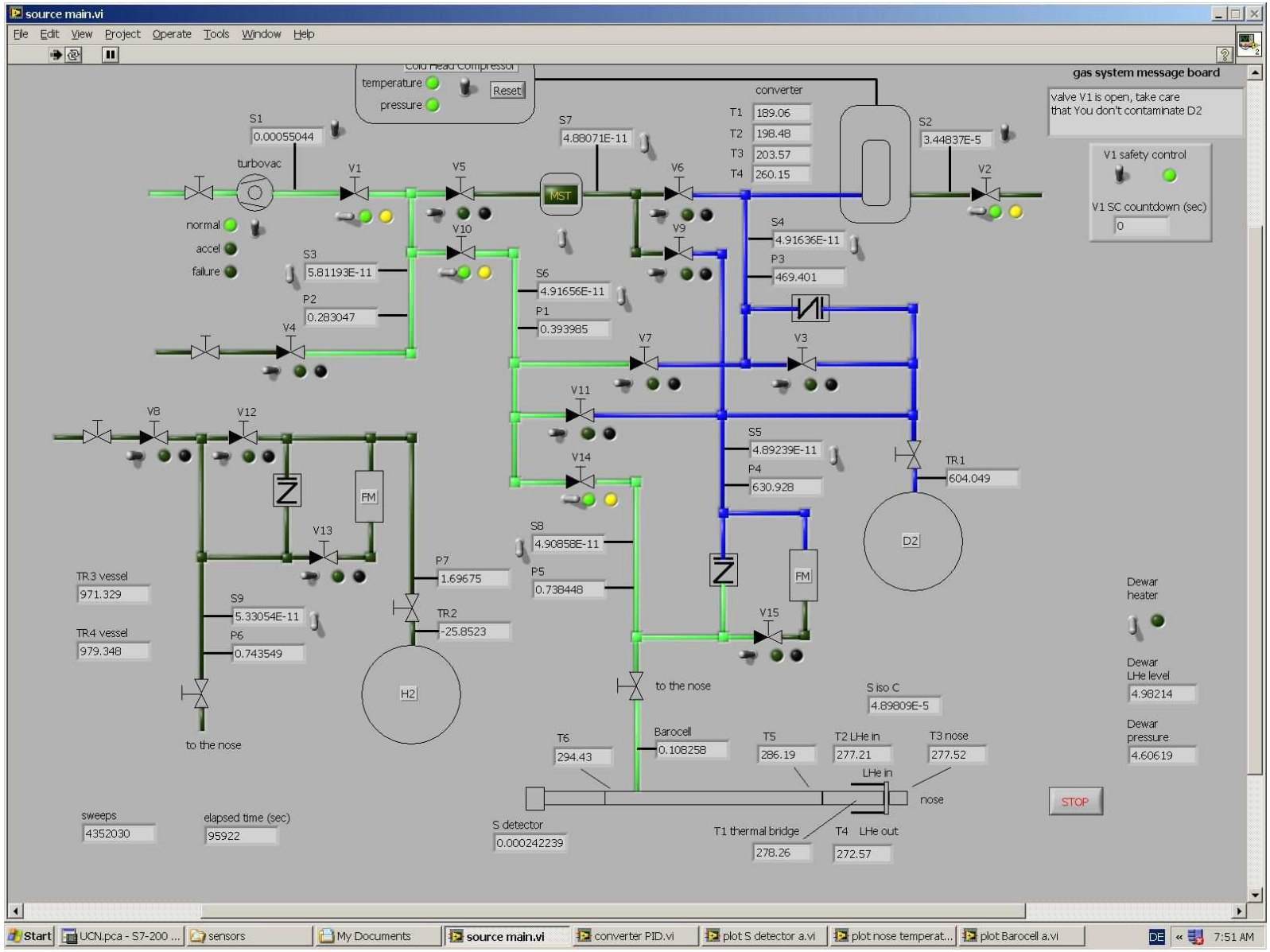

Figure 3.9: Screenshot of the control software of the gassystem and the inpile-cryostat

Chapter 4

Experimental results and their discussion

In contrast to other experimental setups to characterize solid deuterium [36] as suitable UCN converter, the used inpile cryostat at beamport C doesn't give us the oportunity for an optical investigation and monitoring of the growth mechanism of a solid deuterium crystal. Therefore, we are not able to judge the form or the transparency of our crystals. Our main interests in the present topic can be summarized in four questions

- What are the optimal freezing parameters?
- Can we grow crystals in a reproducible way?
- What happens to solid deuterium under radiation exposure?
- Are there any changes in the crystal and crystal performance over time?

To obtain answers, we started to investigate the UCN production by using the pulse mode of the Mainz TRIGA reactor. But it turned out, that due to the fact that the outcoming neutron spectrum of the solid deuterium contains also very cold neutrons, the analysis of the final results in this case is not free from some ambiguity. Therefore, we switched to the constant power mode (100kW) and used the time-of-flight method (TOF) to obtain results sensitive to the neutron velocity distribution. Finally, to show the future prospects of a pulsed UCN source at a low power reactor of the TRIGA type, we performed a storage experiment to measure the available UCN densities in a real storage volume at the experimental area outside of source.

4.1 Experimental investigation of "pulsed" UCN production

The experimental results achieved during one year of pulse mode operation are the main part of another PhD thesis and can be found in detail in [28]. For completeness I will give here only a short summary.

4.1.1 The experimental setup

In order to investigate solid deuterium under pulsed mode operation, a simple setup, consisting of a standard 'nocado' tube (flight path 1.5m), followed by a 90° bend, 0.5m of vertical neutron guide and a detector, was directly mounted to the exit of the UCN source. A sectional drawing of the setup was already shown in Fig.3.1. In order to increase the detection efficiency of the used Cascade UCN detector, see also appenidx A, the UCNs have been accelerated by gravity after the 90° bend half a meter down into the detector.
To freeze out and to keep the solid deuterium at 6K, a 250 liter dewar provides the converter cup with liquid helium. Additionally, a second dewar with 150l of liquid nitrogen is needed to cool down simultaneously the thermal shield of the converter cup. Unfortunately due to the too big inner diameter of the cryogenic supply tubes, the liquid helium flow had to be increased drastically in order to avoid pressure oscillations inside the tubes, due to helium evaporation. The big helium consumption of 20 litres per hour reduced the source working time to 10 hours per day, only.
The time-of-flight spectrum of the pulsed UCN source measured with the CASCADE-U detector triggered by the reactor pulse is shown in Fig. 4.1.
The amount of frozen D_2 in the converter cup was about 4.5 mol. The count rates reach

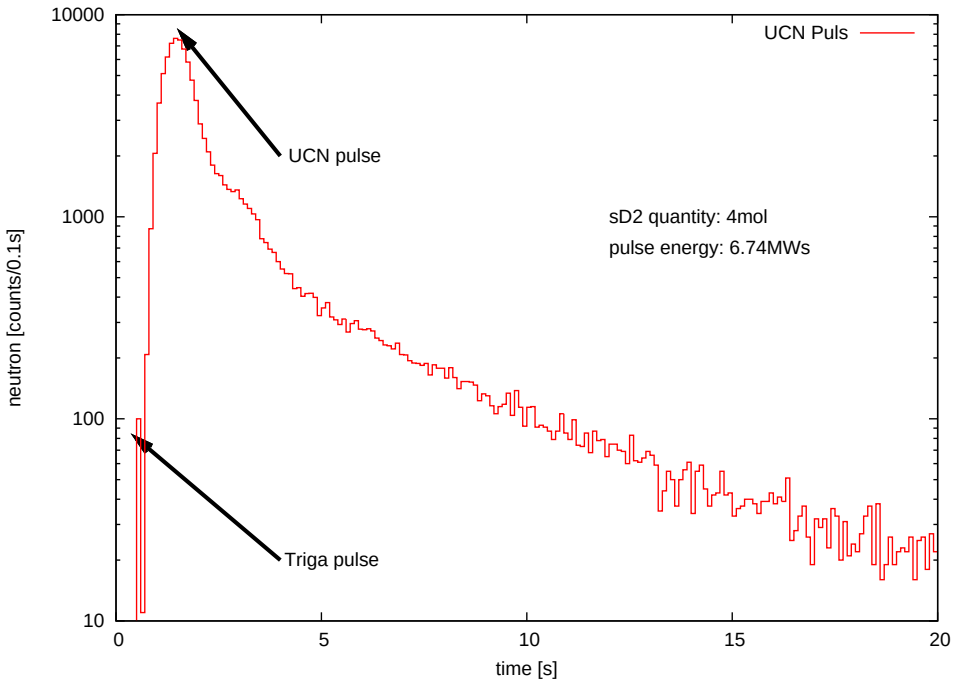

Figure 4.1: Time-of-flight spectrum of a typical UCN pulse from a standard 4 mol crystal.

a maximum at about two seconds after the reactor pulse and then decrease with a time constant of about 5 s. The relatively long tail between 5 s and 20 s indicates that for a small fraction of UCN, the guide acts as storage bottle rather than as neutron guide. The background is completely negligible as it contributes only with a few hundred to

the totally measured counts.

4.1.2 UCN Production versus amount of frozen deuterium

At first, the neutron yield was measured as a function of the amount of sD_2 in the nose. These data were taken without a pre-moderator. As can be deduced from Fig. 4.2, the data points (full diamonds) show an almost linear increase of the neutron yield up to 2 mol of frozen deuterium. For larger amounts, saturation is observed probably caused by the poly-crystalline structure of the converter. During these measurements, the amount of frozen deuterium gas was increased, step by step in small portions of 0.3 to 0.4 mol, while keeping the temperature of the nose constant at about 6 K. A significant increase

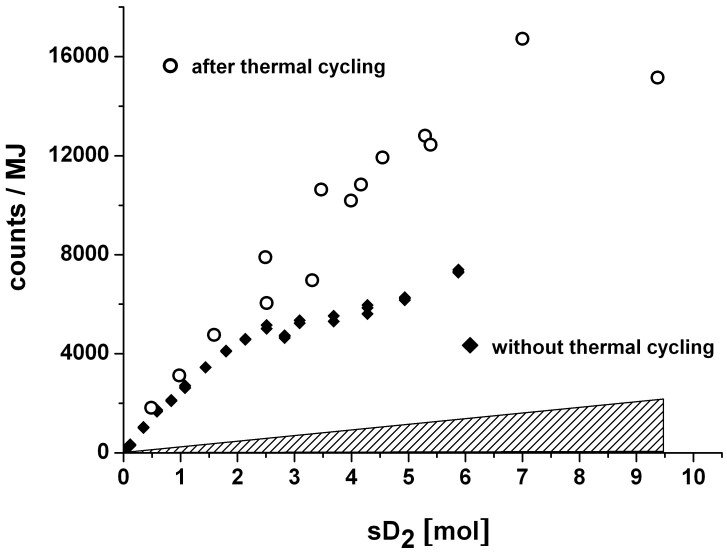

Figure 4.2: Neutron counts (normalized to the pulse energy (MJ)) measured versus amount of solid. Full diamonds: neutron yield obtained by gradually increasing the quantity of sD2 in steps of 0.3 to 0.4 mol, while keeping the temperature of the converter at 6 K, i.e., without thermal cycling. Open circles: thermal cycling of the frozen deuterium results in an increase of the neutron yield. Hatched triangle: Corresponding error bars on the data indicating the reproducibility (10%) of the thermal cycling procedure

of the UCN yield, in particular for fillings beyond 2 mol of sD_2, could be observed after thermal cycling the sD_2 converter in the temperature range between 5 K and 13 K. The open circles in Fig. 4.2 show the resulting count rates for different amounts of frozen deuterium. Obviously, thermal cycling of the crystal improves the source performance. This behavior coincides with a change of its optical properties as reported in [34]. However, the relation between the optical properties of the crystal and the dynamics for UCN production still needs to be determined. After thermal cycling, an almost linear increase of the neutron yield up to 7 mol was found. Beyond 7 mol ($V > 140$

cm^3) the capacity of the nose (V $\approx$ 200 cm^3) is gradually approached with no further increase of the neutron yield. This is caused by the stronger effect of the heat load from thermal conduction through the thermal bridge as well as the heat radiation from the warm neutron guide. Furthermore, the dissipation of this heat load is decreasing with increasing sD_2. The measurements including thermal cycling had been performed a few times for amounts of sD_2 in the range 1 mol $\leq m_{sD2} \leq$ 9 mol in order to proove the reproducibility. Variations observed in the maximal yield indicate a systematic error of 5 % to 10 % as shown in Fig. 4.2.

In Fig. 4.3 details of thermal cycling are shown for 4 mol of sD_2. This amount of

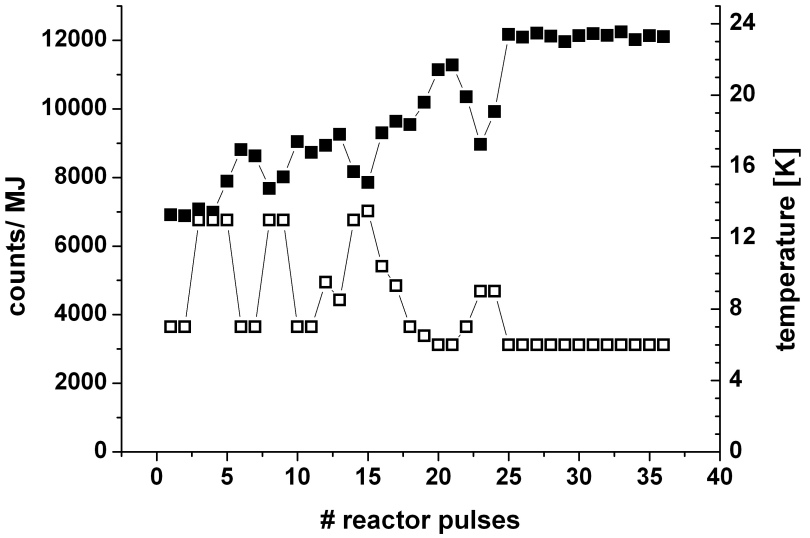

Figure 4.3: Full squares: neutron counts (normalized to the pulse energy (MJ)) as a function of the serial count of reactor pulses. The temperature of the sD2 converter (open squares) was increased and lowered periodically in the range between 6K and 13K. The amount of frozen deuterium was 4 mol. From pulse number 25 on, the nose was kept at 6 K resulting in a constant yield at around 12 000 counts/MJ.

deuterium gas was transferred in one step into the UCN source volume. After freezing out at 6 K (nose temperature), the temperature of the nose was increased and lowered periodically. After four cycles, the measured neutron yield increased by a factor of about 1.7 from 7 000 counts/MJ to 12 000 counts/MJ. Keeping the nose temperature constant from then on, no change in the neutron yield was observed in the following measurements.

4.1.3 UCN production versus reactor power

In a sequence of measurements, the pulse power of the reactor and thus the thermal neutron flux was varied. Figure 4.4 shows the background-subtracted integrated neutron counts as a function of the pulse energy for 4.0 mol of frozen deuterium, demonstrating

precise scaling of the neutron yield versus the thermal neutron fluence. This behaviour was found to persist up to 7 mol of frozen deuterium.

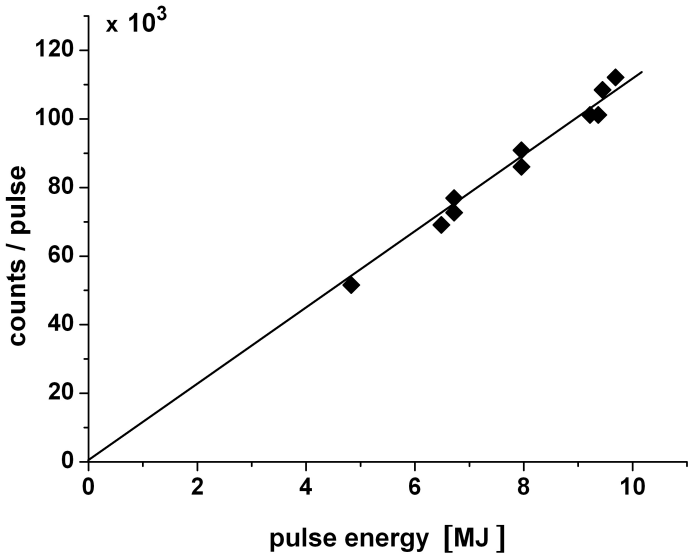

Figure 4.4: Total count rate as a function of the reactor pulse energy in MJ. The amount of frozen deuterium was 4.0 mol. The statistical uncertainties are smaller than the size of the symbols.

4.1.4 Test of an organic premoderator

As already shown in Fig.2.4 the UCN production rate in the sD_2 converter strongly depends on the incident neutron spectrum. Thus, the use of a cold pre-moderator enables to match the incoming neutron spectrum to the phonon excitation spectrum of the sD_2 converter in order to obtain maximum UCN yields.
Two different pre-moderator substances were tested: mesitylene and a mixture of 33 vol% toluene and 67% vol% mesitylene. Methyl derivatives of benzene, such as mesitylene ($(CH_3)_3C_6H_3$) and toluene ($CH_3C_6H_5$) with relatively low melting points (227 K and 180 K, respectively) can be used as an efficient cold moderator, because even at low temperatures the weakly hindered rotational motions of their methyl groups enable the absorption of small amounts of energy from neutrons. In our tests, mesitylene as pre-moderator material turned out to be the most effective pre-moderator, giving about 10% to 15% higher neutron yields compared to the toluene/mesitylene mixture. This substance was filled into the pre-moderator cup (Fig. 3.3, right), which was put on the cold nose with a thermal contact. During the measurements, the pre-moderator was cooled to about 16 K. The average pre-moderator thickness was 15 mm. A peculiarity of solid mesitylene is that it can exist in three crystalline phases [37], which show very different inelastic neutron cross sections [38]. It is very likely that, at a cooling speed of $\approx$ 3 K/min, we produced a mixture of phase I and III. Compared to phase

III, the two other phases have more soft phonon states and thus are more suitable as cold moderator for thermal neutrons. In Fig. 4.5 the maximum UCN yield after ther-

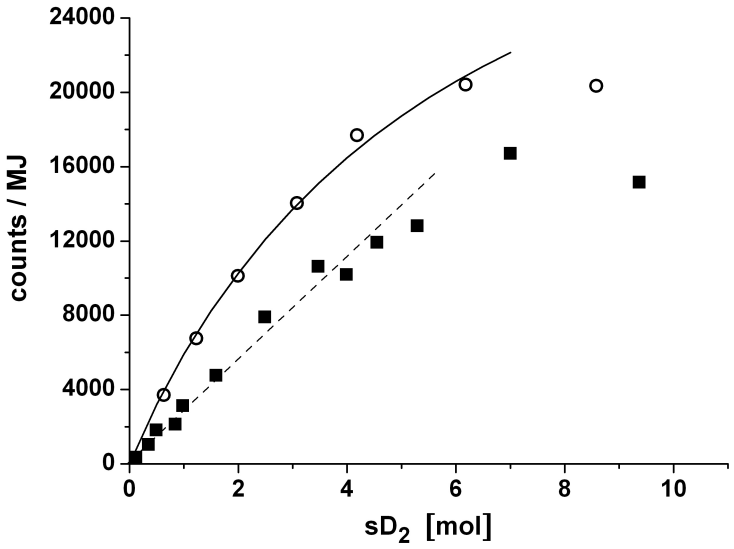

Figure 4.5: Neutron yield (counts/MJ) as a function of the amount of frozen deuterium. Full squares: neutron yield without pre-moderator. The broken line is drawn to guide the eye. Open circles: corresponding neutron yield with mesitylene at 16 K as a pre-moderator.

mal cycling of sD_2 is shown for different amounts of frozen deuterium, measured with and without a mesitylene pre-moderator. The most striking finding is that with pre-moderator, more neutrons are produced. Whereas the gain in neutron yield is about a factor of two higher at low molar values of sD_2 compared to the measurements without a pre-moderator, the neutron yield levels off towards higher amounts of sD_2 resulting in only somewhat higher neutron counts at about 7 mol. The almost linear increase in neutron counts without pre-moderator can be explained by the role of sD_2 which acts both as converter for UCN and as cold moderator for the incident thermal neutrons. Hence, the pre-moderator effect of sD_2 will be more pronounced at larger amounts of sD_2.

4.2 Verification of the neutron optical potential of sD_2

Measuring the very low energy end of the neutron spectrum from a solid $^2H_2$ crystal in an ultracold neutron (UCN) source gives a direct estimate for the material optical potential, see, e.g., Ref.[39], i.e. the averaged or coherent strong interaction potential, which arises in the theoretical treatment of the interaction of very low energy neutrons with materials in terms of refraction, e.g. Ref.[40].
The material optical potential has been measured for most materials using reflectometry

and thin film material transmission and is required for computing the center-of-mass velocity associated with absorption (or other 1/v) cross-section values obtained from transmission data measured with very low energy neutrons, see ,e.g., [41, 42, 43]. A further consequence of the material optical potential is that the energy of neutrons produced within a sample will be boosted as they cross the material boundary, leading to an external spectrum being shifted in energy; such a measurement will give a model independent value of the material optical potential but requires (a) a material that produces significant quantities of very low energy neutrons and (b) measurement of the lower energy limit of the external neutron spectrum. This is possible, and has been carried out, by measuring for the first time the spectrum of UCNs produced in a solid $^2H_2$ converter.
In order to determine the UCN energy spectrum from the superthermal solid $^2H_2$ converter, we used a gravitational spectrometer [44], see Fig. 4.6 which was directly connected to the neutron guide outlet of the inpile cryostat. The 'U'-chicane uses gravity

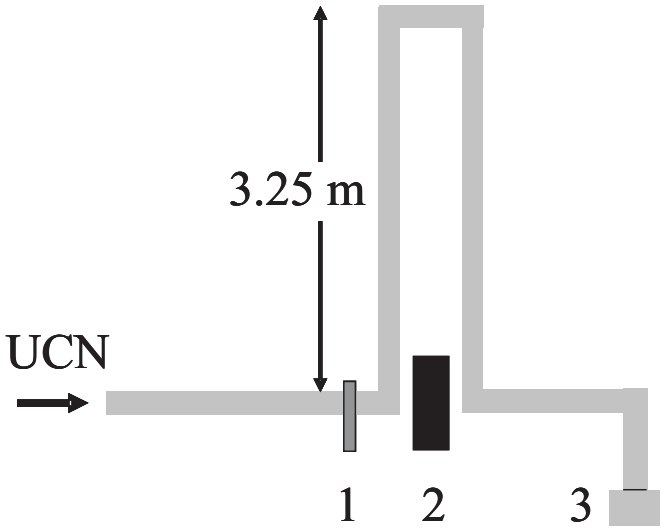

Figure 4.6: Sketch of the gravitational spectrometer; 1: vacuum shutter; 2: 10 cm borated polyethylene; 3: UCN detector with 0.1 mm aluminium entrance window. The detector was shielded against background in a box of 10 cm borated polyethylene (not shown).

to determine the minimum energy of throughgoing UCNs; its height and hence the minimum UCN energy was adjusted by rotation around the neutron guide axis. A vacuum shutter was installed in front of the 'U', cf. Fig. 4.6, to prevent inrush of air into the vacuum system of the cold source during the rotation process.
Unfortunately, about 40 % of the UCNs were absorbed in this gadget. Passing neutrons are registered in a gas counter containing 18 hPa ^{3}He and 12 hPa CO_2 in about 1070 hPa Ar. The detector with its 0.1 mm aluminium entrance window was mounted 60 cm below the beam axis.
This way, gravitation accelerates UCNs such that all of them can penetrate the detector entrance window with a material optical potential of 54 neV. The data were acquired during two consecutive days driving the TRIGA reactor in pulsed mode. Working with

two different solid deuterium crystals might have caused a non-statistical uncertainty, which was taken into account as described below.
Furthermore, it cannot be excluded that certain source parameters may have changed with time leading to a drift in UCN intensity. In order to minimize the influence of such drifts, the sequence of data taking at different heights was determined randomly. Figure 4.7 shows the registered neutrons normalized to the reactor power. Each data

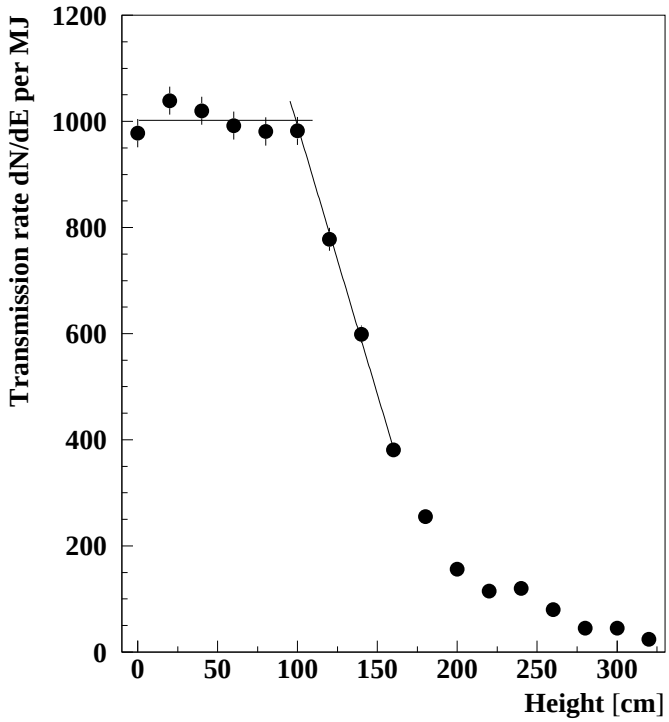

Figure 4.7: Data taken with the gravitational spectrometer. The UCN transmission rates per megajoule of the reactor power after background subtraction are plotted against the vertical height of the gravitational spectrometer. The two lines represent the fit to the data, see text.

point consists of counting neutrons after two consecutive reactor pulses with a time interval between 3 and 10 minutes. In order to determine the detector background during a reactor pulse, two measurements were performed, one before freezing of the $^2H_2$ and a second one with the vacuum shutter closed. The two methods showed identical background rates of 20 counts per megajoule (MJ). The reactor pulses had an energy of typically 6.7 MJ. A 2 % uncertainty of the reactor yield in the pulsed mode at constant released energy was estimated and added in quadrature to the statistical uncertainty. To the left of the data shown in Fig. 4.7, one can see a flat distribution over increasing height of the spectrometer. Above about 100 cm, corresponding to ∼100 neV neutron kinetic energy, the spectrum decreases. This can be compared to the material optical potential of solid $^2H_2$ at 5 K calculated to be about 106 neV [45].

For the analysis, we have introduced a simple model: UCNs gain energy through acceleration in the coherent strong interaction surface potential when they leave the solid

$^2H_2$ converter.
Consequently, the minimal energy of UCN from the new source at the TRIGA Mainz reactor corresponds to the material optical potential of solid $^2H_2$. Above this threshold, the energy spectrum is expected to rise linearly (i.e. quadratically with velocity, v^2) [46]. This can be seen in Fig. 4.7 from the linear intensity decrease of dN/dE with increasing height. The minimal energy of UCNs from the source was determined by fitting a constant A to the flat distribution and a straight line, $y = Bx + C$, to the beginning of the slope at height values above 100 cm, see Fig. 4.7. From the crossing of these two functions, we deduce the minimal UCN energy, i.e. the material optical potential of solid $^2H_2$ at 5 K. The material optical potential is proportional to the density of the material. The density gradient in solid $^2H_2$ at that temperature is about 0.00006 g/cm^3/degree. Uncertainties from the determination of the temperature are thus negligible.
The fitted parameters are $A = 1002 \pm 12$, $B = -10.1 \pm 0.6$ and $C = 2002 \pm 86$. The χ^2 per degree-of-freedom of the two fits were 1.0 for determining A and 0.93 for the straight line. With these values, we find E_c = (99 ± 7) neV, in agreement with expectations. The bend in the spectrum around 200 cm originates from the material optical potential of stainless steel (210 neV) [47]:
UCNs with higher energies are no longer totally reflected under all angles and the U-chicane serves as an energy filter. The small number of events above 210 neV is attributed to scattered neutrons passing this filter.
Using a gravitational spectrometer, we find a minimal kinetic energy of E_c = (99 ± 7) neV for neutrons from a solid deuterium UCN converter. The result is in excellent agreement with theoretical predictions, E_c = 106 neV.

Figure 4.8: Picture of the gravitation spectrometer in action

4.3 Characterization of a sD_2 converter by the time-of-flight (TOF) method

Readig the last section, one could think that the whole job in characterizing the operation parameters of a solid deuterium UCN converter is done. But discussing the results above with physicists, working since many years in the field of UCN science, one obtains two standard questions.

"How can you be sure that you saw UCN?","Did you make storage?" [48]

Today my answer to the second questions would be "Yes, look in section.4.4!"

Besides storage measurements which are not suitable to characterize several different parameter sets of an UCN converter, there exists also another method which allows energy dependent characterization, even at neutron energies higher than the optical potential of existing storage bottles. In this section, I will report on the realization of a time-of-flight setup at the existing UCN source at beamport C at the reactor TRIGA Mainz and also about the detailed energy dependent characterization of the UCN converter based on solid deuterium.

4.3.1 The TOF system

In principle, a TOF measurement can be performed both in the pulsed or in steady state mode of the reactor. In the pulsed mode, the minimal overall length of the flight path is from the geometrical layout (shielding, cryostat, etc., see also Fig.3.1) more than 6 m. In such a long UCN guide, part of the neutrons are repeatedly diffusive scattered back and forth and the neutron guide acts also as a neutron storage chamber.
This leads to a delay of these scattered neutrons in reaching the detector apparently at a lower velocity. In the steady state mode using a chopper for the TOF information, the TOF path length can be chosen to be much shorter, see below.
In order to avoid direct view to the reactor core and to reduce the background from thermal and epithermal neutrons, a horizontal bend section of 45 degree was used, followed by an 1m long straight neutron guide.
For the correct determination of a velocity distribution with the TOF method, we assume a high guide transmission for UCN, *i.e.* a high percentage of specular reflections in the UCN guide system, which is experimentally supported by Ref.[49].
The experimental setup for the TOF measurement, described in Refs.[50, 51, 52], is installed behind this neutron guide; a sketch is shown in Fig. 4.9.
During our investigations two different choppers have been used. Until the end of 2008, a three disc chopper [50] from our colleagues at the Paul Scherrer Institute, in switzerland built the main part of our time-of-flight setup. After its return to switzerland a newly designed single disc chopper was build in Mainz and succesfully implemented in the running characterization of the UCN converter. More details about the design and the construction can be found elsewhere [53].

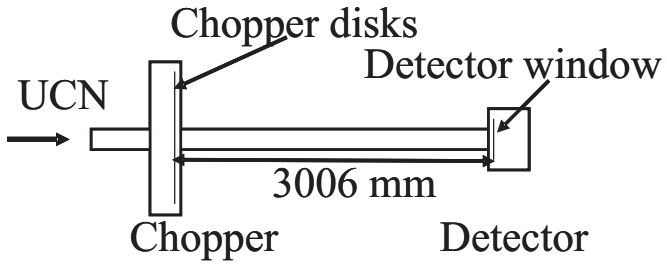

Figure 4.9: Scheme of a standard time-of-flight setup as it was used for the investigation of ultracold neutron converters. As explained in the text, two different disc choppers were used during the measurements.

In Fig.4.9 slow neutrons enter the apparatus and pass through a chopper operating with a duty cycle of 5.5 % [50] or 3% [53], respectively.
They are registered in a neutron detector (^3He or Cascade U, see appenidx A) which was installed directly behind the TOF path ($\approx 1.5m$). The Al entrance windows of both detectors was 0.1 mm thick with an energy barrier of 54 neV (material optical potential of aluminium) and caused some reduction of the detector efficiency.
With this setup, the (averaged) velocity component along the forward direction can be measured [51, 52].
As DAQ system we used either a PCI-BUS module MCD-2 (dual imput multiscaler, FAST ComTec) or the on board DAQ system of the advanced Cascade-U, see also appenidx A. The start signal for the TOF spectra was delivered from the chopper control unit. In the case of the MCD-module for the event (stop) signal, the discriminator output of a Canberra 2015 Amplifier with intergrated single channel analyser was used. The discriminator level was adjusted well above the noise level of the detector signal. The dwell time for the multiscaler was 2.5 ms.

4.3.2 Experimental results and their interpretation

With the installed TOF setup and operating the TRIGA at a steady state power of 100kW we had been able to investigate velocity dependent neutron yield associated with the following issues.

1. UCN and VCN production as function of amount of frozen deuterium

2. UCN and VCN yield as function of temperature

3. UCN and VCN yield as function of the para deuterium concentration

4. Thermal cycling effect

5. Effect of different freezing procedures on UCN and VCN yield

To obtain the velocity dependend informations for UCN, $3.3m/s < v_{axial} < 6m/s$ and VCN, $v > 6m/s$, all TOF spectra were deconvoluted and transformed to velocity spectra with a mathematical routine, described in appenidx C.

1. The amount of sD2

Like in the pulsed reactor mode, we started our investigations on freezing out different amounts of solid deuterium inside the converter cup. The measurement was carried out in two consecutive days. All crystals were frozen with the same procedure as it was done in pulsed mode operation (see chap.4.3.2). Special attention was laid on the preparation of the big quantities of deuterium, e.g., 5mol and 6mol. Thermal cycling was performed for all crystals until the deuterium gas pressure in the neutron guide dropped below 2mbar. Unfortunately, due to the high liquid helium consumption a preparation of a 7mol crystal was not possible.

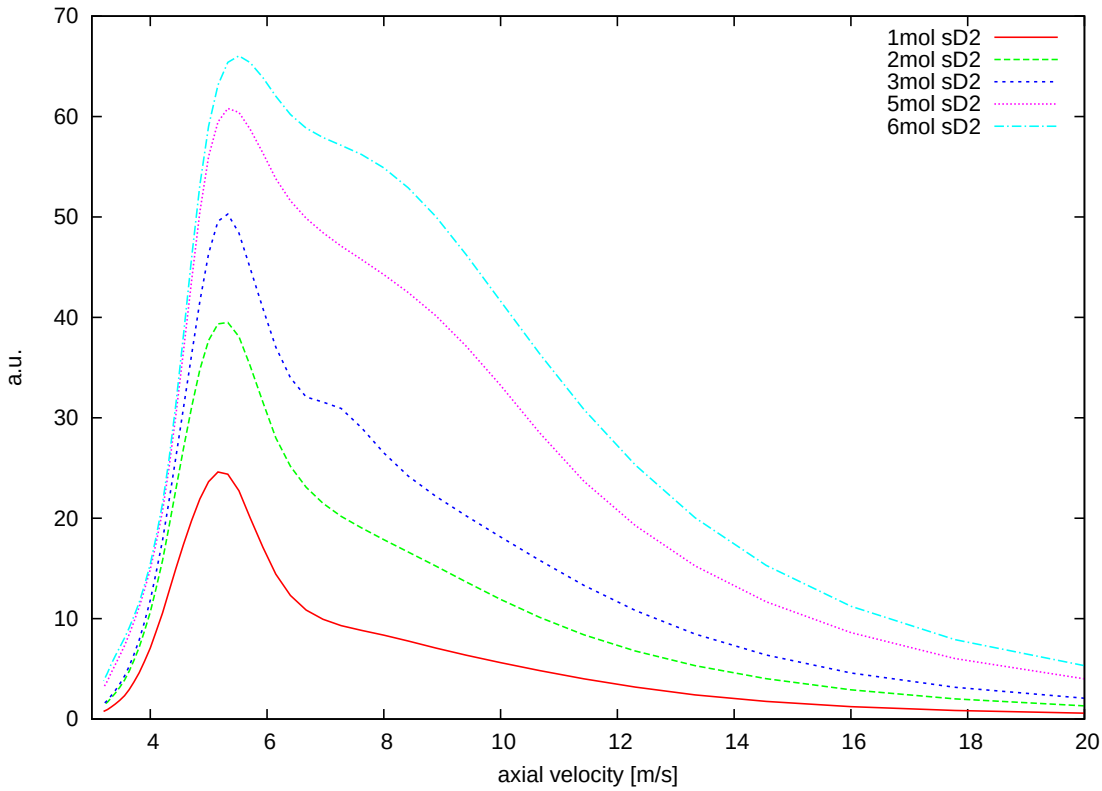

Figure 4.10: Deconvoluted velocity spectra for different amounts of solid deuterium (97% ortho concentration). During the measurement, the temperature of the solid deuterium was kept below 8K. For neutron detection, a ^{3}He detector was used.

Starting from 5.5m/s at one mol a slight shift of the peak velocity up to 5.7m/s at 6mol is visible. Also an increase of neutrons with velocities higher than the boundary velocity of stainlees steel is observed and can be explained by the larger mean free path of these neutrons inside the solid deuterium crystal. Integrating the spectra of Fig.4.10 over the UCN ($v \leq 6m/s$) and the VCN range ($v > 6m/s$) results in the following plot which can be directly compared with the already shown result for the "pulsed" mode operation, Fig.4.2.

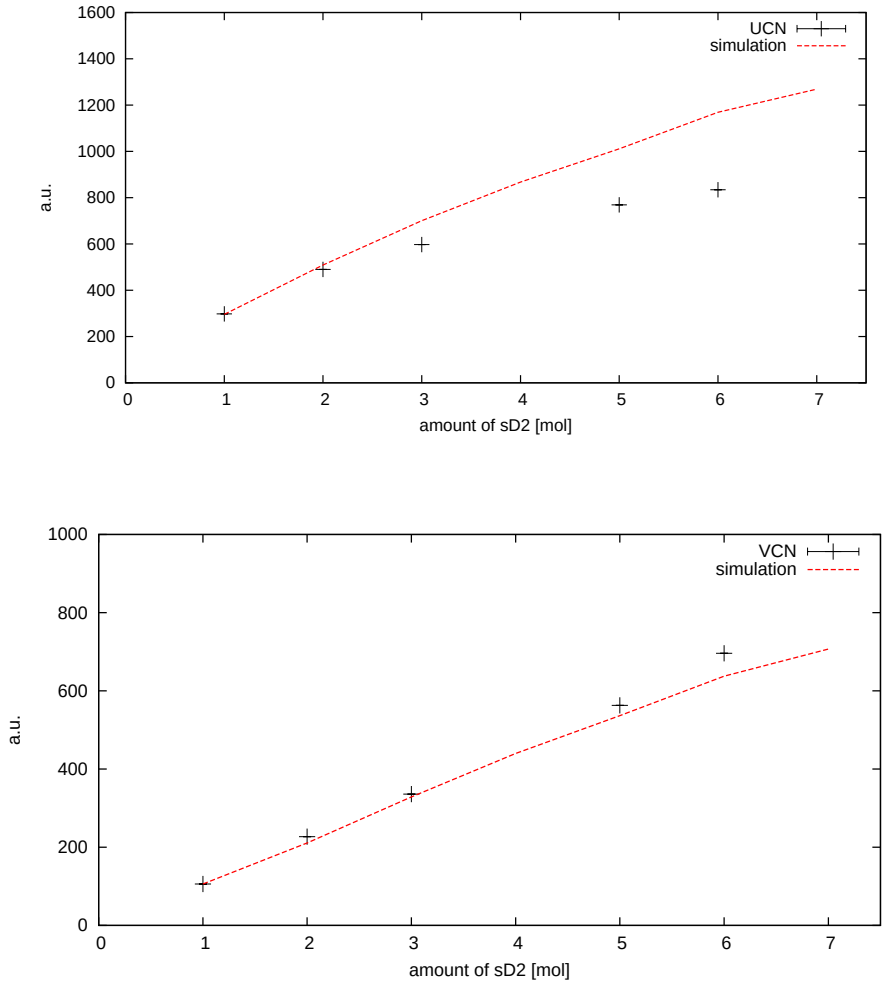

Figure 4.11: Yield of UCN with $v \leq\ 6m/s$ (upper plot, black points) and VCN $v \geq\ 6m/s$ (lower plot, black points) as function of the amount of solid deuterium. The red line represents the data obtained from Monte Carlo simulation (λ_{loss} = 3.5 cm) excluding premoderation inside the solid deuterium.

Supposing no premoderation of the initial thermal neutron spectrum inside the deuterium, we obtain from the Monte Carlo transport simulation code (desribed in appenidx E) a loss mean free path of ≈ 3.5cm (for UCN with v = 3 m/s). The simulated UCN yield as a function of the amount of solid deuterium is plotted in Fig.4.11, red line. Looking on the two plots, we can make already two important conclusions:

1. The detected number of VCN is sligthly higher than the predicted numbers from our Monte Carlo simulations based on a simplified production model. Thus, premoderation of thermal neutrons inside solid deuterium has to be included

2. The mean free path of 3.5 cm is still to high (30% lower yield than expected).

Including premoderation of the thermal neutron spectrum as result of MCNP simulations (see chap.D), one obtains for the UCN production inside the deuterium as function of the amount of solid deuterium the plot shown in Fig.4.12 .

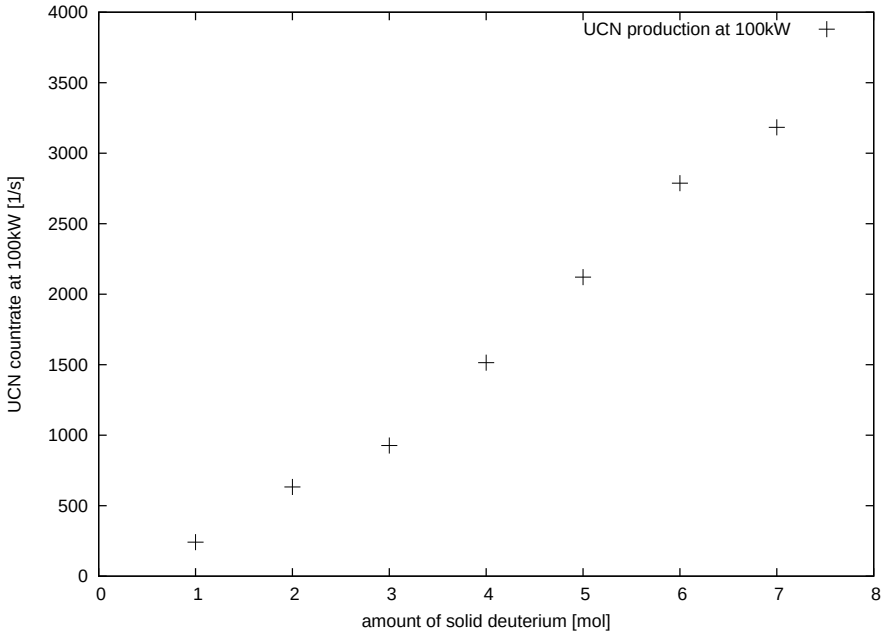

Figure 4.12: Calculated UCN production as function of the frozen amount of solid deuterium. For the caclculation the denity of states measured by Nielsen was used [27].

Together with the new production numbers and by varying the loss mean free path ,we finally get the corrected plot, Fig.4.13.

In order to obtain a good agreement with the measured data, we had to reduce the mean free path drastically down to a value of 3 mm. Due to unknown crystal structure (density, geometry and actual temperature) of our converter and also unknown premoderation cross sections of solid deuterium, we can state at this point only two facts:

1. The UCN yield increases with growing amount of deuterium and saturates above 6 mol.

2. We can give only an estimation for the mean free path of UCN (v = 3m/s) inside the solid deuteriumwhich should be in the range between 3 mm and 35 mm.

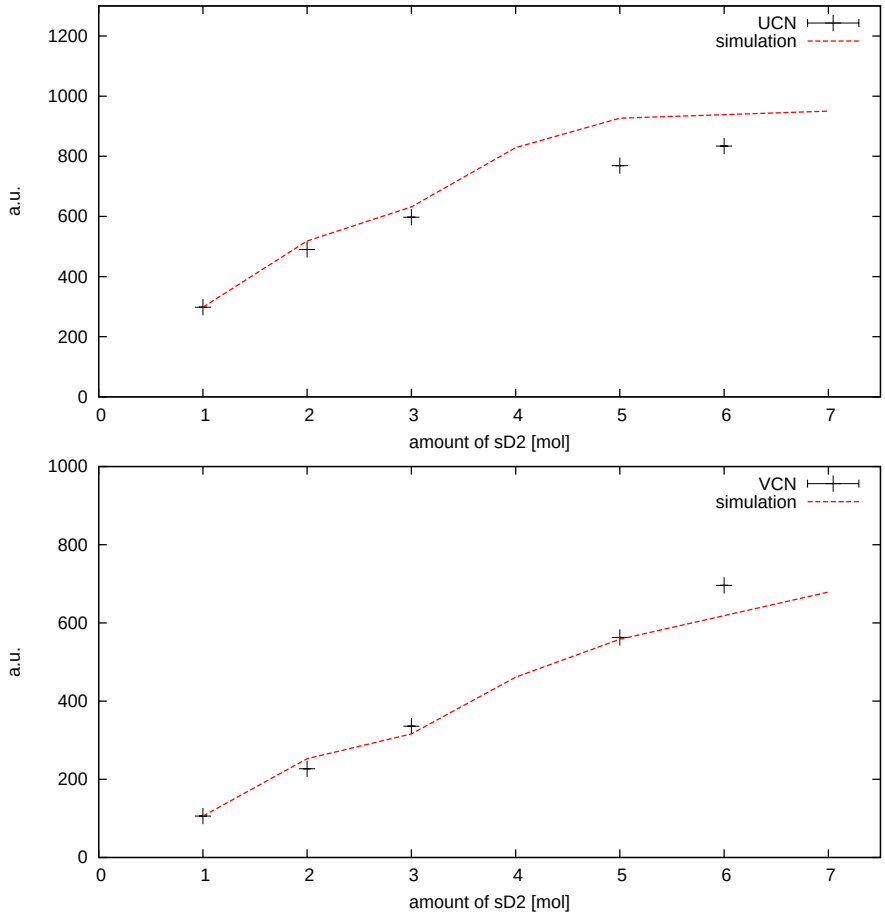

Figure 4.13: Yield of UCN $v \leq 6m/s$ (upper plot, black points) and VCN $v \geq 6m/s$ (lower plot, black points) as a function of the amount of solid deuterium. The red line represents the data obtained from Monte Carlo simulation ($\lambda_{loss} = 3$mm) including premoderation inside the solid deuterium.

2. The temperature of the solid deuterium converter

The principle of detailed balance, eqn.2.20 connects the down- and upscattering cross sections via an exponential function depending on the UCN converter temperature [29]. The upscattering cross section at 5 K is equal to the absorption cross section $\sigma_{th} = 0.519$ mbarn and increases about one order at a temperature around 12 K. Hence, a significant decrease in UCN countrate is expected for temperatures higher than 12 K.
To investigate this behaviour, an appropriate heater was installed on the liquid helium entrance line of the inpile cryostat. The controlled evaporation of helium allowed us to vary the converter temperature between 6 and 15 K. To reach higher temperatures was not possible due to liquification of the deuterium which would have resulted in a sudden evaporation of the deuterium inside the neutron guide Fig.3.2.

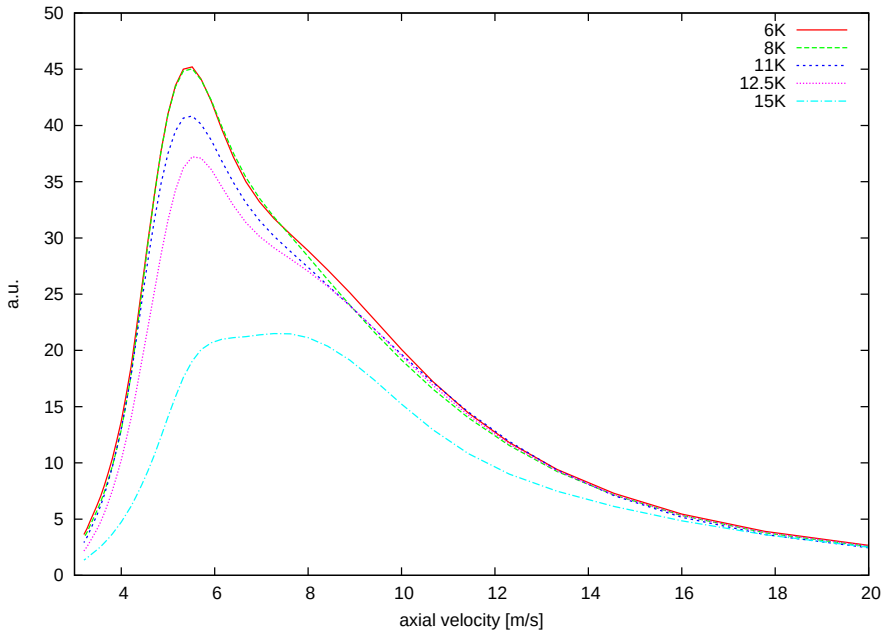

Figure 4.14: Deconvoluted velocity spectra for 1mol deuterium (97.5% ortho concentration) at different temperatures. For neutron detection a ^{3}He detector was used.

Fig.4.14 shows the temperature effect on the TOF spectra taken at 1mol of solid deuterium (2.5% para concentration). In order to avoid temperature gradients inside the deuterium, like in [28], especially a thin layer of solid deuterium was choosen. With increasing temperature a decrease in countrate is visible, which is mainly dominated by the expected decrease of UCN.

Using the cross sections given in [29], we tried to verify the measured data with our Monte Carlo code. Looking on the data we find good agreement up to a temperature of 11 K.
Unfortunately due to instabilities in the temperature regulation of the converter cup,

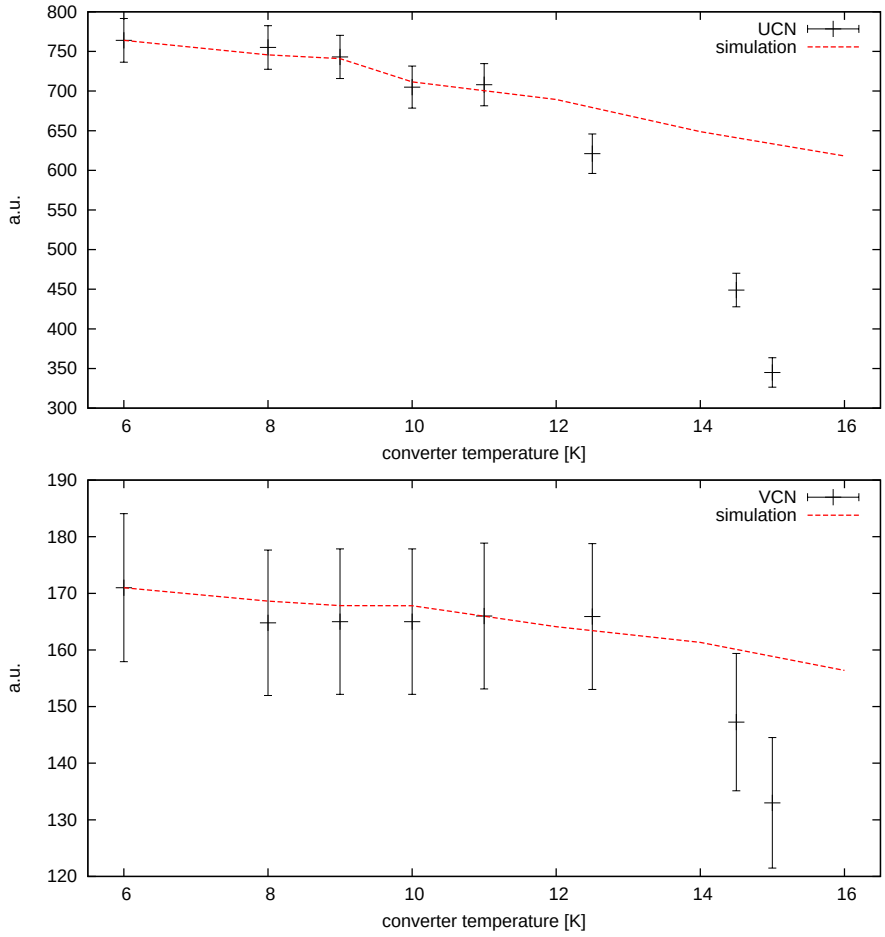

Figure 4.15: Yield of UCN $v \leq\ 6m/s$ (upper plot) and VCN $v \geq\ 6m/s$ (lower plot) as a function of temperature.

especially for higher temperatures, and the resulted increase of the deuterium pressure inside the guide, any theoretical description of the data has to be handled with care. Qualitavively, we can only conclude, that in the temperature range between 6 K and 10 K no significant decrease in the UCN yield was detected. This fact fits quite well to the data already presented in [28].

3. The para concentration

According to [29], UCN can gain energy (7meV) during a zero phonon interaction with a para deuterium molecule by spin flip. This possible interaction decreases considerably the mean free path of UCN inside the converter in the presence of para deuterium. From [29] one can deduce a cross section for pure para deuterium of 78.2 $barn$ ($v = 3m/s$). In thermal equilibrium, "natural" deuterium consists of 33% para deuterium which results in an characeristic upscattering time of only 4.3 ms, corresponding to a mean free path of $\approx 1.3\ cm$ ($v = 3m/s$)

Of course we don't want to keep our produced neutrons inside the neutron guide close to the open converter, but nevertheless produced UCN inside the crystal may strongly suffer from the presence of para deuterium. To reduce the para concentration, we implemented in our new gas system a catalytic conversion system, which allows us a reduction of para deuterium contaminations down to 1.5%. Anyhow, to estimate possible UCN losses in our solid deuterium due to para impurities, we investigated the neutron yield of 1mol crystals for different para concentrations. Of course, the losses inside bigger crystals would be more significant due to the low mean free path, but the repoducibility of crystals bigger than 2 mol is quite questionable and would have led to not predictable results.

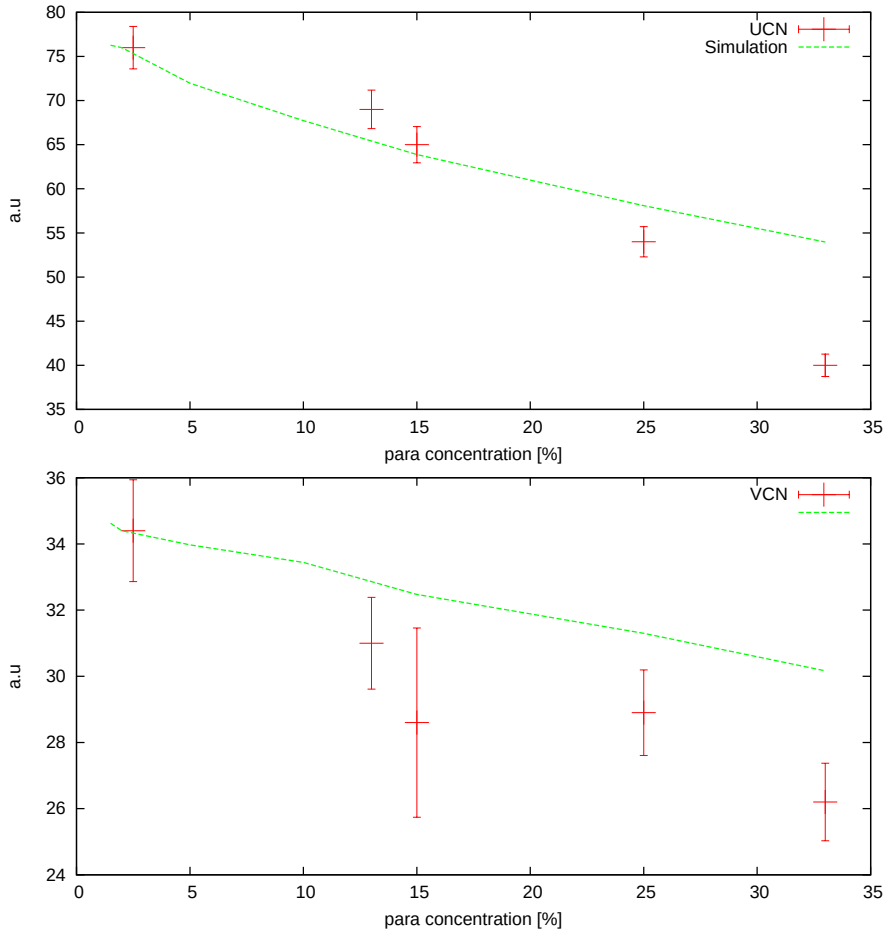

Figure 4.16: Yield of UCN with $v \leq 6m/s$ (upper plot) and VCN with $v \geq 6m/s$ (lower plot) as a function of the para deuterium concentration. The green lines are the results of Monte Carlo transport simulations

The measurements shown have been performed in a four days beamtime. For normalisation reasons, additional data with natural deuterium were taken for each para concentration run.

4. Thermal cycling

In order to get a deeper look inside of the already measured annealing effect of grown deuterium crystals, a series of TOF spectra using a 3 mol crystal were taken. Starting with the first TOF spectrum directly after freezing (deuterium "snow"), four consecutive TOF spectra at 7 K have been taken. Before each measurement the crystal was kept 40 min at a temperature between 10 and 14 K. After every cycling special care was taken in cooling down the crystal slowly enough in order to avoid thermal shocks which could result in cracks, resulting in a decrease in neutron transparency (compare also [36]).

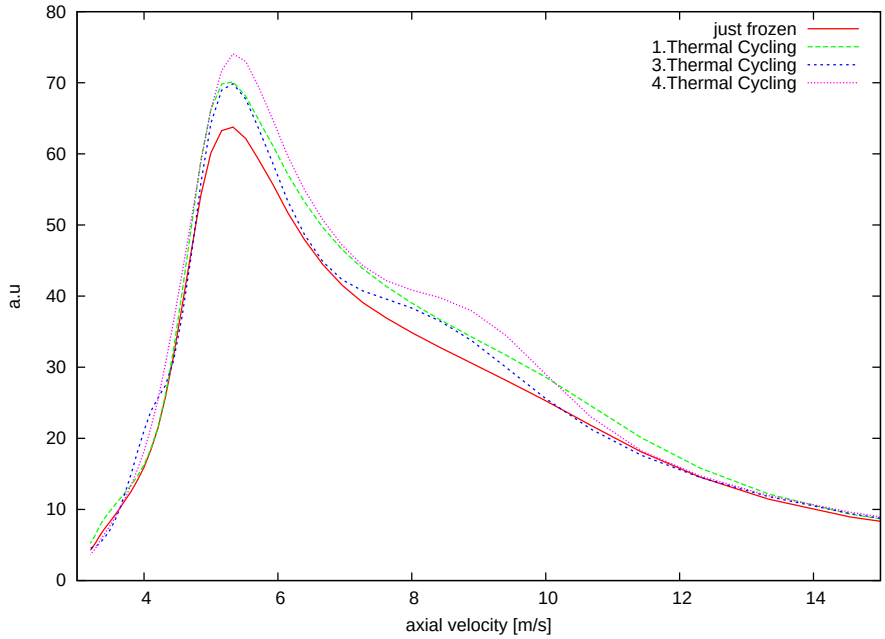

Figure 4.17: Deconvoluted velocity spectra for 3 mol of solid deuterium (96.5% ortho concentration) after different thermal cycling procedures (described in text). During the measurement, the temperature of the solid deuterium was kept below 7 K. For neutron detection, a ^{3}He detector was used.

As in the case of the previous "pulsed" measurements, it was possible to prove the effect of thermal annealing, resulting in a higher solid deuterium transparency for UCN and VCN. The improvement of transparency due to thermal annealing can be explained by a decrease of polycrystal scattering centers. Analogous to the repeated melting and freezing out of snow, the transparency of frozen deuterium could be increased.

Simultaneously with the improvement of the UCN yield, we also found a decrease of gaseous deuterium pressure inside the neutron guide, which can be explained by an increase of thermal conductivity due to the higher bulk density and therefore a lower temperature at the converter surface. Starting from 6 mbar deuterium (after freezing of "snow"), it was possible to reduce the pressure inside the neutron guide down to 2 mbar. After 4 cyclings a gain of 14% in UCN and VCN yield could be reached. Unfortunately, due to our "open" converter cup design, it was not possible for us to increase

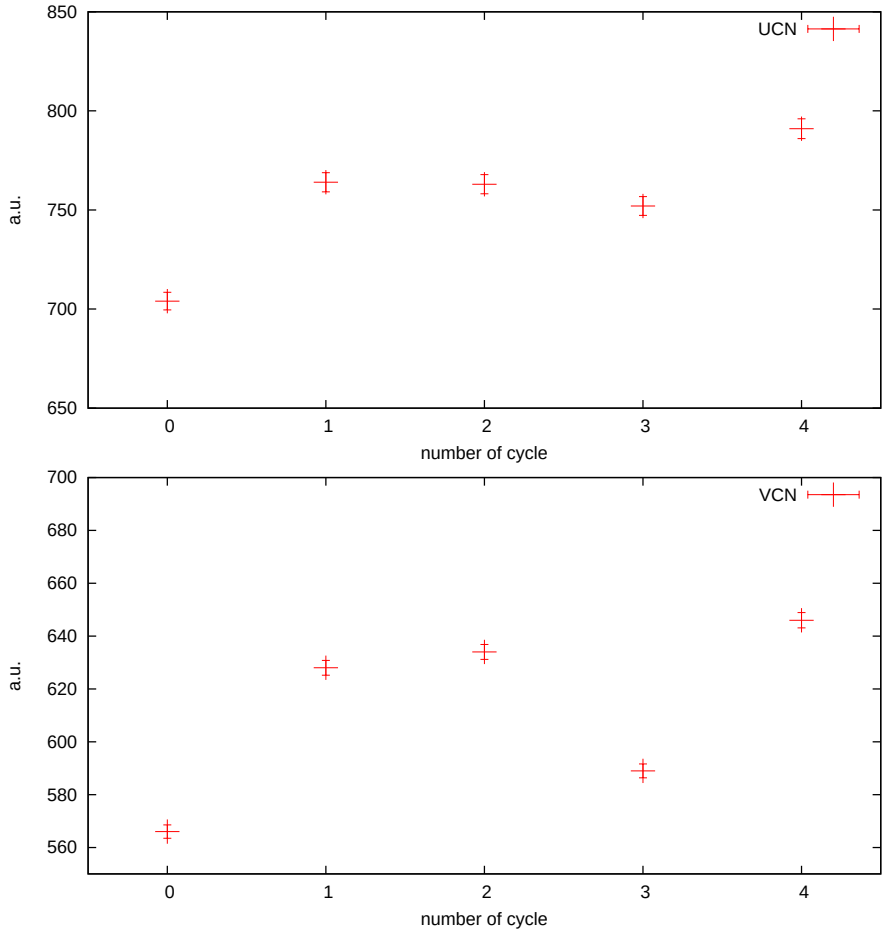

Figure 4.18: Yield of UCN $v \leq 6m/s$ (upper plot) and VCN $v \geq 6m/s$ (lower plot) with increasing number of thermal cyclings (described in text).

the annealing temperature up to 16 K like reported in [36]. Maybe, a thermal annealing time longer than the applied ones would still improve the results, but due to the high helium consumption of the test source, an investigation in this direction was not possible.

5. Freezing procedures

Investigations on the optical and neutron-optical transparency of solid deuterium crystals give quite different results depending on the freezing procedures. By looking on the inelastic neutron scattering results of [36], and their conclusions, one can find that the UCN production doesn't depend on the crystal structure, but certainly that the crystal structure is of great importance for an optimal UCN transmission. Compared to other source concepts (Los Alamos and PSI), the presented open converter design of the UCN source in Mainz doesn't allow to freeze a deuterium crystal from the liquid phase. Therefore, the investigation of different freezing meachnisms from the gas phase was of great importance for us.

Unlike the old deuterium gas system [28], the new gas system is equipped with precision gas flow controllers from MKS, which have been especially calibrated to control small gas flows of deuterium. Within the range of zero and one standard liter per minute (1slm) it was possible to vary the crystal growing time for one mol of deuterium between 25min and a few hours. In agreement with [36], we can compare two different freezing procedures:

"Pulsed" freezing is realized by keeping the converter all time at a temperature of around 6 K. For freezing, the neutron guide with the converter volume are repeatedly filled with deuterium gas up to a pressure of 45mbar. Due to the cryopumping effect of the cold converter cup, the deuterium resublimates at its cold parts and the pressure drops down to the saturation pressure, corresponding to the converter temperature. This procedure is repeated until the final quantity is reached or until the converter (solid deuterium crystal) is not able to pump anymore gas from the guide volume. A further increase of converter thickness is then only possible after several thermal cyclings (see also section about thermal cycling). Using this method, it is possible to build a 4 mol crystal in 4 hours including a minimum of 3 thermal annealing breaks with a duration of 25 min each.

"Continous freezing" keeps the deuterium gas pressure constant inside the system during freezing.

During the first investigations (1.The amount of sD_2 and 2.The temperature dependence) the solid deuterium crystal was prepared with the above described freezing method. Comissioning the new gas system for beamport D, it was later possible to investigate also deuterium crystals grown under constant gas flow, which is called from here on "continous freezing".

Looking on the obtained TOF spectra in Fig.4.20, the increase in UCN yield by resublimating solid deuterium under a constant gas flow is quite significant. The pressure inside the guide doesn't increase beyond 3 mbar during the whole freezing procedure and drops down to 2 mbar at the end of this procedure. Further decrease in deuterium pressure in connection with a small increase in countrate can be realized by a carefully prepared thermal annealing at a temperature of 14 K.
From [36], a further improvement in UCN transmission was expected by variation of the deuterium gas flow resulting in a solid deuterium growth speed in the range of 3 mm/h. This speed corresponds to a constant gas flow of $\approx$ 0.2 slm and to a freezing time of 8 hours for 4 mol of solid deuterium.
As already mentioned, the huge helium consumption of the UCN source in combination with 250l dewars allowed only preparation and measurement times of max. 11hours. Therefore, at the beginning of our research, the detailed investigation of slower freezing speeds was impossible.
To overcome this problem, a 1500 l helium dewar was installed close to the source setup. Together with home made liquid helium transfer lines, we even reduced the helium consumption to a minimum of 14 l per hour. This way it was possible, to freeze out crystals over night and to keep the same crystals for measurement periods of three days.

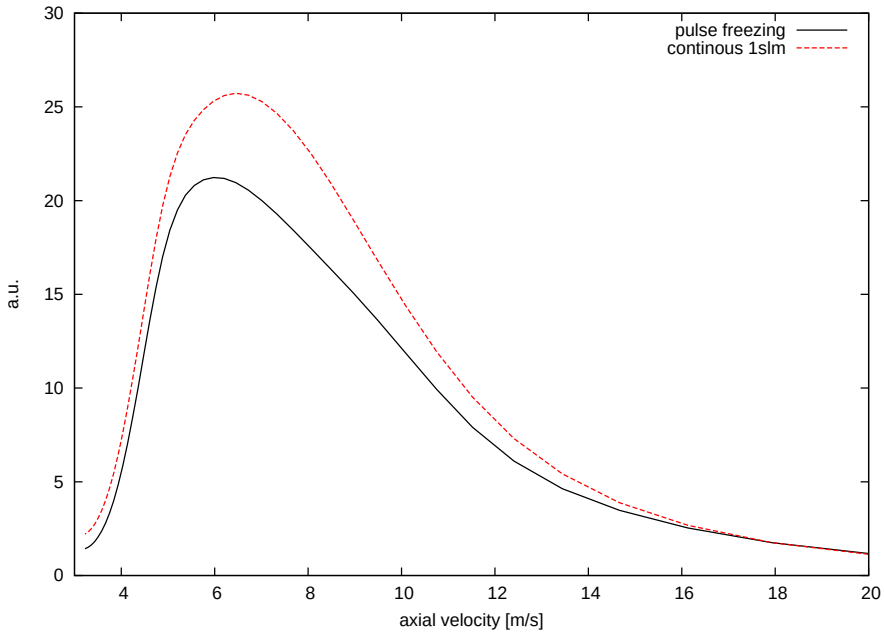

Figure 4.19: Time-of-flight spectra of two 4 mol solid deuterium crystals grown with i. pulse freezing (black curve) and ii. continous freezing (red curve) procedure. The initial deuterium parameters for both crystals were the same $c_{ortho} = 97.5\%$. The measurements were performed with the single disc chopper [53] and the standard Cascade U detector (appenidx A).

Test of the new cryogenic cooling arrangement

During the test of our new liquid helium transfer lines, we made a standard freezing procedure at a deuterium gas flow of 1 slm (Fig.4.20, red curve). In order to improve the UCN yield, as done before, a thermal annealing process at a temperature of 14K was performed. Instead of a further increase, the UCN yield (Fig.4.20,green curve) and even more the VCN yield dropped down. To compare the measured result with previous measurements performed at the same deuterium parameters but with the old transfer line, the black curve in Fig.4.20) is added. Looking on the converter temperatures obtained with both lines, one can finally conclude, that temperature oscillations in the range of one Kelvin, which had been the result of using the old transfer line, obviously damage the crystal (cracks) and decrease the UCN transmission. This effect could be demonstrated during annealing of the crystal (Fig.4.20,green curve) which also resulted in not controllable temperature oszillations due to the evaporation of liquid helium.

Finally, we prepared a 4 mol crystal with a deuterium gas flow of 0.25 slm, which is close to the growth speed mentioned in [36]. The TOF spectrum of this crystal is also presented for comparison in Fig.4.20. In contrast to the crystal prepared at a deuterium flow at 1 slm, the UCN ($v \leq 6m/s$) yield increased only sligtly. A considerable increase ($>10\%$) is only visible for neutrons at higher velocities ($v \geq 6m/s$).

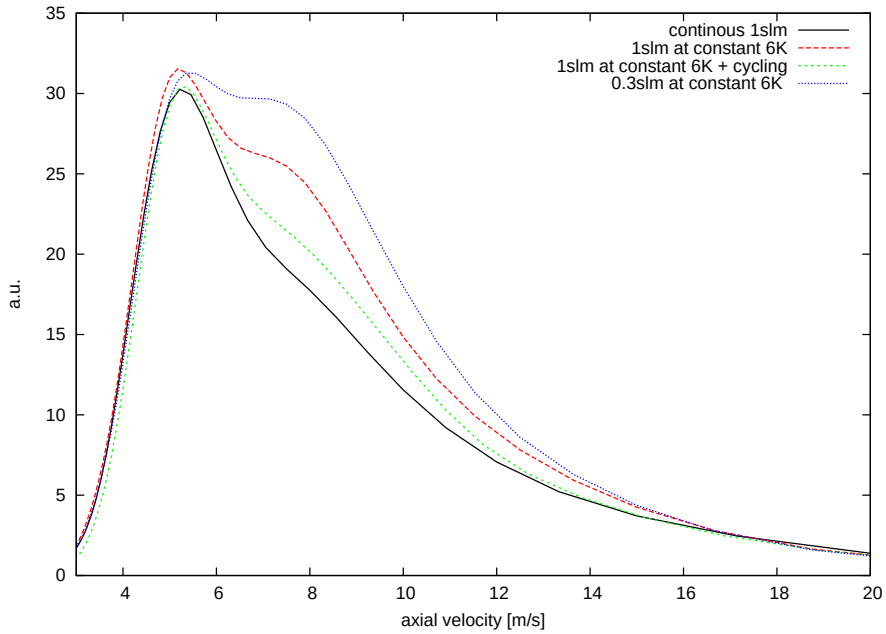

Figure 4.20: Time-of-flight spectra of three 4 mol solid deuterium crystal, grown with different freezing procedures and freezing speeds. Black curve: carefully annealed 4 mol crystal, grown with 1 slm and temperature oszillations of around 1 K (old transfer line). Red curve: 4 mol crystal grown with 1 slm and temperature oszillations of around 0.1 K (new transfer line). Green curve: 4 mol crystal (red curve) after carefuly annealing at 14 K (40min). Blue curve: 4 mol crystal grwon with 0.3 slm and temperature oszillations of around 0.1 K (new transfer line). The measurement were performed with the described single disc chopper [53] and the advanced Cascade 2D detector (appenidx A).

A formula for a good deuterium crystal

1. Grow the converter crystal at low speed ($\approx 3mm/h$) and low pressure

2. Avoid big temperature gradients inside the crystal

3. For crystals grown with these hints thermal annealing is dangerous, at least if one cannot control precisely the temperature.

6. amount of sD2 at optimal freezing parameters

At the end of our investigations, knowing now a formula, how to prepare reproducible deuterium crystals with high UCN yield at the discussed converter setup, it is worth to repeat our first investigations on the UCN yield as a function of amount of solid deuterium. Therefore, to complete the two measurements at 1 mol and 4 mol, a deuterium crystal with the amount of 7 mol ($\approx$ 140 cm^3) was prepared with the above described growing parameters.

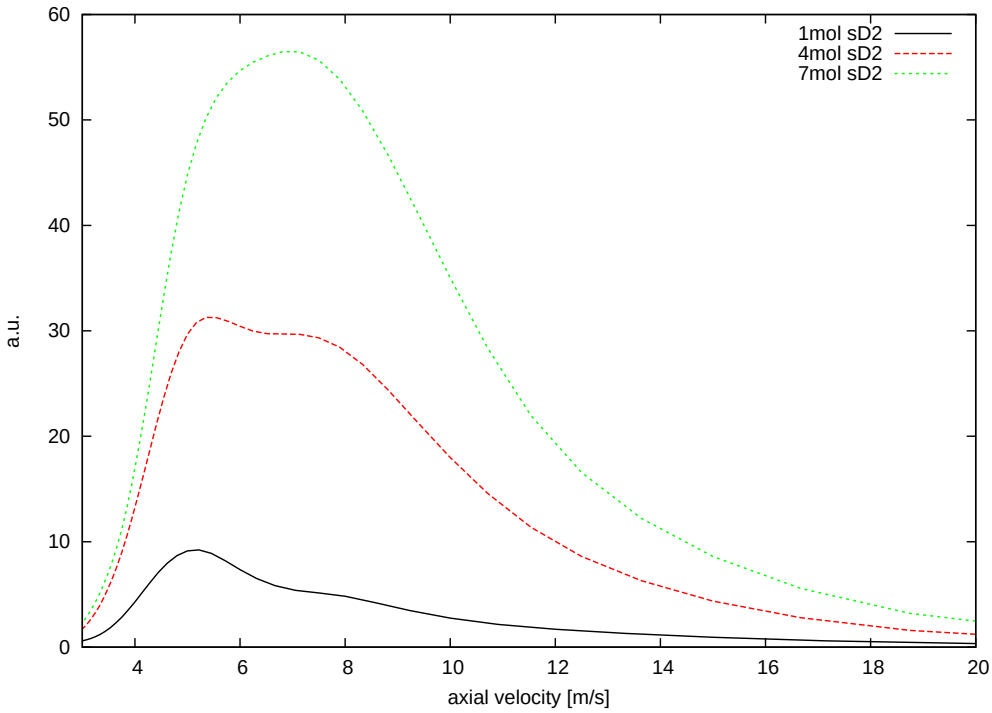

Figure 4.21: Deconvoluted spectra for different amount of sD_2, frozen with a speed of 0.3 slm at a temperature of 6 K. Black curve : 1 mol sD_2, red curve : 4 mol sD_2, green curve : 7 mol sD_2

Integrating the obtained TOF spectra (Fig.4.22) over the UCN ($v \leq 6\ m/s$) and VCN ($v \geq 6\ m/s$) region we get the following plot for the UCN and VCN yields as a function of the amount of solid deuterium.

In contrast to the data taken in 2007, the new data give almost a factor of 2 higher UCN yield. Including the premoderation of solid deuterium, the data is in fairly good agreement with a UCN mean free path of $\lambda_{loss} = 23 \pm 5mm$. This value fits also to the estimated allowed region for the mean free path given above in the first investigation.

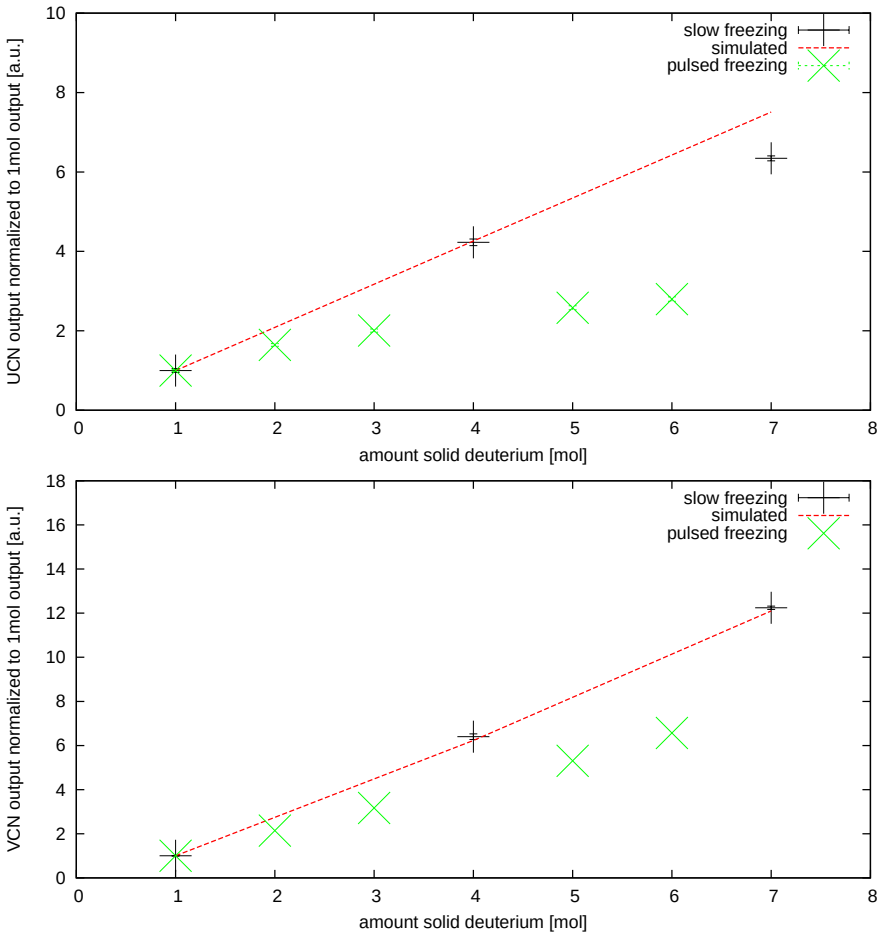

Figure 4.22: Measured UCN $v \leq 6m/s$ and VCN $v \geq 6m/s$ yields at beamport C. The data are normalized to the yield measured at 1 mol of solid deuterium. The black points in both plots represent the yield for the "slowly" prepared crystals (0.3 slm). The red lines are the result of Monte Carlo transport simulations with a UCN mean free path of ($\lambda_{loss} = 23$ mm). The green points (the old data from 2007) are only shown for comparison.

4.4 First storage of ultracold neutrons at TRIGA Mainz

Lookíng into literature dealing with ultracold neutrons, the reader is confronted all time with the same standard definition:

"Ultracold neutrons are neutrons which can be stored in material bottles"

Hence, if you want to convince ultracold neutron physicistss who don't believe in time-of-flight measurements, you have to perform a storage measurement.

The first storage of ultracold neutrons in a real storage setup (one storage volume, two shutters) was performed at the UCN source C in Nov.2007.

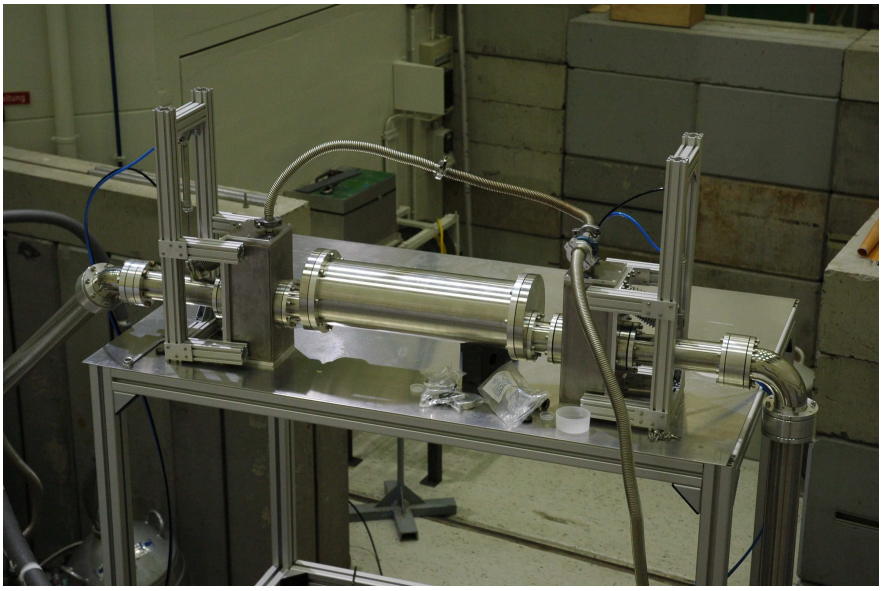

Figure 4.23: Storage setup installed at the UCN area C one meter higher than the UCN source exit

The storage volume was built from an electro-polished stainless steel tube (nocado) with an inner diameter of 150mm and a length of 500 mm. Two electro-polished stainless steel flanges reduced both ends of the storage vessel to the standard UCN guide diameter of 66mm. Together with two standard UCN guide pieces (length 100 mm), which were used as connection between the storage vessel and the shutters, the overall storage volume was $9520 \pm 20 cm^3$. The short time scale of the incoming UCN pulses (see also Fig.4.1) and the bad transmissivity for the direct neutron beam aborted the use of standard UCN shutters commonly applied at the steady state UCN source at the ILL in Grenoble. With the goal to build a fast closing shutter system ($\approx 100 ms$) with high transmissivity for direct beam and negligible UCN leackage, we designed new stand alone shutters. A detailed description of the technical realisation can be found in chap.7.4.
Fig.4.23 shows the final storage setup installed at the UCN area C at the reactor TRIGA

Mainz.
In order to perform a realistic UCN experiment, the storage vessel was not directly connected to the source exit. By using a feeding guide (length 1.9m) and two 45 degree electro-polished stainless steel bends, it was possible to vary the height of the storage setup with respect to the level of the source exitt (zero level).
In Fig.4.23 UCN enter from the left side via the feeding guide and the first UCN shutter (filling shutter) into the storage volume. After some predefined storage time ($t_{storage}$) the UCN are emptied via the second shutter (emptying shutter) and are detected with the Cascade-U A (not visible in the picture).
To increase the detection efficiency, the Cascade-U detector is installed with a 90 degree stainless steel bend and an UCN guide half meter length below the storage vessel. This way UCN, which would not overcome the Fermi potential of the detector entrance window (54neV), are accelerated by gravity and gain an energy of ≈50neV.
During the first storage experiment, the timing of the shutters with respect to the reactor trigger was realized by using three digital I/O ports of the existing SPS control system [28], which was implemented to control the deuterium gas handling system. One complete storage cycle was split into three parts:

1. Close emptying shutter and wait for reactor trigger

2. After reactor trigger, close filling shutter after a predefined filling time t_{fill}

3. After some predefined storage time $t_{storage}$, open emptying shutter

Processing several 1.5$ reactor pulses with a maximal energy release of 6.4 MJ and a time interval between 6 and 10 min, we obtained for two storage setup positions, level zero (storage vessel located at the same hight as the source exit) and 1m above the following storage curves (Fig.4.24). Unlike steady state UCN sources, pulsed UCN sources reach the optimal density of storable neutrons in a few seconds after the initial reactor pulse. The characteristic filling time of our setup was 2.5s. A more detailed optimzation of the filling time can be found in Fig.4.25.

Introducing a simple fit curve according to

$$N(t) = A \cdot exp^{-\frac{t}{\tau_1}} + B \cdot exp^{-\frac{t}{\tau_2}} \tag{4.1}$$

where A and B are amplitudes and τ_1 and τ_2 are the storage times corresponding to different velocity regions, see also eqn.4.2, one can extract the final results given in Tab.4.2.

Looking on the storage times for both configurations one can realize the change in the velocity distribution to lower velocities by lifting the whole storage volume one meter higher than the UCN source exit. Concerning the minimal UCN energy (106 neV, see also chap.4.2) leaving the solid deuterium converter and the maximal storable energy (190 neV, stainless steel), we estimate an averaged velocity of the stored neutrons at zero level of 5.5 m/s. According to

$$\frac{1}{\tau} = \frac{A}{4V} \cdot \overline{v} \cdot \overline{\mu}_{eff} \tag{4.2}$$

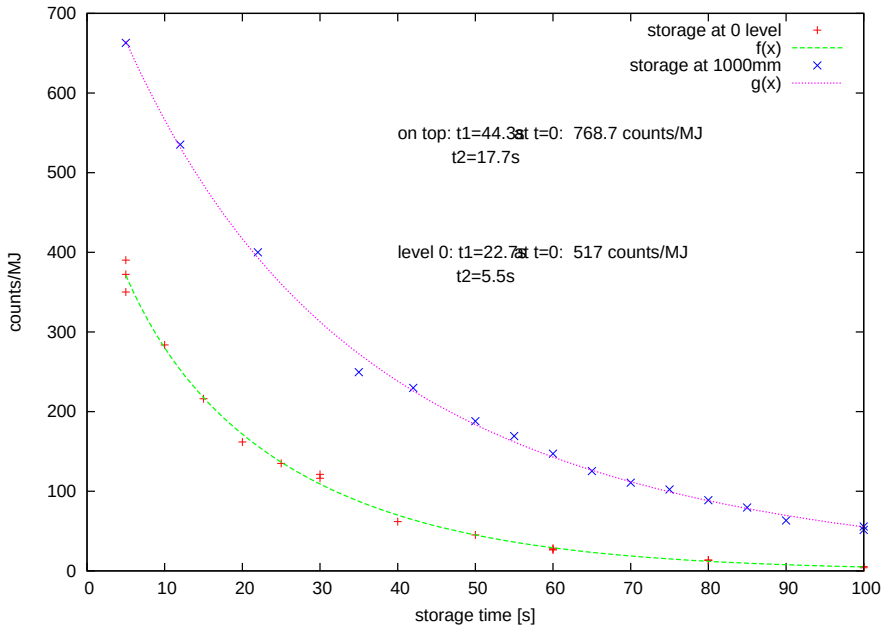

Figure 4.24: First storage curves obtained for two different storage vessel positions. Lower curve (red points): vessel positioned at the same height as the source exit ≈900 mm over flor(zero level). Upper curve (blue points): vessel positioned 1m higher than the "zero" level. Both measurements used the same filling time of 2.5 s and the same solid deuterium crystal of 4 mol. Freezing was performed in "pulsed" mode at a temperature of 6 K including 2 thermal cycles of 20 min each.

position	zero level	1000mm
τ_1 [s]	22.73	44.3
τ_2 [s]	5.5	17.7
$\rho(0)[cm^{-3}]$	0.54	0.81

Table 4.1: Fit results of the measurements shown in Fig.4.24. The given densities $\rho(0)$ are extrapolated (not corrected for detector efficiency) at t=0 and measured at a reactor pulse power of 10 MJ.

with A the inner surface of the storage vessel, V the volume of the storage vessel, $\overline{v}$ the averaged velocity of the neutrons inside the vessel, $\overline{\mu}_{eff}$ the averaged effective loss per bounce and assuming a deceleration (100 neV) of the average velocity down to 3.4 m/s we evaluate in a rough estimation a storage time at the lifted position (1000 mm) of 36.7 s. Without knowledge of the real velocity and angular distribution and neglecting the velocity dependence of $\overline{\mu}_{eff}$, this calculated result is in fair agreemenet with the measured storage time of 43.7 s. Assuming for the lower storage time, τ_1 an inititial velocity of 7 m/s and a deceleration of 100neV we would expect a storage time τ_1 one meter higher of roughly 10 s.

As conclusion of the first storage measurement, one has to point out that we had been

able to convince the UCN community of the succesfull test of a solid deuterium UCN converter in Mainz.

4.4.1 Final UCN densities for UCN experiments

Finally, after two years of investigation and optimization of freezing and working parameters of the realized solid deuterium UCN converter principle, a reproducible UCN density available at the present UCN facility "UCN C" should be given.

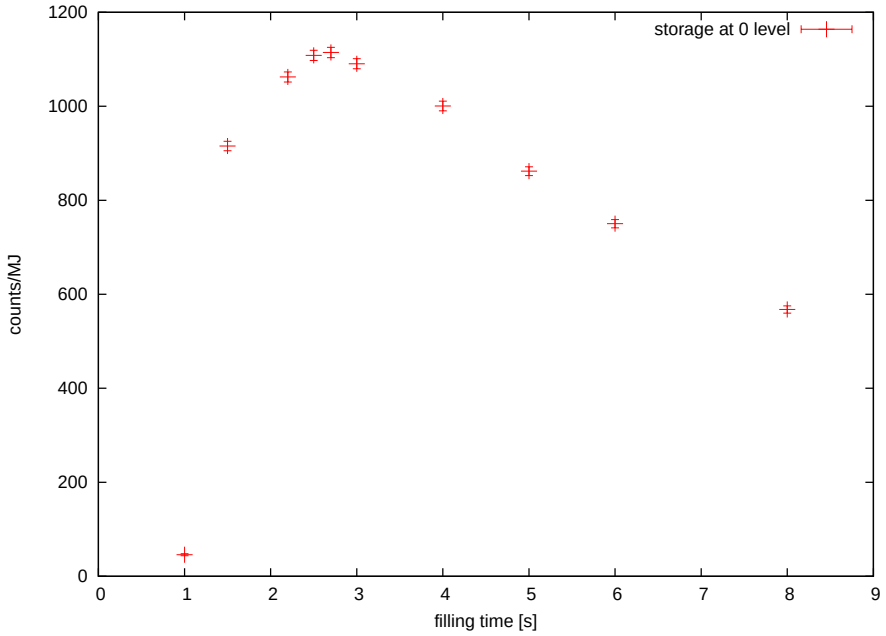

Figure 4.25: Determination of the optimal filling time. The storage time $t_{storage}$ was kept constant at 5s over the whole measrement run. UCN converter parameter: 4 mol solid deuterium, 97.5% ortho deuterium, growing speed 300 sccm, converter temperature 6 K .

To determine the "final number", we installed exactly the same storage setup which was used already two years ago, at the neutron guide exit of "UCN C". The only thing which had to be changed was the shutter control system. Due to the no longer availability of the TUM SPS system, we implemented a small portable USB digital I/O card from National Instruments, which could be controlled via standard NI Labview routines, instead.
As detector, we used a Cascade-U detector with 2D readout structure (appenidx A).
To compare our results with the former measurements, presented above a solid deuterium converter with the same amount of 4 mol was prepared with the latest formula. By keeping the storage time ($t_{storage} = 5s$) constant , the filling time according to the following plot (Fig.4.25) could be optimized in the first measurement run.
Like two years ago, a filling time of 2.5 s was found to be optimal for the existing setup.

After this optimum backdiffusion into the neutron guide system get's more and more important. A decrease of the neutron density due to the short storage time of the whole converter and guide system is visible ($\tau_{storage} \approx 4s$).
In comparison with the TOF spectrum obtained with both shutters in open position, the maximum density is obtained almost one second after the peak maximum of the UCN pulse, shown in Fig.4.1.

UCN density as a function of solid deuterium amount

In order to demonstrate again the gain of UCN yield as a function of the UCN converter volume, a two storage measurements (see also Fig.4.26) were performed with a 4 mol and 7 mol deuterium converter.

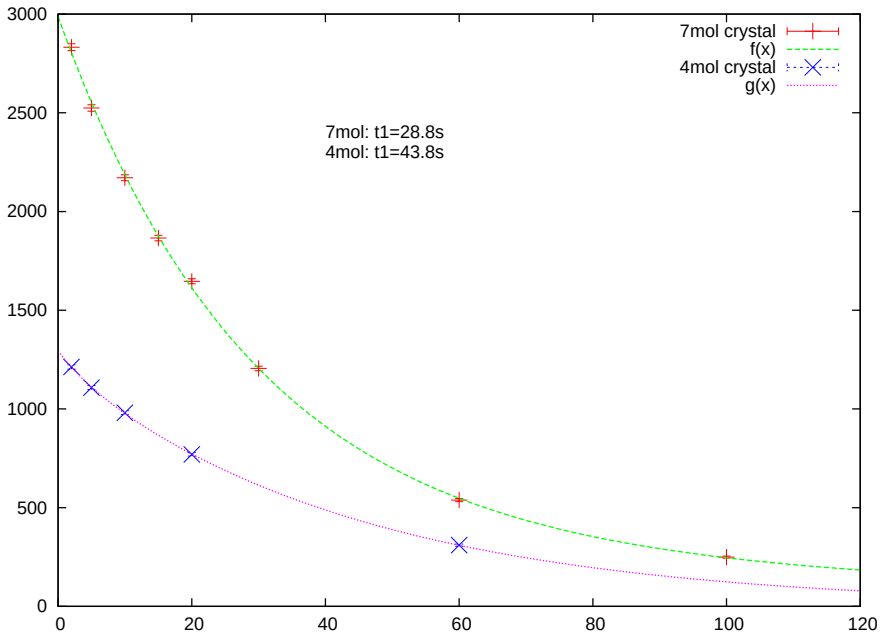

Figure 4.26: Storage curves for two different amounts of solid deuterium. Upper curve (red points): 7mol solid deuterium frozen at 300 sccm at 6 K. Lower curve (blue points): 4mol solid deuterium frozen at 300 sccm at 6 K. Both crystals are prepared without thermal cycling.

As summarized in Tab.4.2, a gain of 2.3 was found for the larger converter. Remembering a UCN ($v \leq 6m/s$) gain factor of roughly 1.5 in Fig.4.22, this result shows clearly the influence of faster neutrons ($6m/s \leq v \leq 8m/s$) on the UCN density (VCN gain factor = 2).

Therefore, for further increasing the density of storable neutrons at levels above the source exit, high qualitative neutron guide parts and especially high qualitativ bent parts are extremly needed.

A new 45 degree bent part for the deflection of neutrons

As shown in Chap.7.5, neutron guides, made from round glass tubes coated inside with materials of high neutron optical wall potential, can certainly improve the performance of the UCN and even more VCN transmission in comparison with the standard used nocado stainless steel tubes.
Exchanging the first 45 degree nocado bent (bent radius ≈150 mm) at the source exit with a glass bent (larger bent radius) coated with 500 nm NiMo (90/10) should result analoque to our experiences with 20 degree glass bents (see also appenidx E, Fig.E.2), in a higher UCN density inside the storage volume.

Figure 4.27: Picture of the new 45 degree glass bend coated inside with 500 nm NiMo(see chap.7.5) installed at the UCN source yield.

As can be seen in Fig.4.27, the idea of a 45 degree glass bent (bent radius ≈ 500 mm) was realized and tested in the frame of the latest storage experiments. Unfortunately, the inner diameter of the used glass tubes was sligthly smaller (64 mm) than the standard nocado tubes and therefore the final UCN values have to be corrected.

The analysis of the shown curves, Fig.4.28 and Fig.4.26 give us the final densities of:

Correcting the last density of 3.75 with smaller guide cross section (diameter 64mm) of the glass bend to a standard guide cross section of 66mm, gives a final density of

$$\rho(0) = 3.75 \cdot \frac{33^2}{32^2}\ \mathrm{UCN} \cdot cm^{-3} = 4 \cdot\ \mathrm{UCN} \cdot cm^{-3} \tag{4.3}$$

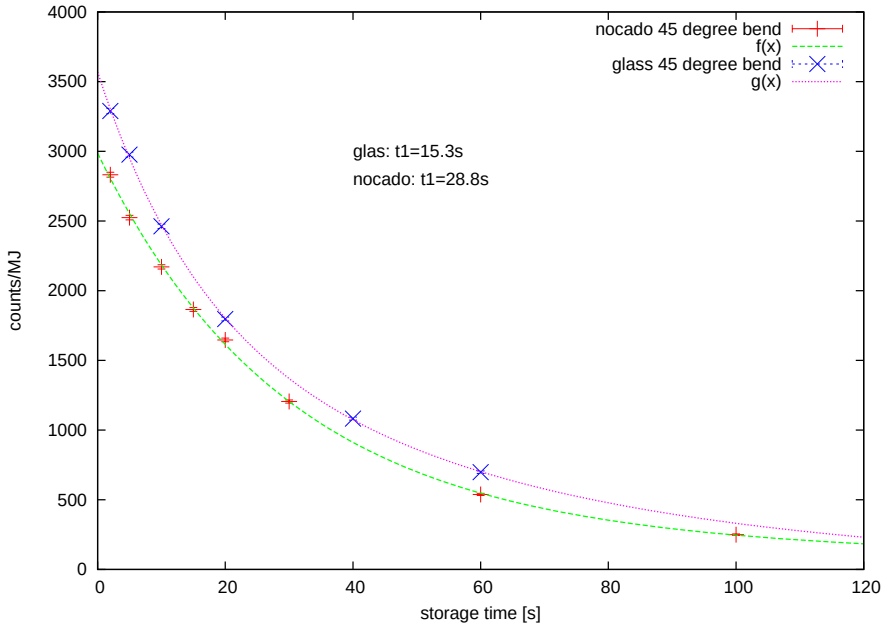

Figure 4.28: Storage curves for different 45 degree bent parts, installed at the source exit. Upper curve (blue points): 45 degree glas bend coated inside with 500 nm NiMo(see chap.7.5). Lower curve (red points): 45 degree electro polished stainless steel bend (nocado). Both measurements were performed with the already described 7 mol crystal.

	4mol	7mol	glass bend
τ_1 [s]	4.5	28.8	15.28
τ_2 [s]	43.8	146	56.25
$\rho(0)[cm^{-3}]$	1.36	3.13	3.75

Table 4.2: Fit results of the measurements shown in Fig.4.26 and Fig.4.28. The given densities $\rho(0)$ are extrapolated, no detector efficiency correction at t=0 and measured at a reactor pulse power of 10 MJ.

4.5 Conclusion and outlook

To summarize the presented results, I would like to state, that in the last beamtime we learned the important things about freezing and handling of solid deuterium .
Keeping loss mechanisms as low as possible, it is quite obvious from the data presented, that the most significant influence on the UCN yield is related to the crystal structure and therefore the freezing procedur. For optimal freezing parameters (97.5% ortho concentration, converter temperature 6 K, deuterium gas flow during freezing 0.3 slm, and a temperature stability of 0.1 K), we obtained reproducible crystals with a mean free path of 23 ± 5 mm for UCN with a velocity of 3 m/s. The error is mainly dominated by the not well known premoderation effect of solid deuterium and the converter geometry.
Another important aspect, which could be demonstrated during the experiments was the influence of the temperature stability of the system, which in agreement with the investigations presented in [36], results in cracks inside the crystal causing in a decreased UCN mean free path.
Referring on the finally achieved corrected UCN density of 4 UCN/cm^3, reached in the experimental area of beamline C, we had been able to show the performance of the available UCN source in Mainz in comparison to the existing most powerful UCN sources in the world (5 UCN/cm^3 [54]). Furthermore I would like to point out, that the so far reported densities in vicinity of the ultracold neutron source at Los Alamos differ considerably from the obtained densities in the storage volume of dedicated setups [54, 55].

Chapter 5

Hydrogen, a candidate as prospective converter material for a superthermal UCN source with an inclined channel

Presently, all new superthermal sources under construction are based on two converter materials, namely, solid deuterium or superfluid helium. Investigations in the direction of other promising candidates like solid oxygen or heavy methane [56] haven't shown so far the expected UCN yield. Besides these substances which can be used as converter due to their dedicated phonon dispersion curves, hydrogen has been forgotten so far. First production calculations for solid para hydrogen [26] indicated a ten times higher UCN production in comparison with deuterium, which is connected to the ten times higher incoherent scattering cross section of $\sigma_0 = 79.7$ barns. Additionally, hydrogen is also an excellent premoderator for thermal neutrons and therefore increases also the UCN output due to the better precooling of the initial neutron spectum.
Unlike all the other converter materials mentioned , hydrogen has one big drawback. Its absorption cross section of $\sigma_{th} = 0.334$ barns is more than 600 times larger than the absorption losses in solid deuterium and hence reduces the mean free path of UCN inside a solid hydrogen crystal down to 1 mm.
Due to the idea of using a hydrogen premoderator in front of our new UCN converter at beamport D, we started to investigate the neutron yield from solid hydrogen at the very cold part of the neutron energy spectrum in order to understand the premoderation capabilities.

5.1 Some basics and calculations for solid hydrogen as converter

Similar to deuterium, hydrogen can be in two different rotation J = odd (ortho) and J = even (para) states. The ground state J = 0 (para) is separated from the first

excited ortho state (J = 1) by an energy of 14.7 meV. In thermal equilibrium at room temperature, hydrogen consists of 75% ortho and 25% para hydrogen. Unlike deuterium, the natural conversion from the ortho to the para state at low temperatures ($\approx$ 10 K) is a factor of 31 higher, and follows the simple differential equation

$$\frac{dc_{ortho}}{dt} = -k \cdot c_{ortho}^2 \tag{5.1}$$

with c_{ortho} being the ortho concentration and k = 0.019 h^{-1} [57] the conversion constant. Thus, a conversion from natural to pure para hydrogen with a concentration of 99% would need only 40 h.

UCN Production

Knowing the phonon density of states of solid para hydrogen, Fig.5.1, we are able to calculate, according to the UCN production calculations performed already for solid deuterium (see also chap.2.3.1), the UCN production inside a thin hydrogen film.

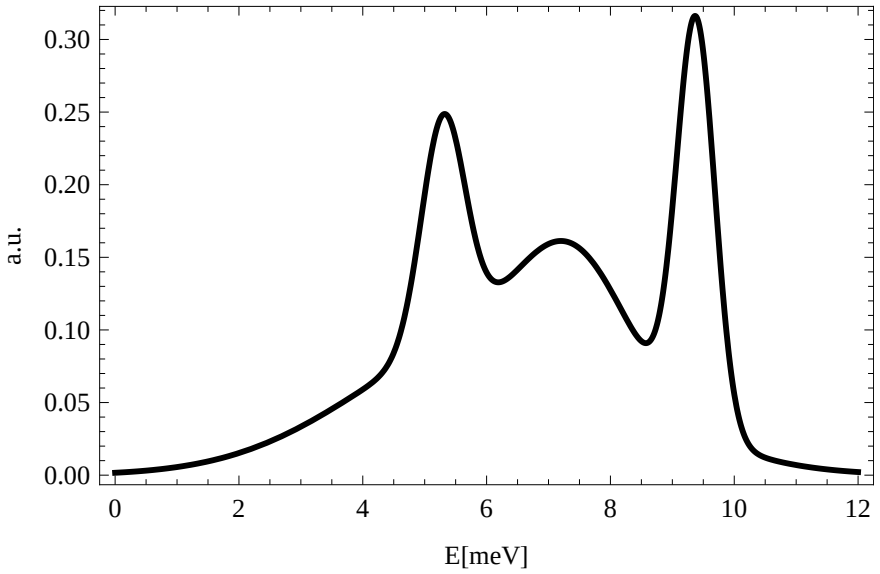

Figure 5.1: Approximated phonon density of states of solid para hydrogen at 6 K.[26]. The related dispersion measurements can be found elsewhere [27]

Integrating over the initial thermal neutron flux at beamport C of the TRIGA Mainz and the final UCN energy spectrum (0-190 neV), we expect an UCN production of

$$P = P_{atom} \cdot N_{sH} = 18382 \cdot 10^{-24} \cdot 2.63 \cdot 10^{22}\ 1/cm^3 s = 483\ /(cm^3 s) \tag{5.2}$$

for 1cm^3 of solid hydrogen at 100kW reactor power. Here P_{atom} represents the Production calculated with eqn.2.21 and N_{sH} the number density of hydrogen in solid phase. Including the premoderation (Fig.5.2) of the neutron spectrum inside the hydrogen layer

with the help of detailed MCNP calculations, this number increases by about a factor of 2.6 to

$$P = 1254\ /cm^3 s \tag{5.3}$$

All *MCNP* calculations have been performed using the available neutron scattering

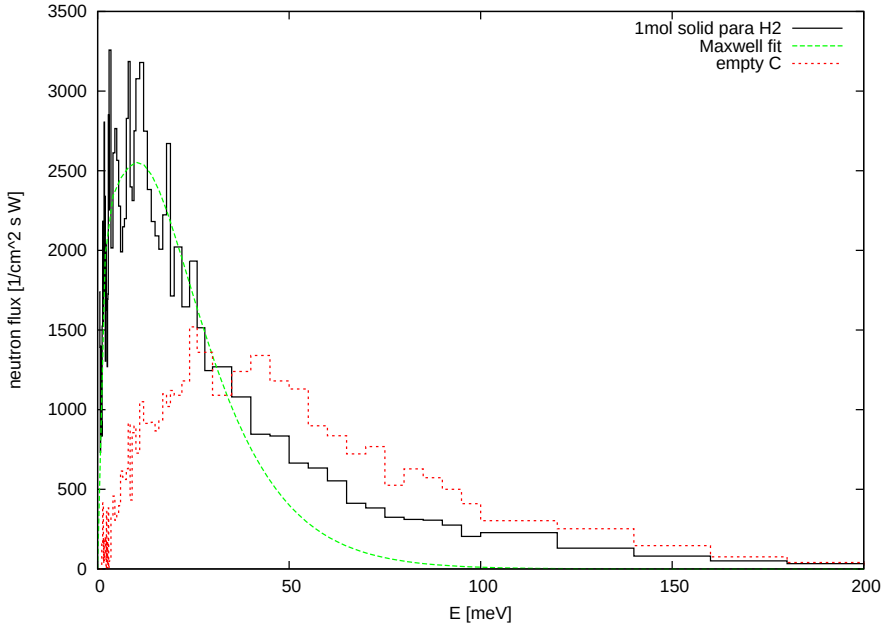

Figure 5.2: Premoderation of the thermal neutron spectrum (red curve) inside 1mol of solid para hydrogen (black curve). As result of the incomplete premoderation of the initial neutron spectrum a fit with two Maxwell functions (green curve) including two moderator temperatures was used. From the fit we obtain $T_1 = 22K$ and $T_2 = 135K$.

cross section for liquid hydrogen. As presented in Fig.5.3, these *MCNP* results may be only seen as a lower limit, because of the not available scattering data for solid hydrogen.

5.2 Experimental results

Together with our colleagues from the Technical University of Munich, first tests of hydrogen as UCN converter were performed in the end of 2007 [28] driving the reactor in pulsed operation. By applying the TOF method in further experiments, we had been able to measure for the first time the neutron velocity distribution from a solid para hydrogen converter. Looking for a suitable premoderator for our new source at beamport D, we started more detailed investigations on solid hydrogen in the beginning of 2009. Using again the already desribed TOF setup, we investigated natural as well as para (90%) hydrogen solids as a function of the amounts of frozen gas.
The natural hydrogen was taken directly from the bottle and filled in the premoderator gas vessel of the new gas system. Due to the high absorption cross section of hydrogen we had not been afraid of any contamination by other gases. Therefore we

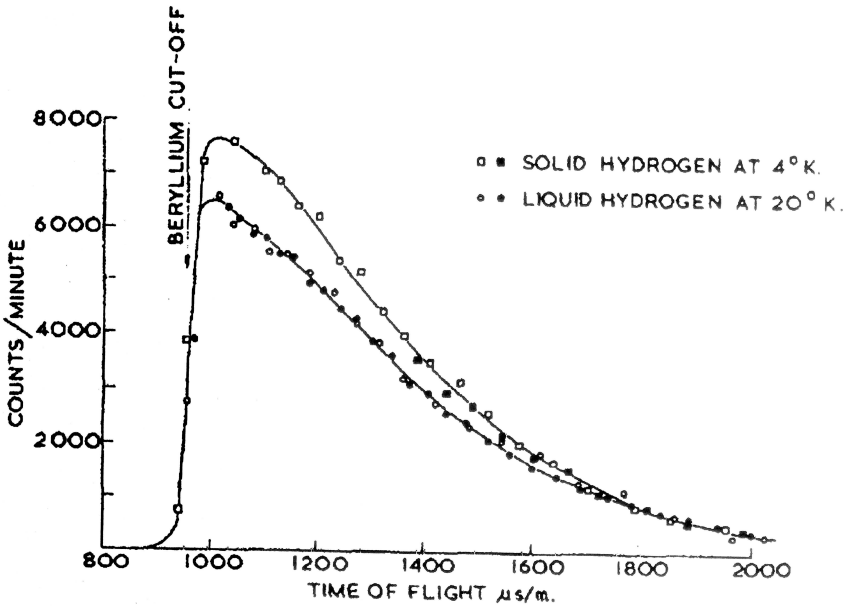

Figure 5.3: Liquid para-hydrogen and solid para-hydrogen time-of-flight spectra measured by Webb et.al. at the BEPO reactor in Harwell [58]. The white and black symbols correspond to two different sets of measurements.

used standard hydrogen with a purity of 5.0. Nevertheless, to clean the hydrogen gas from possible hydrocarbon contaminations, we installed a zeolithe trap in parallel to the oxysorb converter .
The conversion from natural to para hydrogen was done by the use of a new ortho/para converter system, Fig.5.4, filled with 50 g of oxysorb. To allow high mobility, the whole converter setup was installed vertically in a movable frame. With the help of a standard cryopump cold head from the former Leybold company, the converter vessel could be cooled down to 11 K. Finally, we managed to enrich para hydrogen concentration up to 90%.

ortho/para conversion

During a first test of the setup, only 15 K were reached inside the ortho/para converter volume. A solidification of hydrogen (triple point 13.8 K) inside the converter and therefore a sufficiently fast cryopumping speed was not possible. In order to continue the beamtime, the hydrogen was pumped in small quantities at a temperature of 15 K inside the converter. The high natural conversion of hydrogen and the additional paramagnetic catalyst (Oxysorb®) enriched the para concentration during one hour of pumping to a para concentration of 90%, Fig.5.5, which is a factor of 34 higher than the natural conversion speed.

A further decrease in conversion time may be achieved by the boiling methode, proposed in [36] and used already for the para ortho conversion of deuterium.

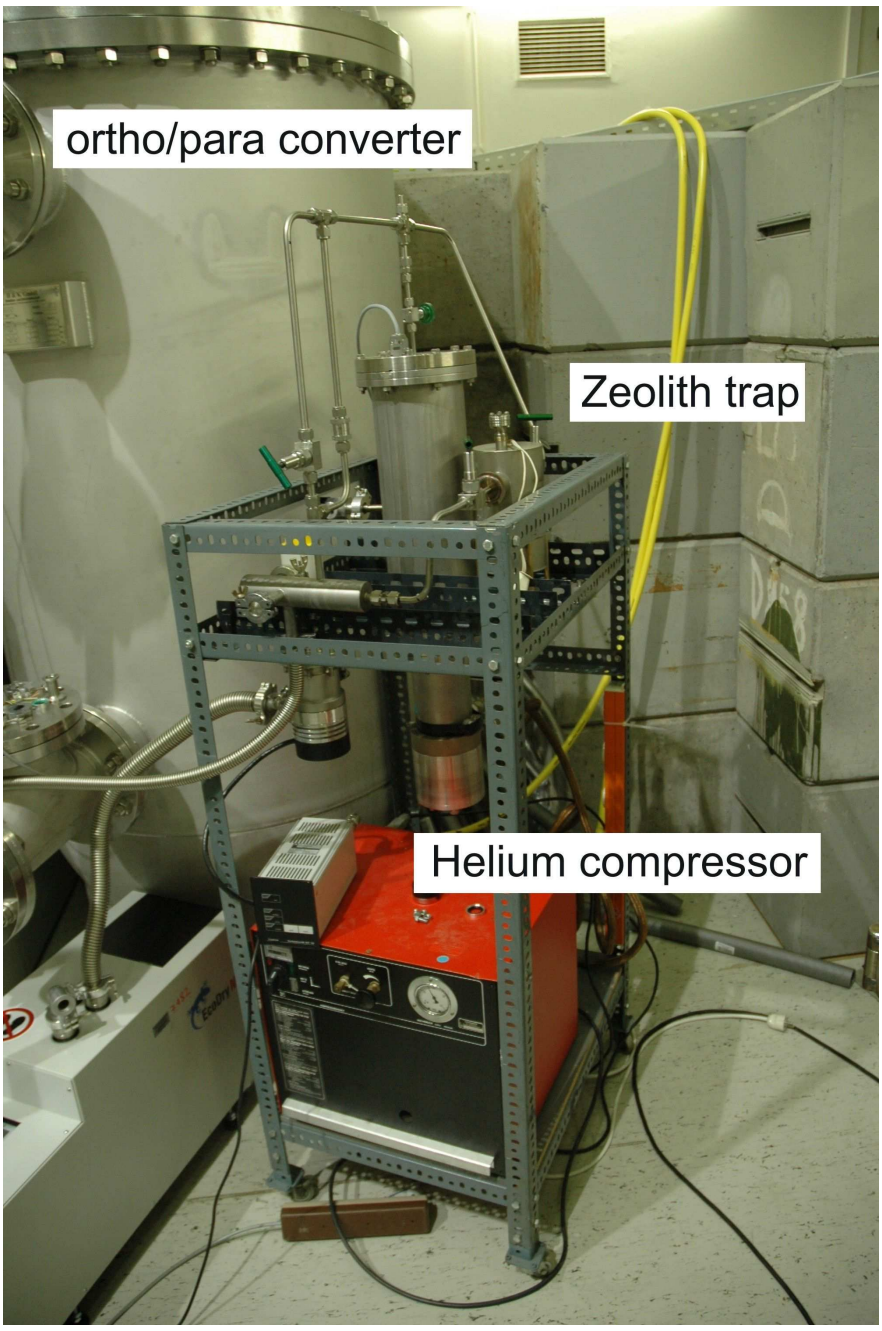

Figure 5.4: Hydrogen converter system including a vertical temperature controlled converter volume and a zeolithe trap

UCN output as function of the amount for natural hydrogen

In contrast to solid deuterium, one expects for hydrogen, because of the higher absorption cross section, a much shorter mean free path of $\approx$ 1mm. Therefore, investigations of the UCN yield as a function of the solid hydrogen quantity were done in smaller

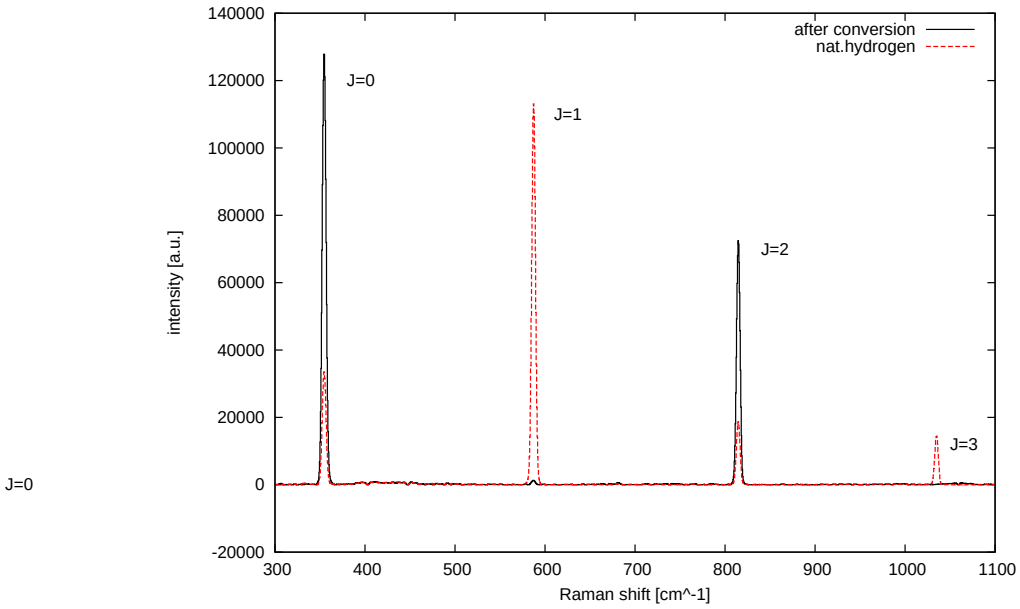

Figure 5.5: Background corrected Raman spectra of natural (red curve) and enriched para hydrogen (black). The conversion speed was 34 times higher than the natural conversion. The decrease of the J = 1 is quite significant.

steps than 1 mol. TOF spectra were taken for natural and 90% enriched para hydrogen with the standard setup already used for solid deuterium. As flight path for the TOF setup, we used a standard nocado guide with a length of 1.5 m. Unlike solid deuterium, the thermal conductivity of solid hydrogen is almost a factor of 10 higher ($\approx 1.5\ W \cdot cm^{-1} \cdot K^{-1}$ for pure para)[59]. Hence freezing of solid hydrogen at a speed of 1 slm resulted in our experiments in not detectable pressure inside the neutron guide. During the measurements the temperature of the converter was kept all the time constant at 7.5 K.

Each spectrum was accumulated within a measurement time of one hour. Supprisingly, the countrate for natural hydrogen was around 10 cts/s and increased with 90% para hydrogen at an amount of 2 mol to 33 cts/s. In contrast to solid deuterium, the maximal intensities in both spectra shifted to higher velocities around 8 m/s. This can be explained by the expected much smaller mean free path inside the solid hydrogen.

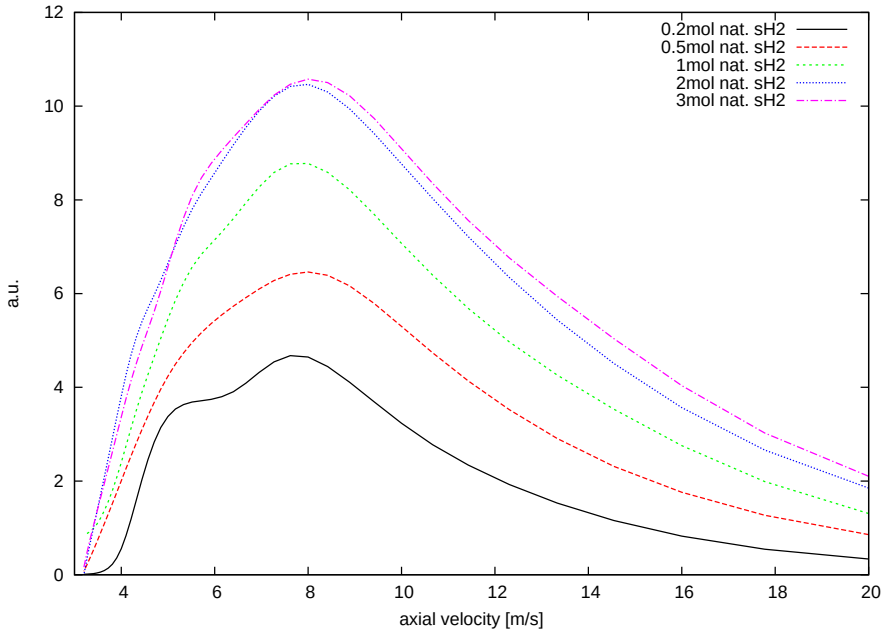

Figure 5.6: Deconvoluted spectra for different amounts of solid natural hydrogen.

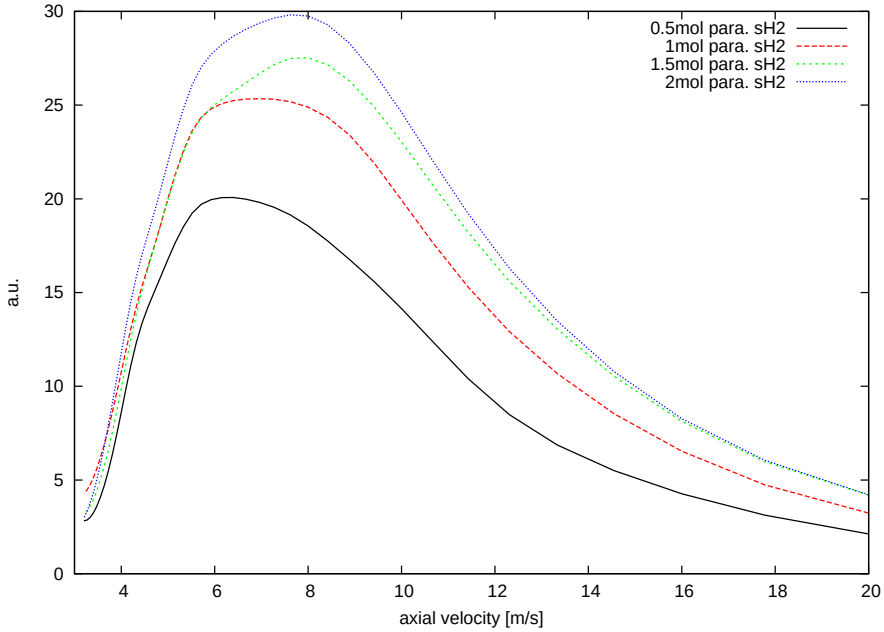

Figure 5.7: Deconvoluted spectra for different amounts of solid para hydrogen. Para concentration was 90%

5.3 Zero phonon upscattering on ortho hydrogen

By integrating the obtained spectra for the interesting velocity regions, we obtain the already known neutron yield as a function of amount of frozen hydrogen. Looking

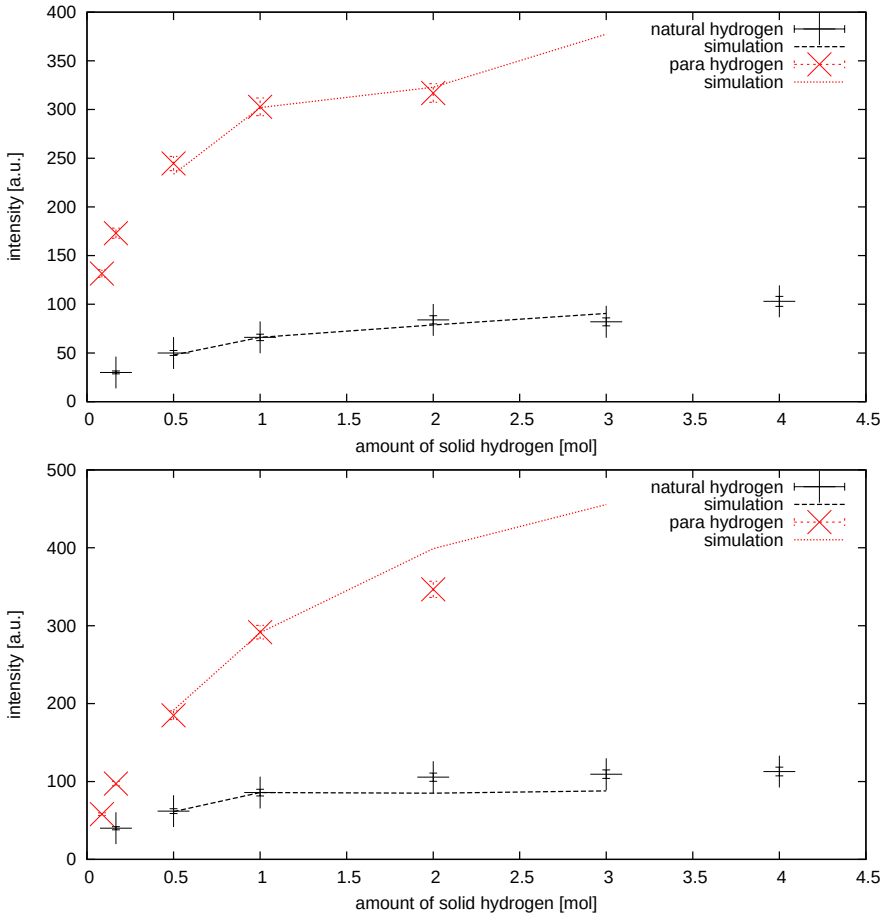

Figure 5.8: Upper Plot: UCN output for nat. and para hydrogen as a function of frozen amount. Lower plot: VCN output for nat. and para hydrogen as a function of frozen amount.

on both plots in Fig.5.8, the almost 4 times higher neutron output of para hydrogen obtained, is quite significant. Using only the known hydrogen parameters, it is simply not possible to explain this gain factor.

Table 5.1: Initial hydrogen parameters, used for the simulation of the UCN ($v \leq 6m/s$) and VCN ($v \geq 6m/s$) yield of a solid hydrogen converter

parameter	value
molecular number density	$\approx 2.63 \cdot 10^{23}$ /cm^3
σ_a	0.3325 barn
σ_{inc}	79.6 barn

According to the zero phonon calculations of para deuterium given in [29], it was possible to derive also in case of hydrogen with the known thermal incoherent scattering cross section of 80 barn and the conversion energy of 14.7 meV, a temperature independent upscattering cross section for pure ortho hydrogen of 3306 barns (v = 3 m/s). This UCN loss channel for natural hydrogen is almost one order of magnitude higher than the capture cross section.

Comparing the Monte Carlo results, see Fig.5.8 including this upscattering cross section, one obtains a gain factor of 4 for an enrichement of para concentration up to 90%, which is in good agreement with the measured data.

5.4 Hydrogen vs. deuterium

With respect to [26], we are able to compare the neutron outputs of a solid deuterium and a solid hydrogen converter. The data are shown in Fig.5.9

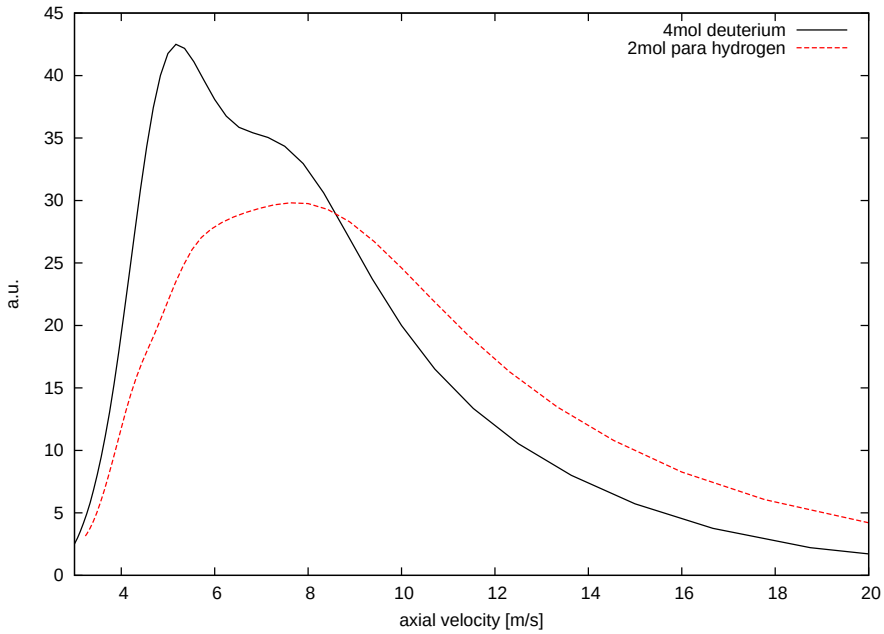

Figure 5.9: Comparison of TOF spectra measured with a UCN converter of 4 mol solid deuterium and with 2 mol of 90% para hydrogen. Both converters were prepared with the same freezing speed of 1 slm.

Unexpectedly, we found that the UCN and VCN neutron yield from the para hydrogen can be made comparable with solid deuterium at similar conditions. The only difference can be found in the velocity distribution of para hydrogen, which is shifted to higher velocities.
These results can open a new way, to use para hydrogen as converters for UCN sources at high flux reactors. The advantages of such a converter can be summarized:

- Thin layers of hydrogen giving approximately the same UCN yield as thick deuterium crystals
- Thermal conductivity of solid para hydrogen is much better than that of deuterium [59]
- Hydrogen can serve as effective premoderator as well
- Hydrogen has much higher ortho-para conversion speed

From our observations, it becomes obvious that UCN sources based on solid para hydrogen can be much easier realised at a high flux reactor than UCN sources based on solid deuterium. Taking into account the velocity shift of the shown TOF measurements, one has to mention that the installation of a UCN source based on solid para hydrogen in an inclined channel is preferable.

Chapter 6

Design of an upgraded UCN source for beamport D

The tangential beamport C of the reactor TRIGA Mainz was a unique test environment, which allowed us to study the physics and the handling of a solid deuterium UCN source at a real reactor environment. Based on the obtained experiences, the second topic of this thesis includes the design and installation of a new superthermal UCN source for the reactor TRIGA Mainz, which will operate at the radial beamport D. In future, UCN densities in the range of 30-40 UCN/cm^3 should be available for users at the experimental area.
Main tasks for the inpile cryostat design at beamport D are:

- 4 times higher thermal neutron flux → faster and higher activation of the main source components
- nuclear heating of the solid deuterium is 80 times higher than in beamport C due to fast neutrons
- the new system should work without liquid nitrogen
- an improved stability of the deuterium temperature is needed
- a significantly lower helium consumption is demanded
- installation of a premoderator is a prerequisite

6.1 The new inpile cryostat for "UCN D"

As already shown in Fig.2.8, beamport D is the only channel of the TRIGA Mark II which crosses the graphite reflector ring and ends close to the reactor core. Due to this fact the thermal neutron flux is about a factor of four higher than in beamport C, Fig.2.11 , that should result correspondingly to an increase by the same amount in obtainable ultracold neutron density.

However, besides this attractive feature, the radial channel has also an essential drawback, e.g., the higher flux of fast neutrons and gammas which results both in an increase of heatload and in higher activation of the source components.
To overcome or at least to minimize these problems coupled with proximity to the reactor core, special care was taken for the design of the converter cup and all parts up to a distance of 500mm behind it. In the following section, all substantial parts of the new inpile cryostat will be described in more detail.

6.1.1 UCN guide and converter system

In order to reduce the neutron activation and to improve the thermal conductivity of the whole converter cup, the standard reactor alloy AlMgSi (Al6061) as material for the "nose" part of neutron guide is selected. Unfortunately, like beamport C, the inner diameter of the beamtube of 150mm reduces quite severely the available space for the final converter setup. To increase the available space, we omitted the use of a three barrier system like at the prototype source. To ensure all safety requirements, the thickness of the vacuum tube was increased and should now act also as safety barrier against explosions. This way it was possible to achieve an maximal usable internal diameter of 130 mm for the final converter and guide installations.
As can be seen in Fig.6.1, the simple cylindrical design of the final converter cup includes three aluminium cylinders with a maximal wall thickness of 1mm, which are welded together at 2 radial positions. The inner cup, the UCN converter volume, has the standard neutron guide internal diameter of 66mm and can keep with the internal length of 100 mm maximal 340 cm^3 (14.5 mol) of solid deuterium. The active cooling surface of $\approx$ 250 cm^2 is surrounded by a layer of supercritical helium which is kept in a gap of 1.5 mm by a second aluminium cylinder. Finally a premoderator cyclinder builds the third wall around the deuterium and helium part. The maximum usable premoderator volume is 540 cm^3 which results in maximum of 40 mol of solid hydrogen or 17 mol of solid methane.

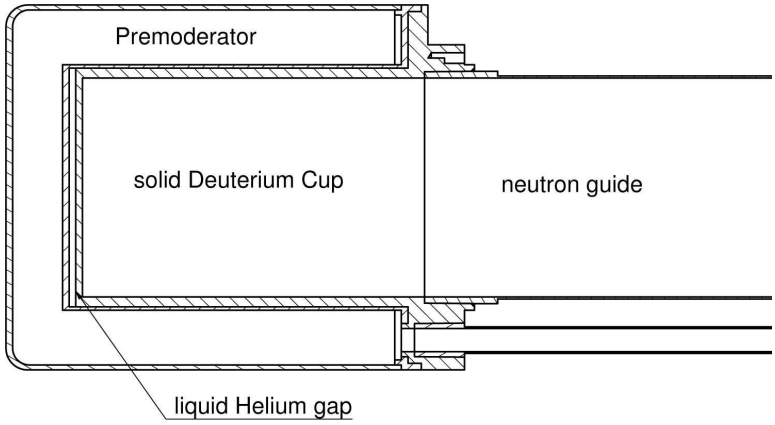

Figure 6.1: Cylindrical design of the converter cup for the UCN source at the radial channel D of the Triga reactor in Mainz.

To overcome the low Fermi potential of alumnium (54neV), which would result in ob-

vious UCN losses, the assembled and electropolished converter cup was coated inside with a non magnetic alloy of NiMo (90/10). To ensure good adhesion of the coatings we made use of the sputtering technique which is also used for the production of UCN guides [60].
The high thermal conductivity of the used aluminium alloy ensures an optimal heat removal from the converter and the premoderator volume, but as already realized in the first version of a prototype source for beamport C [61] it cannot be used as substrate material for adjoint neutron guide to extract UCN. Using aluminium as UCN guide material would result in a cooling down of the whole guide, especially in that part close to the converter (below 20 K). This cold part would then act as cryopump and freeze out the rest gas (mainly hydrogen and nitrogen) on the surface of neutron guide which would produce UCN losses due to absorption.
To solve this problem the aluminium guide of the first prototype version was exchanged against an electropolished high grade stainless steel tube, which is used in pharmaceutical industry and was found to be also a good guide for ultracold neutrons [62].
The thermal conductivity of stainless steel is much weaker than that of aluminium. By reducing the standard tube thickness from 2 mm to 0.6 mm on a length of 400mm behind the converter cup, it was possible to keep the adjacent neutron guide at room temperature which was essential for the final success in extraction of UCN at beamport C.
According to our experiences with UCN at C, stainless steel as material for neutron guide is a reliable choice, also for the new UCN source at beamport D. Unfortunately, one can find only two acceptable variants for the connection between the aluminium "nose" and the adjacent stainless steel at very low temperatures and under radiation conditions: a flange connection with metallic sealing, or an explosion bonded transition with intermediate materials like Cu and Ti. Due to the lack of space inside the inpile tube, any flange connection was practically impossible. Also the sizes and thicknesses of commercially available explosion bonded transitions were to large for our purpose.

A home made aluminium stainless steel transition

In order to solve the problem, we started to investigate friction welding and shrinking techniques. After several attempts in testing the shrinking technique, where a stainless steel is pressed into a aluminium tube, we found the following solution shown in Fig.6.2. To ensure a stable and vacuum tight connection, the intermediate surface is machined slightly conical. After cooling down the stainless steel part to liquid nitrogen temperature and simultaneously heating the aluminium up to 200°C, the stainless steel cone can be placed without force inside the aluminium tube. The force due to shrinking of the aluminium during cooling down was sufficient for a good sealing. To prevent the intermediate connection from ageing due to the different electronegativities of the connected parts and for improvement of sealing, the stainless steel was coated additionally by electrodeposition with a 20 μm Cu layer which acts as safety barrier.

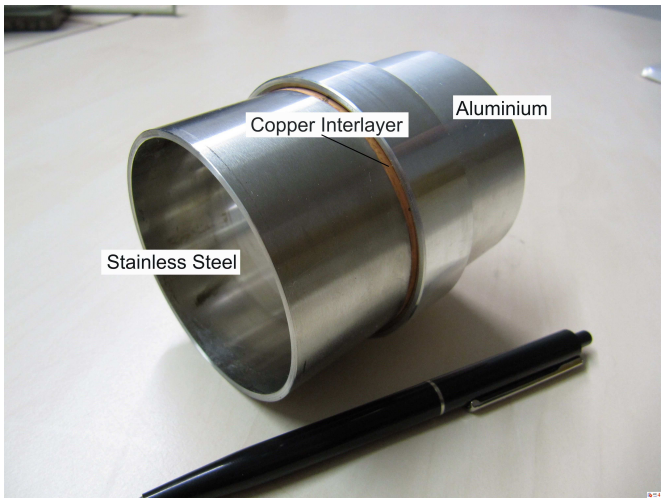

Figure 6.2: Picture of a 70mm test transition. The visible copper will be covered in a second step by low temperature epoxy in order to prevent the copper from oxidation.

6.1.2 Design of the cryogenique system

Main goal of the design of a new cryogenic system for the new UCN source at beamport D was the reduction of the huge helium consumption actually needed at the current UCN source at beamport C. In future, it should be possible to work with the already mentioned 1500 l helium dewar for more than three weeks without melting of the crystal. This goal corresponds to a helium consumption of $\approx$ 3 l/h.

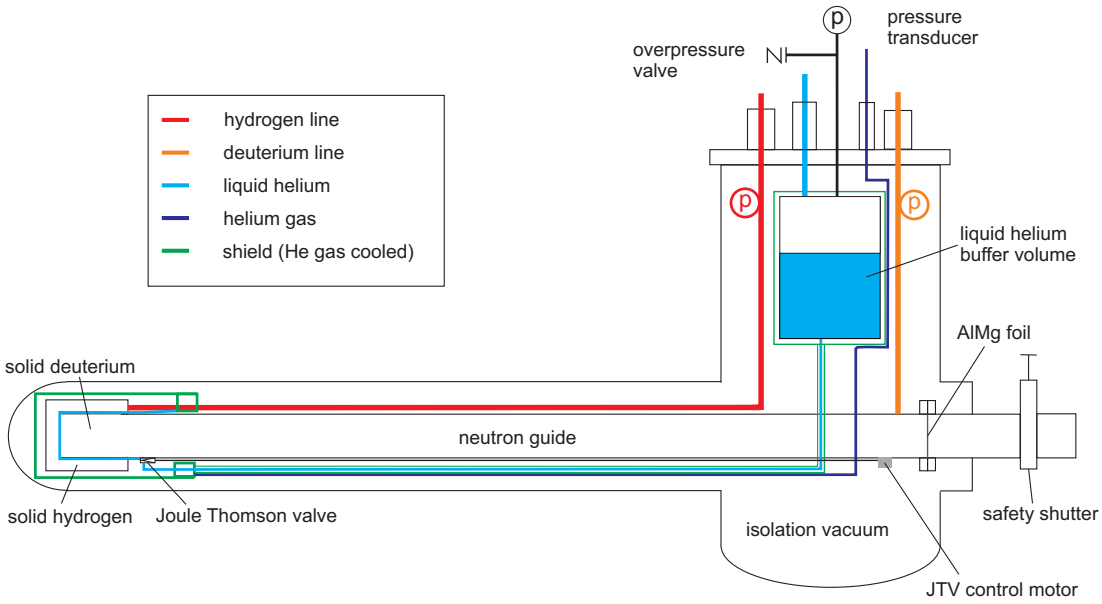

Figure 6.3: Scheme of the cryogenic system of the new inpile part for beamtube D.

To reach this goal, a completly new design of the cryogenic system was needed, which resulted in:

1. a reduction of the inner diameter of the helium supply lines to the converter cup.

2. an installation of a Joule-Thomson expansion valve close to the converter cup to control the helium flow.

3. a liquid helium buffer volume in the cryostat vacuum vessel outside the reactor.

4. an efficiently cooled shielding for the liquid helium line between buffer and the converter cup.

helium supply lines

Instead of the old 10mm diameter helium supply lines, the inlet line of the new system has a internal diameter of only 3 mm. To reduce the mass of the stainless steel tubes and therefore the heatload, only capillar tubes with a wall thickness of 0.4 mm were used.

Joule-Thomson valve

According to the standard liquefier technique, a Joule-Thomson valve was designed and soldered directly to the helium input of the converter cup. Using this standard helium evaporizer cryostat scheme [63], temperature regulations in the region of the desired 5 K should be possible with an accuracy better than 0.1 K. By applying a special pump system on the helium outlet line, the temperature stability can be improved even more. Futhermore, a decrease in the helium consumption due to a better heat exchange between the converter and the obtained supercritical helium He-II phase can be expected.
Fig.6.4 shows the design of the installed needle valve. Besides the needle, which is machined from a special aluminium bronze compound, the whole valve is built from stainless steel. To reduce the number of neutron activated parts and also for an easier maintainance access, the control actuator of the valve is installed in the cryostat vacuum vessel outside of the reactor just under the helium buffer volume. With the coupling via a tube system and a highly flexible bellow, the needle position can be regulated by a stepping motor from nanotec company with a resolution of 10 μm.

A liquid helium buffer volume

Starting from the first ideas of a running UCN source at beamport D, a liquid helium storage volume inside the inpile cryostat was one of the key features, which was needed, to exchange the small 250 l dewars without melting of the deuterium crystal.
Therefore a 10 l stainless steel volume, Fig.6.5, was designed which should keep enough helium for the safety handling of the deuterium for a minimum two hours.

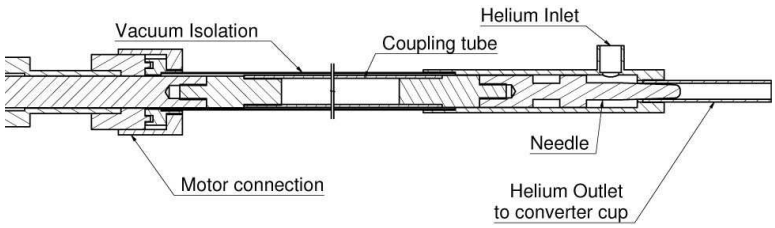

Figure 6.4: Scheme of the Joule Thomson valve (JVT) which is soldered to the helium input of the converter cup.

New shield concept for all 4K parts

Without any appropriate thermal shielding it is almost impossible to reach liquid helium temperatures in any cryostat system without considerable helium consumption. Hence, to save the liquid helium from the thermal radiation heatload of surrounding warm source parts, a new concept was developed, where the shield is no longer cooled with liquid nitrogen (old system) instead the outgoing evaporated helium gas, which has still a temperature of ≈ 30 K. Via a thermal bridge (stainless steel capillary tube) the helium gas from the converter is first flowing through an aluminium shield holder, which cooles this way the alumnium shield of the converter cup with a diameter of 120 mm. The necessary aluminium stainless steel transitions were also home made. A three meter long capillary tube with an internal diameter of 4mm, soldered to a 12 mm diameter tube which acts as shielding of the liquid helium inlet line, transfers the helium gas to the last heat exchanger coil at the buffer volume shield. The shield of the buffer volume can be separately cooled down by a second heat exchanger coil which is connected via a low temperature helium valve to the buffer volume.

6.2 First cooling down of the system

The first cooling down of the setup was done in August 2009. Because of some delays in ordering of the stepping motor for the control of the needle valve, we had to drive the system with a completely open liquid helium inlet line which should result in a higher consumption. The helium was transferred via a static transfer line from a standard 250 l dewar into the buffer volume. Starting with a vacuum of $\approx 10^{-4}$ mbar (after 12hours of pumping) and keeping the cold gas valve for the pressure regulation of the buffer closed, we had been able to cool down the converter cup to a temperature of 8 K in 30 min. Unfortunately a further decrease of temperature was not possible due to the bad vacuum conditions and the related high temperature of ≈ 100 K at the converter shield.

Test of buffer volume

During the flow through mode, it was not possible to detect any liquid helium level inside the buffer volume. To test also the buffer volume and its functionality, the pressure and therefore the helium flow through the cryostat had to be reduced. After reaching a

shield temperature of 100K and opening the cold gas valve to the heat exchanger coil, we had been able to fill the whole buffer volume $\approx$ 12 l within a time of 8 min. By closing the gas valve a further decrease of the converter cup especially at the helium inlet line could be investigated. Without any regulation of the helium inlet the buffer volume was emptied in $\approx$ 4 min.

Figure 6.5: Picture of the helium buffer volume which is already connected to the top flange of the support volume outside the reactor. The two swagelok lines in front are the D_2 and premoderator connections to the neutron guide and the premoderator transfer tube.

Figure 6.6: Picture of the nose during the final soldering of the cryogenic transfer lines. The 70 mm aluminium stainless steel transistion can be recognized on the glossy copper coating. All the other transitions are hidden by low temperature stycast (black), in order to avoid oxidation of the copper in air.

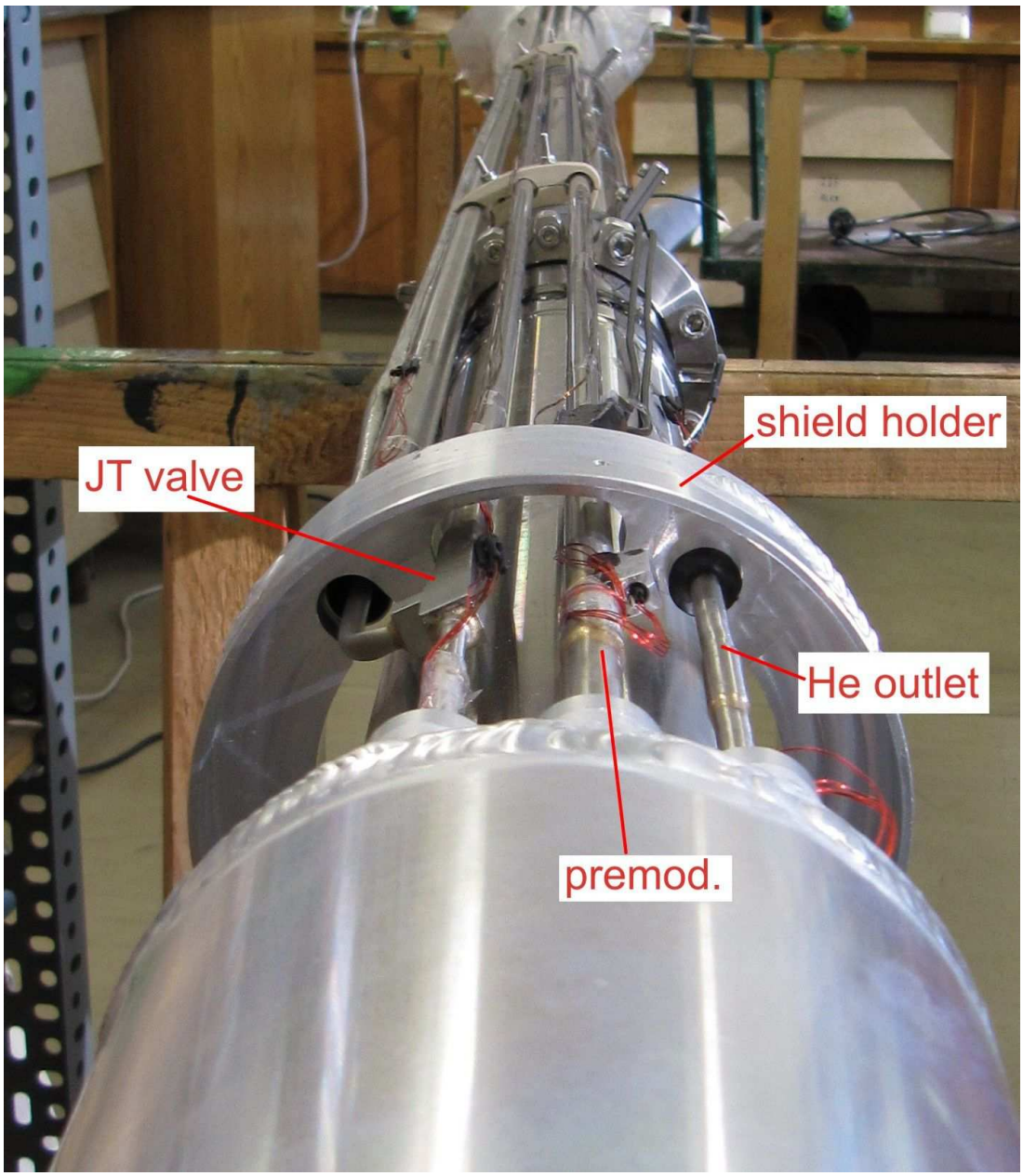

Figure 6.7: Picture of the finally assembled neutron guide. All helium lines including the Joule Thomson valve (JT valve) are visible. The premoderator vessel is connected with a 8 mm stainless steel tube which can be heated by means of a thermo coax line. The red wires in the picture are electronic connections of the cernox temperature sensors.

Conclusions

The results of the first test can be summarized in a few points

1. With the existing cryogenic setup, it is possible to reach the expected temperatures for freezing a solid deuterium crystal
2. Keeping liquid helium inside the buffer volume is possible
3. Without the installed Joule Thomson valve we reached a helium consumption of ≈ 8 l/h in flow through mode
4. An improved vacuum will further decrease the temperature of the shield

6.3 Predictions based on MCNP and latest results

Because of the not yet completed comissioning of the cryostat, only some predictions on the UCN output and the final UCN density obtainable at the experimental area of the new UCN source at beamport D can be given. According to the existing MCNP model of the reactor including channel D, see also appenidx D, Fig.D.1, it was possible to give some first estimation of the thermal neutron fluxes, the final UCN production, and the fast neutron and gamma heatload acting from the reactor on the installed components.

Heatload calculations

Based on *MCNP* the nuclear heating (mainly due to fast neutrons with energies around 1 MeV) of the solid deuterium would result without any premoderator in:

$$P_{n+\gamma} = 40 \ \frac{mW}{g \cdot 100kW} \tag{6.1}$$

For a typical 1.5$ pulse this power would result in an energy release inside the deuterium of:

$$E_{n+\gamma} = 2.5 \ \frac{J}{g} \tag{6.2}$$

Assuming a fast energy release in 75 ms and a low thermal conductivity of the deuterium, it is possible to estimate in a first approxiamtion using only the heat capacity for solid deuterium of ≈ 155 mJ/g (at 5 K) a temperature increase of 16 K. Without a sufficient high thermal conductivity, which is especially the case for not well prepared crystals, such a temperature rise would therefore lead immediatly to not controlable sudden evaporations of deuterium at its inner surface.
To avoid this situation the converter has to be shielded from the 10 times higher fast neutron flux.

Typical reflector materials are either beryllium or graphite. To optimize the reflector insert, we performed several *MCNP* calculations with varying the insert length. Finally

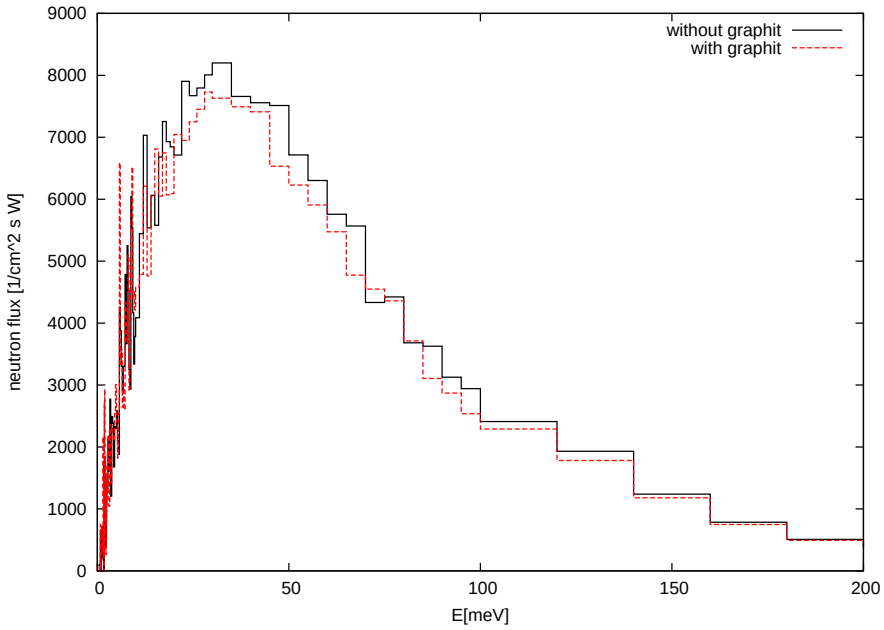

Figure 6.8: MCNP result for the thermal neutron spectra with and without a graphite shielding.

we found that a graphite cylinder in front of the inpile tube, see also Fig.D.1 with a length of 120 mm would reduce the initial neutron heatload by about a factor of 5, with a reduction of the thermal neutron flux of 5.5% , see also Fig.6.8

The final heatload with a 120 mm grapithe cylinder in front of the inpile tube will be

$$P_{n+\gamma} = 9 \ \frac{mW}{g \cdot 100kW} \tag{6.3}$$

corresponding to an energy realease during a 1.5$ pulse of

$$E_{n+\gamma} = 0.55 \ \frac{J}{g} \tag{6.4}$$

and a temperature increase of 3.5 K. Keeping the crystal at a constant temperature would result in a sudden temperature of around 9 K. An evaporation of the deuterium, therefore, is impossible. Damages due to cracks are not excepted up to now.

The right premoderator

To achieve an optimal UCN production inside the solid deuterium, the initial thermal neutron spectrum has to be cooled down to the range of 30 K, see also Fig.2.4.
In contrast to the tested liquid organic premoderators which didn't show the expected gain factors, the new setup is prepared for a premoderator which can be frozen like the deuterium converter directly from the gas phase.
Due to their thermal neutron cross sections, hydrogen and methane are standard substances used in cold neutron source designs and are therefore interesting materials for

our premoderator choice.

Liquid Hydrogen

Nowadays many research reactors are equipped with cold neutron sources, based on either H_2 or D_2 or mixtures of both . Deuterium has the advantage of a good scattering quality combined with low absorption. But because of the mean free path of the neutrons of $>$ 100 mm in D_2, larger moderator volumes in comparison with hydrogen ($<$ 20mm) are needed.
Nevertheless, the absorption cross section of hydrogen is by more than a factor of 600 higher.

The use of hydrogen as premoderator demands one remark: the ortho-para conversion. As mentioned in Chap.5, hydrogen at room temperature contains 25% of H_2 molecules in para state. Liquifying or even solidifying normal hydrogen at lower temperatures will automatically cause a change of the equilibrium to higher concentrations of para H_2. At 10 K almost 99.9% of the molecules are para-hydrogen.
As can be seen in Fig.6.9, for neutron energies smaller than 100 meV the mean neutron scattering cross-section strongly depends on the ratio of ortho and para H_2.

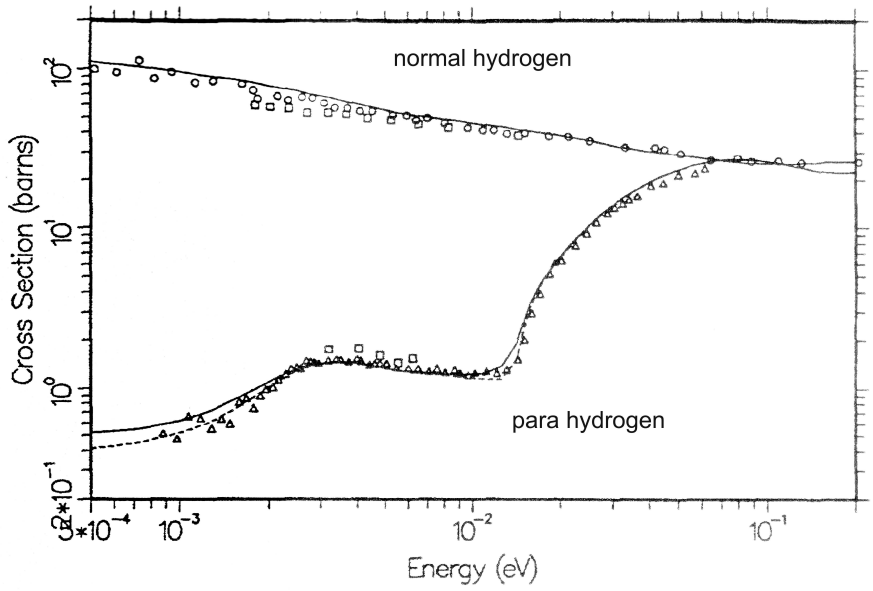

Figure 6.9: The cross sections for liquid ortho hydrogen(upper curve) and liquid para hydrogen (lower curve) are compared with experimental dat due to Squires (gas) at 20K (squares), Whittermore at 20K (circles), and Seiffert at 14K (triangles). The solid curves are at 20K, and the dashed curve is at 14K. The sharp drop in the para cross section below 50 meV is due to spin coherence, and the second drop below 3 meV is due to intermolecular interference. The plot is taken from [64].

Due to the fast ortho/para conversion of hydrogen at low temperatures [57], we expect

a change of the moderation properties within the first two days of source operation. Driving the future source at beamport D with a hydrogen premoderator at stable cold neutron flux conditions, would therefore demand an ortho/para conversion of the used hydrogen before the freezing operation.
To study the moderation characteristics, the existing MCNP model was extended by a realistic cylindrical premoderator volume, see also Fig.D.1, with an maximal moderator layer thickness of 15mm. The cross sections for pure para and also natural liquid hydrogen were taken from the standard *MCNP* library.

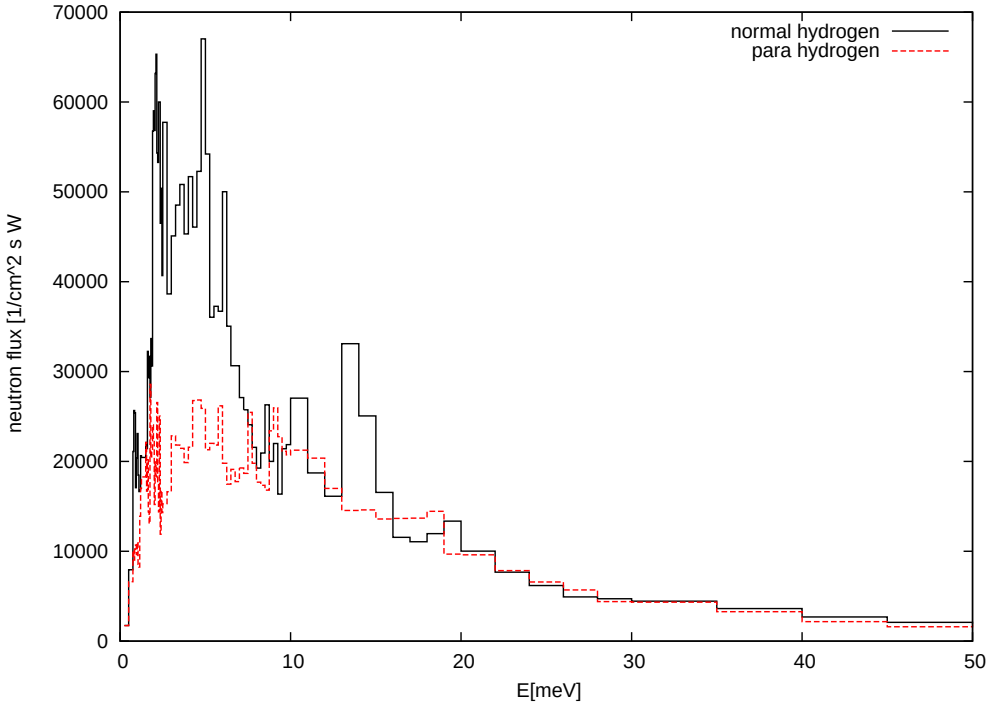

Figure 6.10: Neutron energy spectra obtained from *MCNP* simulations. Black curve: 15 mm natural hydrogen as premoderator layer. Red curve: 15 mm para hydrogen as premoderator layer. In order to obtain the neutron spectum of the premoderator, the simulation was performed without any deuterium converter inside the convertercup.

Unfortunately the thermal cross section for para hydrogen is 5-10 times less than for natural hydrogen, which corresponds to a reduction of almost 60% in cold neutron flux. A fit on the spectra presented in Fig.6.10 with the sum of two maxwell function gives for para hydrogen two characteristic neutron temperatures $T_1 = 23$ K and $T_2 = 90$K. For normal hydrogen we obtain from the fit $T_1 = 36$ K and $T_2 = 191$K.

Solid methane

Solid methane moderators are in operation at Argonne National Laboratory (IPNS-facility, USA) at the Neutron Science Laboratory KENS (KEK-facility, Japan) , and at the pulsed reactor IBR-2 (Joint Institute for Nuclear Research in Dubna, Russia).

One big advantage of methane over hydrogen can be found in its almost two times higher hydrogen atom density ($\approx 8 \cdot 10^{22}/cm^3$ [65]). This number is of great importance for the slowing down of fast-neutron in a narrow region. Additionally, by the rotational excitations with energy levels

$$E_J = 1.30J(J+1)/2\ meV(J = 1, 2, 3, ...) \tag{6.5}$$

downscattering of thermal neutrons to a cold ones takes place.
Fig.6.11 presents the results of two total neutron cross section calculations for solid methane II (solid methane at a temperature $\leq$ 20.4K) at two different temperatures which are published in [67].

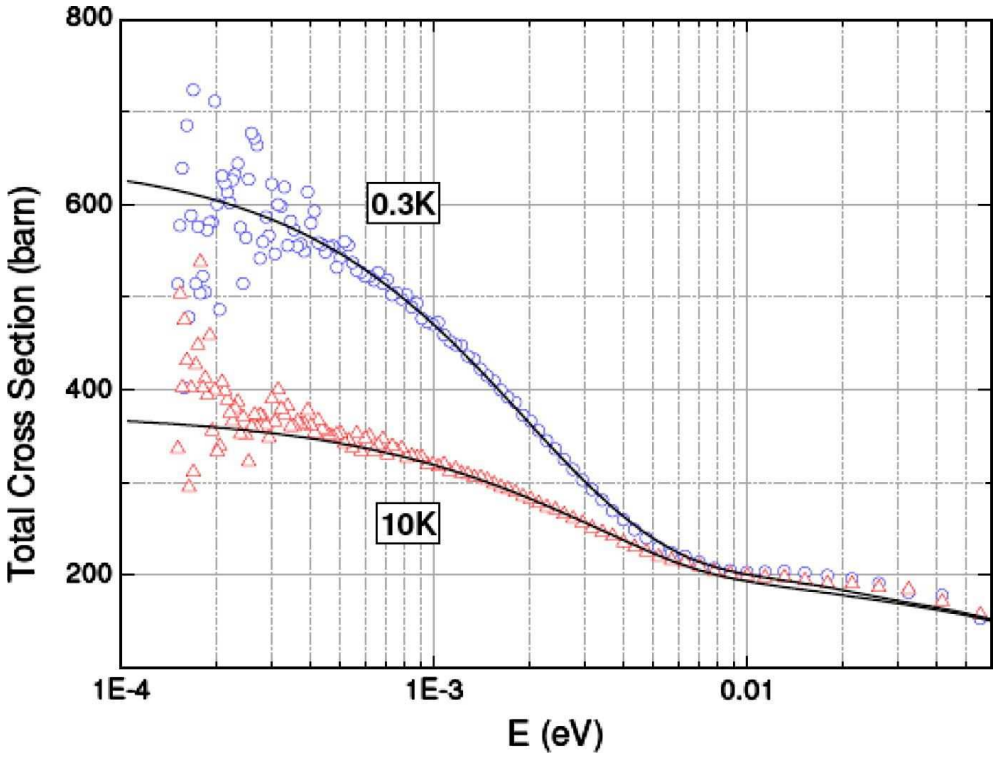

Figure 6.11: Comparison of the calculated total cross sections of methane at 0.3 K and 10 K, with the measured points of [66]. Plot was taken from [67]

In comparison to para hydrogen, the scattering cross section increases below 100 meV increases by almost a factor of 4 with decreasing neutron energy. Therefor, we expect a much higher UCN output from a UCN converter combined with a solid methane premoderator.

As for hydrogen, a *MCNP* simulation based on the existing reactor model including a premoderator layer of 15 mm thickness was performed. The neutron cross section was again taken from the *MCNP* library which unfortunately contained only the cross section for solid methane I.

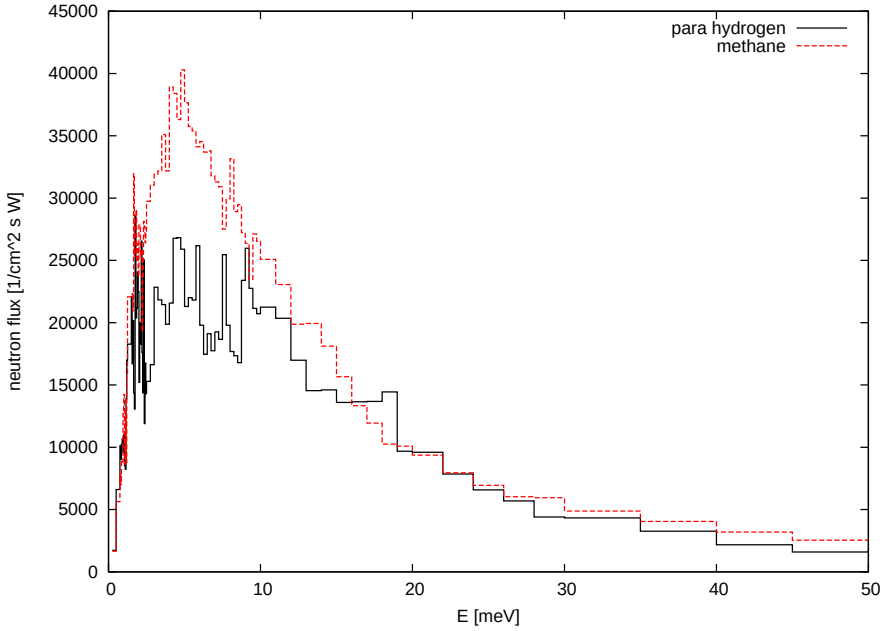

Figure 6.12: Neutron energy spectra at the position of the first layer of the solid deuterium converter. Black curve: Thermal neutron spectrum with 15 mm para hydrogen as premoderator. Red curve: 15 mm of solid methane as premoderator.

In contrast to the hydrogen premoderated spectra a single maxwell fit describes quite well the simulated results.From the fit we obtain for solid methane a neutron temperature of 59 K.

The clearly favourable neutronic properties of methane as a moderator, however, are faced with some disadvantages in its technical realization :

- Methane is radiolysed under irradiation (mainly fast neutrons) in the following reaction:

$$CH_4 + \Delta E \rightarrow H^* + C^*H_3 \tag{6.6}$$

  In liquid phase radiolysis plays a minor role. Recombination according to:

$$H^* + C^*H_3 \rightarrow H_2 + C^*H_2 \tag{6.7}$$

  leads to the production of hydrogen and hydrocarbonic "wax" -CH_2-.
  However, because of the low diffusion rate inside solid methane, radicals are stored without recombination. Experimentally it was found, that radical concentrations at a level of 6% lead to an explosion with a high energy release.

- The heat conductivity of solid methane is low ($<$ 4 mW / cm K below 32 K) . This leads to a temperature gradient in the solid methane. Therefore only thin layers should be used.

To estimate the production of radicals one can use the previously shown *MCNP* results including the radiation dose inside a 15mm layer of solid methane of

$$D_{n+\gamma} = 600\ Gray\ /2\$\ pulse \tag{6.8}$$

and a heatload of

$$P_{n+\gamma} = 10\ \frac{mW}{g \cdot 100kW} \tag{6.9}$$

According to [68], this radiation dose would lead to a radical formation of $\approx\ 2.4 \cdot 10^{17}$ radicals per 2\$ pulse. To accumulate the explosive concentration of 6% radicals, one needs therefore more than 10^5 pulses.
With this result, a safe operation of a solid methane premoderator at the beamport D can be guaranteed.

Possible UCN outputs at "UCN D" for different premoderator settings

The final decision on the later premoderator will certainly be defined with the help of experimental results. In order to obtain a first impression of the final UCN production at the new converter setup, it is nevertheless interesting to study a bit more in detail the free parameters (premoderator material and thickness) of "UCN D" with the help of *MCNP* simulations. To compare the results with the data obtained for beamport C, we assumed for beamport D an UCN converter with an amount of 7 mol deuterium. For every parameter setting (material and thickness of premoderator), the UCN production was calculated according to

$$P = P_{atom} \cdot N_{sD} = P_{atom} \cdot 2.63 \cdot 10^{22}\ /cm^3 s \tag{6.10}$$

For the total UCN production inside the whole crystal we have to multiply this number with the molar volume of solid deuterium of 20 cm^3/mol

$$P_{converter} = P \cdot 20\ cm^3/mol \tag{6.11}$$

In 10 different simulation runs, we obtained for the discussed moderator materials (nat. hydrogen, para hydrogen and solid methane I) surrounding the UCN converter as premoderator the UCN production as a function of premoderator thickness, Fig.6.13.

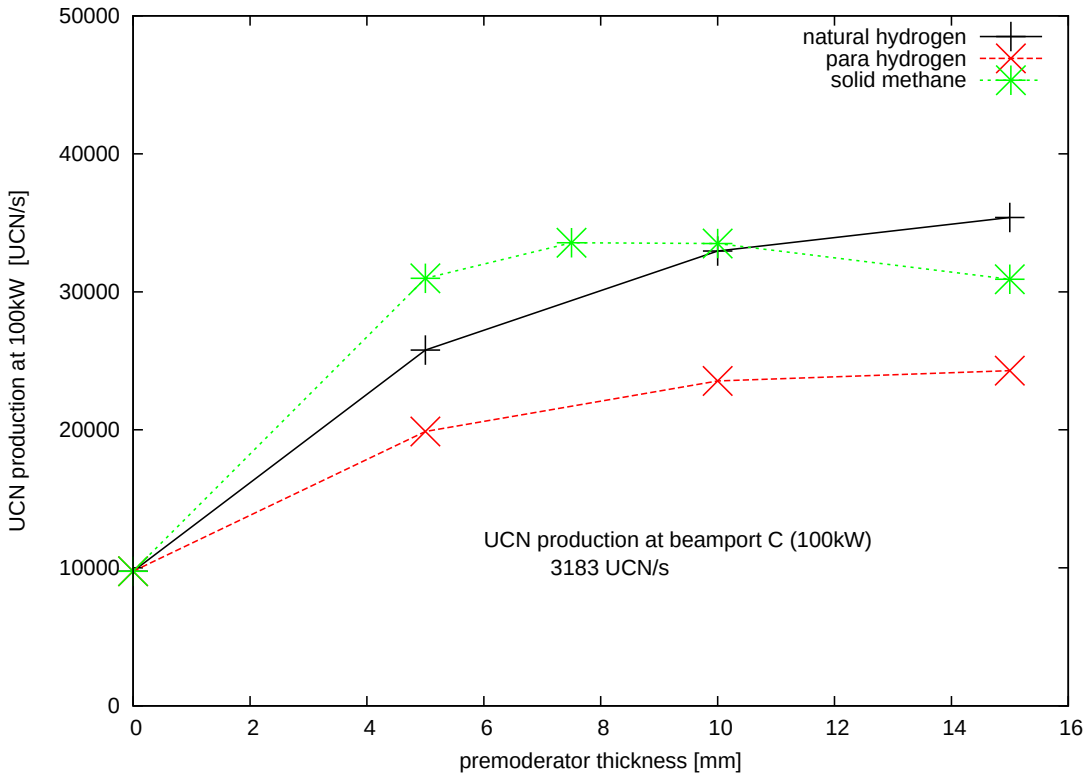

Figure 6.13: Calculated UCN production as a function of premmoderator thickness. Black curve: liquid natural hydrogen (16 K) as premoderator. Red curve: liquid para hydrogen (16 K) as premoderator. Green curve: solid methane (phase I) as premoderator.

Because of the not existing knowledge of the transmission function of the new setup, it is possible to give only a rough estimation of the final reachable UCN densities in a storage setup, see also chap.4.4.1.
Comparing the calculated production of C and D and the finally reached UCN density at "UCN C", one expects a minimal UCN density for a 15 mm thick layer of para hydrogen as premoderator of

$$\rho_{UCN} = 32\ /cm^3 \tag{6.12}$$

The use of a 7 mm layer of solid methane as premoderator can even increase this number by 40% to roughly

$$\rho_{UCN} = 44\ /cm^3 \tag{6.13}$$

Chapter 7

UCN instrumentation and developments

7.1 A fast shutter for UCN storage experiments

The typical time scale of UCN pulses (see also Fig.4.1) following an reactor pulse at the existing UCN source at the TRIGA Mainz is in the range of a few seconds. Compared to typical filling times (order of 10 seconds) in standard UCN storage experiments at the steady state UCN source at ILL (Grenoble), this is a rather short time. In order to reach an optimal UCN density inside a storage volume at a pulsed UCN source like the TRIGA Mainz, the closing time of a shutter is of great importance and should be in the range of one tenth of the filling time, see also Chap.4.4.1.
Thus, to realize a storage experiment at our pulsed UCN source, we designed and built two stand alone shutters (Fig.7.4).

7.1.1 The shutter design

The main requirements to any UCN shutter, used for storage experiments, is its almost diminishing probability of loosing neutrons in a possible gap between shutter lid and storage vessel. To reduce this gap in our setup, a meachnism was realized, which is pressing the lid to the entrance of the storage vessel. Instead of two different motions (closing the lid and pressing the lid), especially formed levers transform the vertical force of the closing lid into a horizontal one, just before the UCN entrance is completely closed, see also Fig.7.1.
A pressurized air driven piston, which is mounted outside the vacuum housing, garantees the needed force and speed for this action. To save money, a standard stainless steel bellow with a length of 70 mm was adjusted for our purpose and serves now as vacuum feedthrough for the linear piston motion.
All of the shutter parts are made out of stainless steel to ensure their mechanical strength and reliability. To decrease the friction of the lid during sliding inside its linear fixation, the lid was coated with 2 μm of diamond like carbon, DLC.

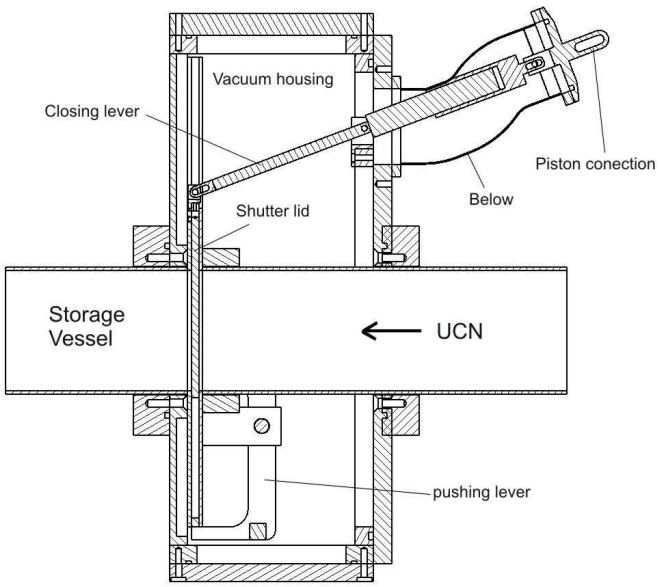

Figure 7.1: Sectional view of the shutter design.

To determine the opening and closing speed of the shutter, we performed a TOF measurement corresponding to appenidxB. In this setup, the shutter was installed with a horizontal 45 degree nocado bend and 1.5 m guide tube away from the beam axis. To obtain a "neutron picture" the used UCN detector was connected with a short flight path of 20 cm UCN guide to the shutter outlet (entrance to storage vessel).

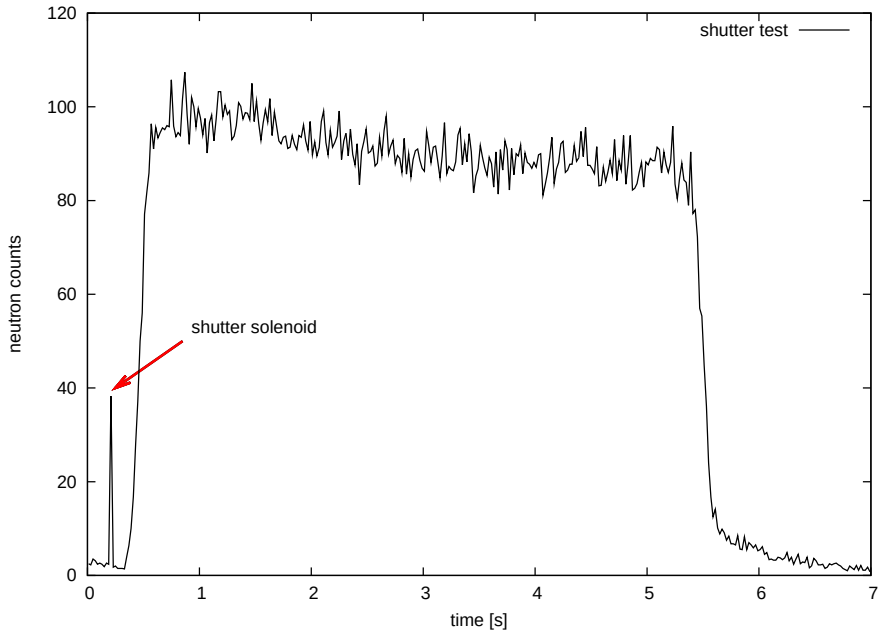

Figure 7.2: Measured opening function of the new shutter system. The spike at 0.2 s originates from electronic noise from a solenoid.

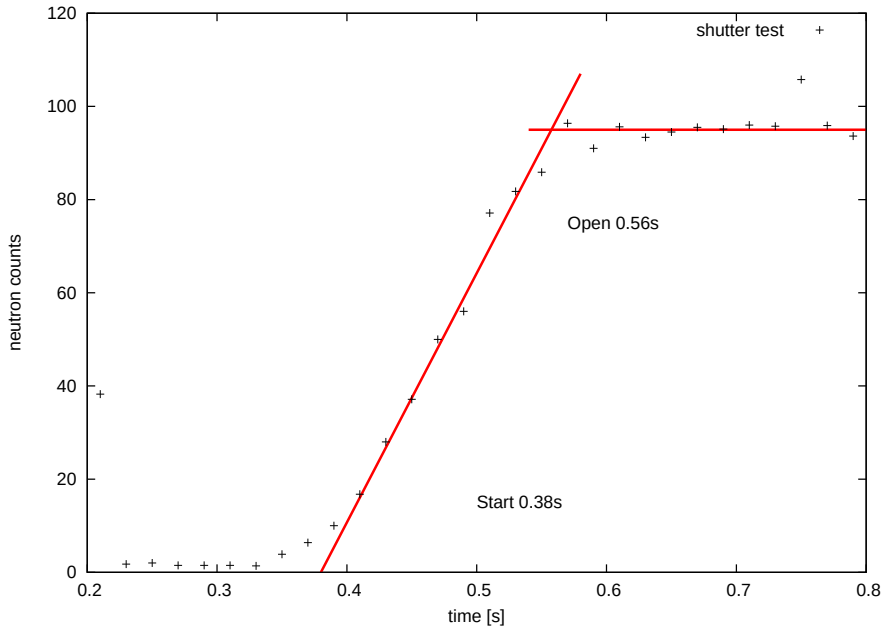

Figure 7.3: Zoomed region of the measured opening function, see also Fig.7.2. The red lines are used to determine approximately the opening time of the shutter system.

By fitting just by eyes two straight lines into the rising opening function (Fig.7.3 right side), one determines an opening time of 180 ms. The spike at 0.2 s in Fig.7.2 is a result of electronic noise from the used solenoids which drives as switch for the pressurized air.

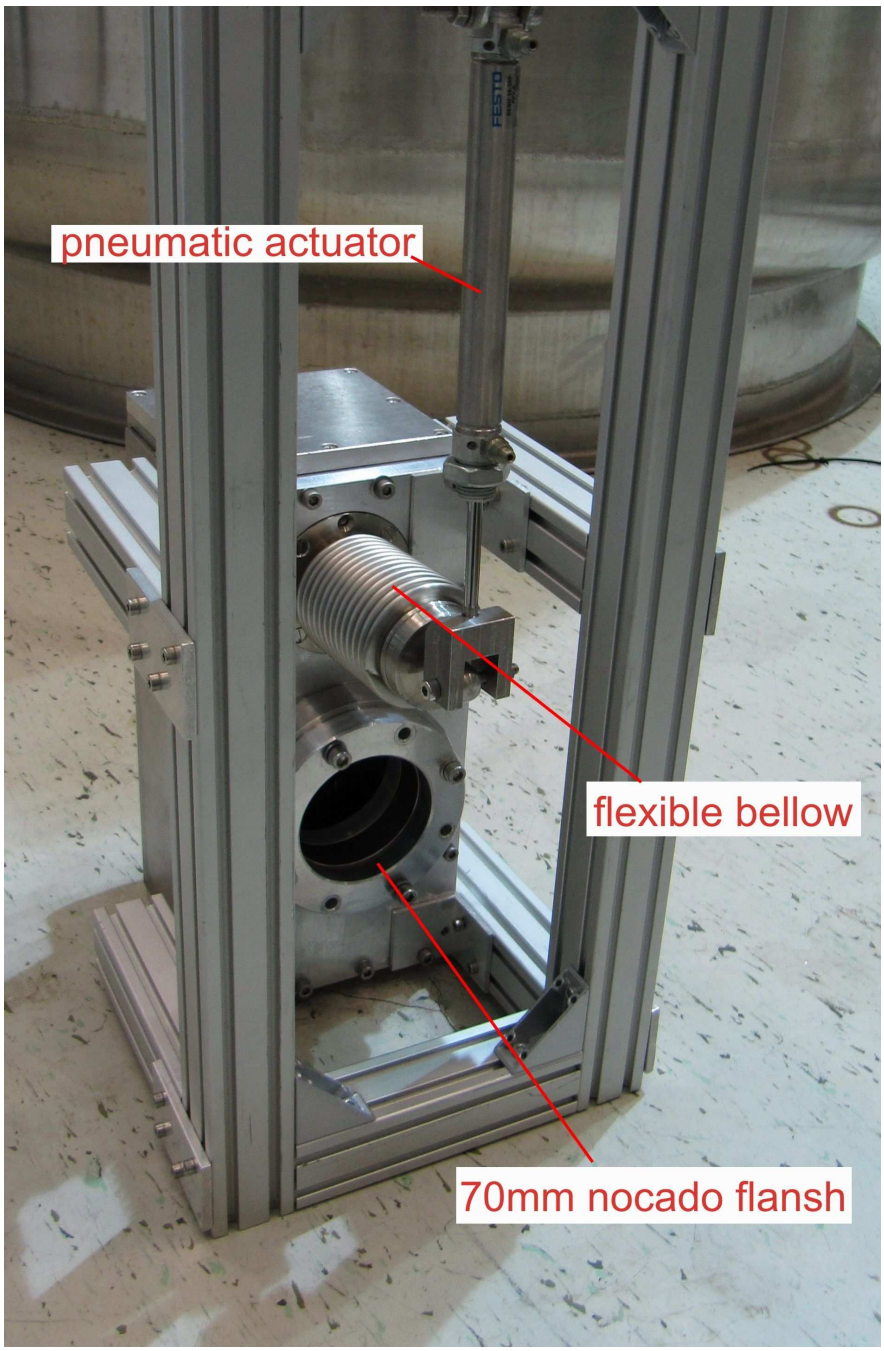

Figure 7.4: Photograph of the shutter equipped with a pressed air actuator, to drive the shutter lid.

7.2 Cubic boron nitride: a new prospective material for ultracold neutron application

The material optical potential U_f can be expressed as $U_\mathrm{f} = V - iW$ [69], where the wall-potential V describes the reflecting and the imaginary part W the absorbing behaviour of the material and is given by

$$V = \frac{2\,\pi\,\hbar^2}{m} \cdot \sum_i N_i\, b_i, \qquad W = \frac{\hbar}{2} \cdot \sum_i N_i\, \sigma_i\, v_\mathrm{th}. \tag{7.1}$$

Here, m is the neutron mass, N is the scattering center density, b is the bound coherent scattering length, σ is the sum of the absorption cross sections, σ_a, and the inelastic scattering cross section, σ_ins, at thermal neutron velocities, v_th. The sum over i includes all specific nuclei of the chemical composition. Neutrons with a normal velocity component below a critical value $v_\mathrm{c} = (2\,V/m)^{1/2}$ are totally reflected from the surface. The loss probability per reflection is expressed by the energy-independent loss coefficient $\eta = W/V$.

The v^2 dependence of the UCN velocity spectrum [26] leads to a storable UCN density which scales with $V^{3/2}$. Therefore, V has to be as high as possible to increase statistics in UCN experiments. At the same time, the η value has to be low enough to reduce absorption and upscattering losses. Besides this, specific experiments like the nEDM require additional properties of the materials, e.g., high electrical resistivity (also against surface currents) and non-magnetic properties.

The material with the so far highest known wall-potential commonly used in UCN experiments, is ^{58}Ni with $V = 346$ neV corresponding to a critical velocity of $v_\mathrm{c} = 8.1\,\mathrm{m/s}$. Nickel, however, is magnetic and conductive. So far, only beryllium oxide (BeO, $V = 261$ neV, $\eta \approx 1 \times 10^{-4}$) satisfies all criteria mentioned above. But its high toxicity may be prohibitive.

By looking for other non-toxic, non-magnetic materials with high wall potentials and high electrical resistivity, we got interested in cubic boron nitride (cBN). Due to its hardness and high wear resistance, cBN is under development as a super-hard coating (micro-hardness $> 50\,\mathrm{GPa}$, [70]) for cutting tools in the metal machining industry.

Natural boron consists of two isotopes of abundance ratio: $^{10}\mathrm{B}/^{11}\mathrm{B} = 0.248$. The calculation of the pseudo-potential of this chemical composite using Eq. (7.1), the chemical stoichiometry of BN (1 1) and the given material parameters, $\rho \approx 3.5\,\mathrm{g/cm^3}$ [71, 72], $N \approx 8.5{\times}10^{22}\,\mathrm{cm^{-3}}$, $b(^{10}\mathrm{B}) = -0.1\,\mathrm{fm}$, $b(^{11}\mathrm{B}) = 6.65\,\mathrm{fm}$, $b(\mathrm{N})$=9.36 fm, yields
$V = 324\,\mathrm{neV}$ and $\eta \approx 1.5 \times 10^{-2}$. The value for η reflects the enormously high absorption cross section of ^{10}B, $\sigma_a = 3840$ barn[73].
This drawback can, in principle, be overcame by using isotopically enriched ^{11}B in the composite ($\sigma_a = 0.0055$ barn), which results in an even higher wall-potential of $V = 351\,\mathrm{neV}$. The value of $\eta \approx 3.3 \times 10^{-5}$ in this case is mainly dominated by the absorption

of ^{14}N ($\sigma_a = 1.9$ barn) for a ^{11}B enrichment of > 99.95 %. As a first step, we started with the investigations of natural cBN.

7.2.1 Experimental determination of the neutron optical potentials of cBN

We carried out two experiments to measure the critical velocity of UCN reflected from natural cubic boron nitride, using (i) a time-of-flight (TOF) measurement in order to determine the transmission of ultracold and very cold neutrons (VCN) through a silicon wafer (380 μm) coated with natural cBN of thickness 300 nm and (ii) cold neutron reflectometry with the same sample. For comparison, a natural nickel coated sample with a layer thickness of 500 nm was investigated using the TOF method.

The cBN films were prepared in a reactive r.f. diode sputtering system using an electrically conducting boron carbide (B_4C) target. In order to reach good adhering cBN layers, a special process was used starting with an interlayer of boron carbide and continuing with graded BCN interlayers, where the carbon is replaced by nitrogen by means of an incremental change from argon to nitrogen as sputter gas. Further information on the process and the sputtering facility can be found in Refs. [70, 74, 75]. With this method, cBN layers of up to 2 μm thickness and a cubic phase content of approximately 90 % (measured by IR spectroscopy [70, 74, 75]), corresponding to a density of 3.3 g/cm^3, are produced.
The nickel coating was produced at Hahn-Meitner-Institut (HMI) by conventional DC magnetron sputtering. With this technique, it is possible to reach coating densities close to 100% of bulk material.

The time-of-flight experiment

In the time-of-flight (TOF) experiment, we determined the neutron optical potential via the critical neutron velocity from the transmission of slow neutrons through the sample. The experiment was performed at the UCN source C at the TRIGA Mainz.
In all measurements, the same amount of solid deuterium (4 mol) was used as UCN converter. We used a time-of-flight spectrometer with a three disc chopper [50] provided by the UCN group of the Paul Scherrer Institute (PSI). The neutrons were guided via electro-polished stainless steel tubes with inner diameter of 66 mm from the UCN source to the TOF spectrometer. The arrangement is schematically sketched in Fig. 7.5.

Neutrons enter from the left and pass the TOF spectrometer towards a Cascade-U detector [76] at the end of the flight path. The flight path between chopper and detector was (1006 ± 3)mm. The Al entrance window of the detector was 0.1 mm thick with an energy barrier of 54 neV from the material optical potential of aluminium and caused some reduction of the detector efficiency. With this setup, the velocity component along the forward direction can be measured.

The coated and noncoated silicon wafers (diameter 76 mm) were inserted in a foil holder placed in front of the chopper operating at a duty cycle of 4.0 % and at a frequency of 1.0 Hz.

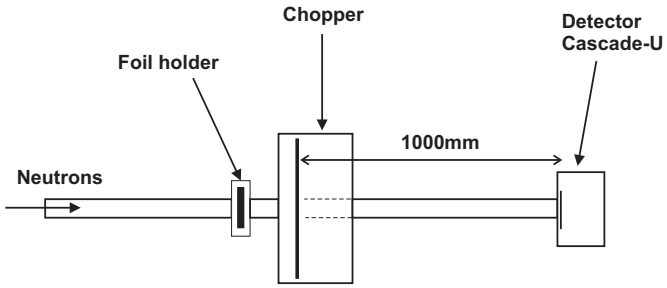

Figure 7.5: Sketch of the experimental setup for the time-of-flight experiment with a chopper.

For the correct determination of a velocity distribution with the TOF method, we assume a high guide transmission for UCN, *i.e.* a high percentage of specular reflections in the UCN guide system, which is experimentally supported by Ref. [49].

Without sample, the count rate in our TOF spectrometer was about 45 s^{-1}. As DAQ system, we used a standard TOF card from the FAST company. The TOF spectrum was started with the pulse from the chopper indicating the chopper status 'open'. Neutrons were registered with a dwell time of 1.5 ms according to their arrival time in the detector. Figure 7.6 shows the time-of-flight spectra without and with samples, *i.e.*, the nickel and cubic natural-boron nitride sample.

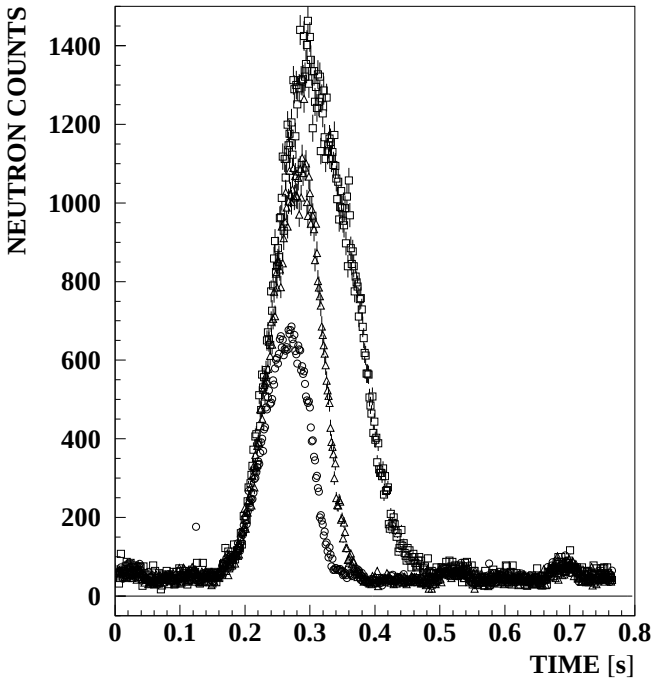

Figure 7.6: Measured time-of-flight data (i) without sample (quads), (ii) with the nickel coated silicon wafer (triangles) and the cBN coated one (circles)..

Analysis of the time-of-flight experiment

In order to extract the values of the optical potential from the layers of interest, we developed an analysis procedure [77] following three steps.

In the first step, we approximated the measured data with no sample and after background subtraction with a cubic spline function based on nine data points in order to obtain an analytic expression for the data, see also appenidxC. The χ^2 per degree-of-freedom was 2.8 which on the one hand originates from sparks in the detector and on the other hand reflects the rather simplified parametrization of the spectrum by the spline which, however, is sufficient for our purposes. In order to take this non-statistical uncertainty into account, we increased the uncertainties of the data points by a factor $\sqrt{\chi^2}$.

In a second step, we calculate the transmission of the UCNs through layers. For given values of the Fermi potential of each layer, we developed procedures to perform a numerical solution of the Schrödinger equation. Hereby, we include surface roughness via smearing of the potential step at the border of adjacent layers, cf. Ref. [78]. Matching the numerical solution of the Schrödinger equation outside the layers with the well known analytical solution for plane wave propagation allows us to calculate the value for the transmission.

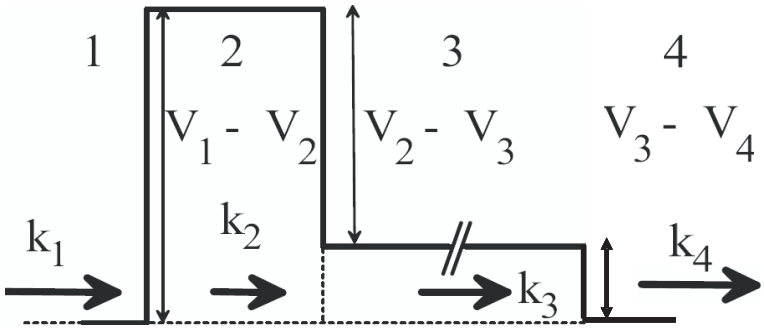

Figure 7.7: Diagram of the Fermi-potential profile (thick step line) representing a wafer coated on one side (here the left side). The transmissions $T_{i(i+1)}$ at each boundary are determined by the components of the wave vectors $\mathbf{k}_i$ and $\mathbf{k}_{i+1}$ perpendicular to the interfaces between the refractive media, cf. Eq. 7.2 for the sign convention.

The general physics model, cf. Ref. [79], of the sample is sketched in Fig. 7.7, which shows the Fermi-potential profile along the neutron path used to describe a silicon wafer coated on the entrance side. The transmissions $T_{i(i+1)}$ at each boundary are determined by the perpendicular components of the wave vectors $\mathbf{k}_i$ and $\mathbf{k}_{i+1}$. The problem can be locally reduced to one-dimensional propagation through multiple potential barriers.

Corresponding to Fig. 7.7, the general recursive formula for the perpendicular

components of the wave vectors in the consecutive media is:

$$k_{i+1} = [k_i^2 + 2m(V_i - V_{i+1})/\hbar^2]^{1/2} \tag{7.2}$$

where the V_i represent the Fermi potentials of the different media.

For the case of no interference effects in the thin films and low absorption, the reflectivity R and transmission T per neutron through each interface can be expressed as:

$$R_{i(i+1)} = \left| \frac{k_i - k_{i+1}}{k_i + k_{i+1}} \right|^2 \tag{7.3}$$

$$T_{i(i+1)} = \frac{4k_i k_{i+1}}{|k_i + k_{i+1}|^2}, \tag{7.4}$$

where $R_{i(i+1)} + T_{i(i+1)} = 1$. The k_i are real and positive.

The neutron attenuation by the respective media is given by

$$\alpha_i = e^{-\Sigma_t^i l_i}, \tag{7.5}$$

where $l_i = (d_i/\cos\varphi)$ corresponds to the total path length in the thickness d_i, φ is the sampled angle of the trajectory to the main interface normal and Σ_t^i is the effective attenuation cross section,

$$\Sigma_t^i = \Sigma_a^i + \Sigma_s^i, \tag{7.6}$$

where Σ_a^i is the (macroscopic) absorption cross section and Σ_s^i the cross section for scattering out from the main propagation direction and inelastic upscattering.

The substrates and the coatings used in the experiment are comparatively thick and have a finite roughness so that the effect of multiple reflections and interference between the interfaces is negligible and the transmission of the neutron is then given by the product:

$$\tau = \prod_i \alpha_i T_{i(i+1)}. \tag{7.7}$$

with the transition factors $T_{i(i+1)}$ given by Eq. 7.4.

In the third step, we compare our model with the measured data. For this purpose, we convolute the product of the transmission function (step 2) and the initial spectrum (step 1) with the opening function of the chopper, see Fig. 7.8. The free parameters of the fit were the mean free paths in the coated layers (cBN, Ni), the loss parameter η and the roughness of the sample. The values of these parameters were obtained by comparison of our model with the data and minimization using standard least square fitting techniques. The experimental data with the final fit are shown in Fig. 7.9. In Fig. 7.10, the curves for the velocity dependent transmission for the different measured samples as derived from the analysis are shown.

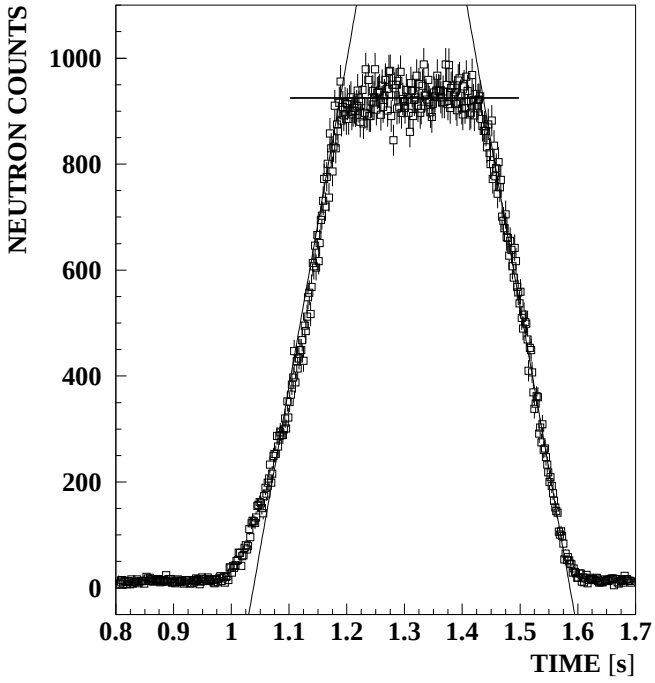

Figure 7.8: Opening function of the chopper measured at a frequency of 0.1 Hz. In the analysis, the opening function is approximated by the trapezoidal function as indicated.

In order to obtain independent layer parameters from the silicon wafer, we started with a transmission measurement of a pure Si-wafer. Because of the above mentioned aluminium window for the separation of the source vacuum and the vacuum of the experimental setup, an experimental determination of the silicon material optical potential is obsolete since the optical potentials of aluminium and silicon have very similar values (54 neV). Therefore, the theoretical value for the material optical potential of silicon (54 neV) was used for the analysis. From the fit, we extracted an experimental value for the loss parameter η of $(1.5 \pm 0.4) \times 10^{-4}$, which is in good agreement with the theoretical value of 1.17×10^{-5}. For the surface roughness we obtained a value of 9.8±0.1 nm.

Due to its ferromagnetic properties, the optical potential of nickel results in effectively two potential values, which are coupled to the neutron spin state and its orientation relative to the domain structure of the Ni film [80]. From the fit, we extract for anti-parallel spin states V = (207 ± 2) neV and for parallel spin states V = (284 ± 2) neV. The uncertainty of ±2 is the uncertainty of the fit and does not (yet) include the apparative uncertainty of the TOF calibration, see below. For η, we obtained an experimental value of $(9.0 \pm 0.6) \times 10^{-5}$, which is close to the theoretical value of 1.0×10^{-4}. For the mean free path in nickel, we obtain a value of (499 ±1) nm and for the surface roughness (10.5 ±0.1) nm. The reduced χ^2 of the fit is 4.5. These results correspond well to an amorphous Nickel layer produced by sputtering with maximum achievable densities around 98 % of bulk nickel density.

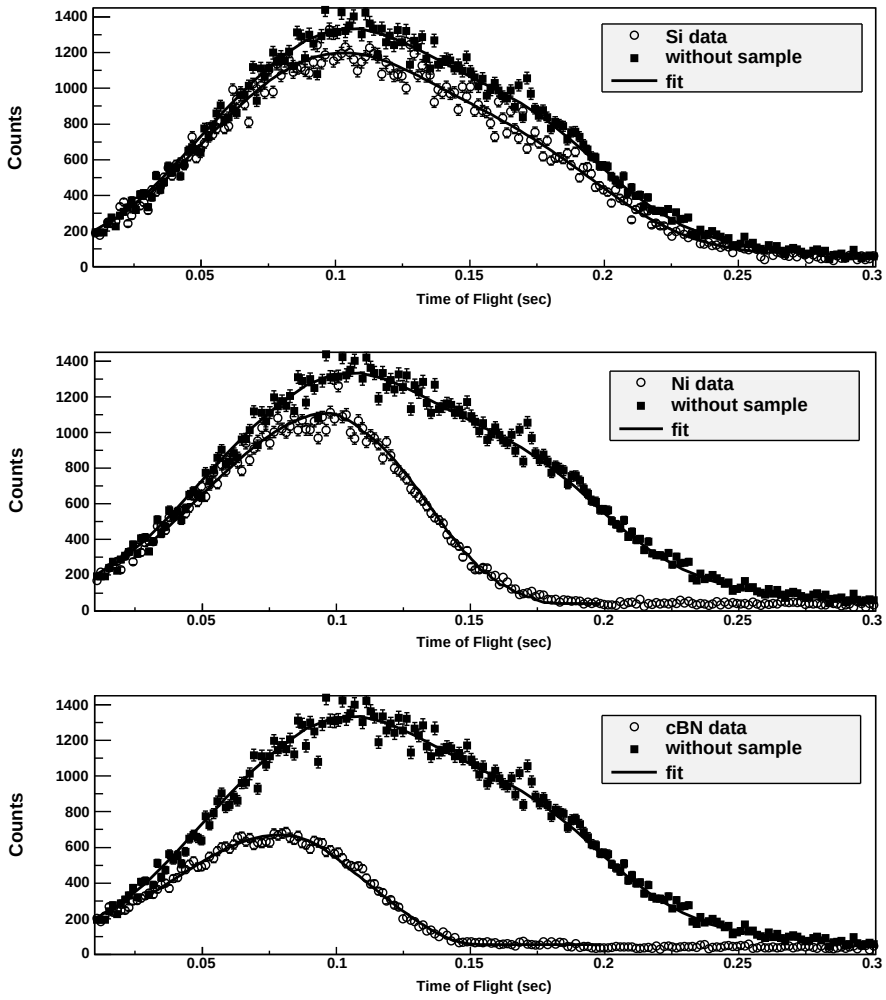

Figure 7.9: Time-of-flight data of very slow neutrons through coated silicon wafers and the fit to the data. Top: 380 μm silicon wafer. Center: 500 nm nickel coated on a 380 μm silicon wafer. Bottom: 350 nm cBN on a 380 μm silicon wafer. The corresponding time-of-flight-data without sample used to calculate the spline fitting function for unfolding the data with the time acceptance of the chopper are shown in all plots. The measured data were corrected for the chopper time offset δt (see text)

For our cBN sample, we obtain for the optical potential a value of
(305 ± 2) neV. From this and the theoretical value for cBN, we calculate a layer density of 90 % of the bulk density for our sample. For the loss parameter η, we obtain experimentally a value, $\eta = (1.8 \pm 0.3) \times 10^{-3}$, in agreement with the theoretically expected 1.5×10^{-3}. From our fit, we extract a mean free path of 2.25 μm which is a factor of 7.5 higher than the produced layer thickness. Together with a measured roughness of 42$\pm$5 nm we conclude that cBN grows in a polycrystalline layer. The reduced χ^2 of the fit was 1.7.

In order to take the χ^2 value as originating from non-statisical uncertainties into account, we increase the uncertainties ($\pm$ 2 neV) by factors $\sqrt{\chi^2}$. The main contributions

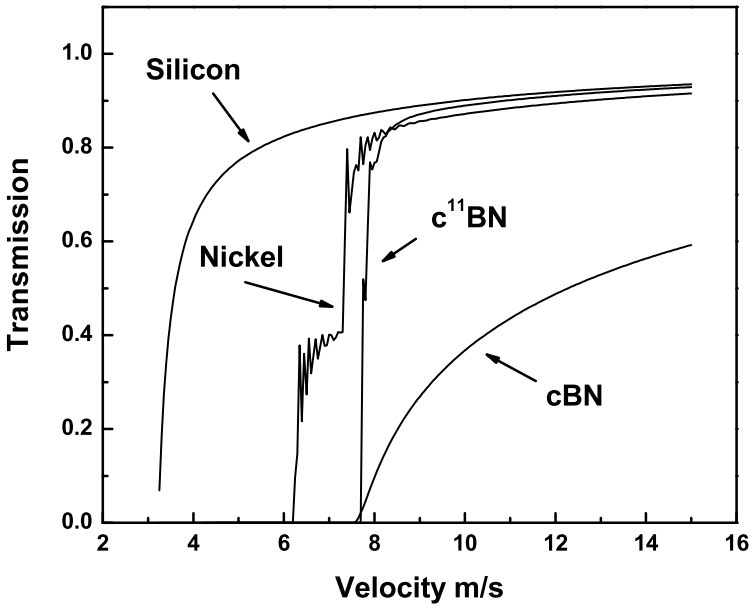

Figure 7.10: Calculated transmission of the measured silicon wafers coated with Ni (500 nm) and cBN (300 nm) layers. The theoretical transmission of an isotopically enriched $c^{11}BN$ (300nm) layer was calculated from literature cross sections.

to the total uncertainty arise, however, from the time calibration of the TOF spectrometer, $\delta V = \pm 15$ neV; the uncertainty originating from the flight path uncertainty is 2 neV. Thus, the total uncertainties of our values for the optical potentials are $\Delta V \approx \pm 15$ neV. The final results of our analysis are summarized in Table 7.1. While the optical potential of cBN has never been measured before, the values for Ni are in excellent agreement with literature values [80]. The main contribution to the uncertainty of the optical potential values originates from the uncertainty of the chopper time calibration.

In principle, one could eventually obtain a smaller total uncertainty by calibrating the cBN data to the known potential of an other material, e.g. nickel. The difficulty here arises from the unknown ratio of domains with spins parallel and anti-parallel to the neutron spin, which, in a way, could also be extracted from the fit. However, we finally prefer to the data presentation as given above.

The neutron reflectometry experiment

The second experiment using neutron reflectometry was performed at the neutron reflectometer V14 at the cold neutron beam at the reactor of the Hahn-Meitner-Institut, Berlin. This method measures the critical angle for total reflection of cold neutrons at

grazing incidence, where the velocity component normal to the surface is comparable to the velocity of UCN. Due to this fact, cold neutron reflectometry can be seen as cross-check to the transmission measurements.

The neutron critical angle of total reflection, θ_c, is directly connected with the scattering length density, *i.e.*, the term $N \cdot b$ in equation (7.1), via the formula

$$\frac{\sin\theta_c}{\lambda} = \sqrt{\frac{N \cdot b}{\pi}} \tag{7.8}$$

where λ is the neutron wavelength (4.9 Å at V14). By measuring θ_c for the samples under investigation, V can be determined using Eq.7.1:

$$V = \frac{2\pi^2\hbar^2 \sin^2\theta_c}{m \cdot \lambda^2} \tag{7.9}$$

The reflectivity function for the analysis of the data was derived with the same quantum mechanical calculation as mentioned above. However, because of the divergent beam profile, the obtained reflectivity function has to be convoluted with the known neutron beam profile.

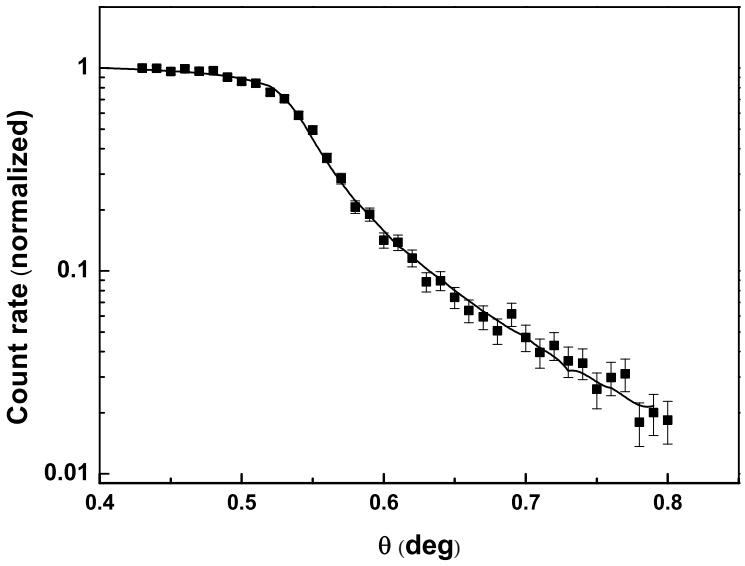

Figure 7.11: Measured cold neutron reflectometry data from a silicon wafer coated with 300 nm of cBN and the corresponding fit.

In the fit, the free parameters were (i) the scattering length density $N \cdot b$, cf. Eq. 7.8, and (ii) the roughness and composition of the surfaces (substrate and coating). The model of the cBN sample is represented by three layers, air, cBN, and silicon. The scattering lengths, b, for air, boron, nitrogen, and silicon were taken from the literature

[81]. The reduced χ^2 of the fit to the reflectivity data is 3.0. The uncertainties of cold neutron reflectometry depend strongly on the flatness and the roughness of the samples under investigation. Silicon wafers usually have very smooth surfaces but not necessarily a high flatness over the whole coated sample. This increases the uncertainty of the result. In order to take such an (unknown) apparative uncertainty into account, the experimental uncertainties were scaled [82, 83] to obtain a χ^2 of one. Figure 7.11 shows the experimental data and the fit.

The extracted value of V for the reflectometer data is shown in Table 7.1. For the thickness, we obtained a value of 350±10 nm and for the surface roughness a value of 31±1 nm. Again these results are in good agreement with the above obtained transmisson data. Since the interaction time of cold neutrons with the cBN surface is much shorter compared to the transmission experiment, we obtain a result for the layer thickness which is more realistic than the result shown above.

Transmission experiment				
Sample	V(Eq.(2))[neV]	V(exp)[neV]	v_c(exp)[m/s]	Ω[Ohm·cm]
Ni ↑↑	289	(284±15)	(7.37±0.19)	–
Ni ↓↑	211	(207±15)	(6.29±0.23)	–
cBN*	308	(305±15)	(7.64±0.19)	$> 3.4 \cdot 10^{16}$
diamond	305	- -	- -	$3.2 \cdot 10^{16}$
Cold neutron reflectometry				
cBN*	308	(300±30)	(7.58±0.38)	–

* 90% cubic phase

Table 7.1: Measured wall-potentials V of natural Ni, cBN, diamond and resulting critical velocities v_c together with the measured specific resistivities for cBN and diamond. In order to give more confidence in our analysing procedure, a Ni layer was measured additionally to verify V_{Ni} as expected from literature. The resulting error on V (30 neV) measured using cold neutron reflectometry mainly comes from the uncertainty to give an absolute value of the angle of grazing incidence.

7.3 A linear acting window chopper for Time of flight measurements

In this chapter, a new chopper system for time-of-flight (TOF) measurements will be described which is based on linear actuators. It will be demonstrated, that standard TOF measurements using disc choppers [53, 50] can gain in intensity due to the high flexibility of presented system.

7.3.1 Motivation

Time-of-flight setups can be characterized by their specific energy resolution, which is defined as

$$\frac{\Delta E}{E} = \frac{1}{2}\frac{\Delta t}{t} = \frac{1}{2}\frac{t_{open} v}{s} \tag{7.10}$$

with t_{open} being the opening time of the used chopper, v the neutron velocity and s the length of the flight path [53]. Hence, improvements in energy resolution can be achieved either by using a long flight path or by decreasing the opening time of the chopper. Unfortunately both parameters are quite limited in their variation.

The flight path should be shorter than the way, the slowest neutrons travel during one chopper cycle time T.

The opening time can be decreased quite well, but at the cost of decreasing countrate (duty cycle).

Therefore, during the construction of a conventional chopper, based on the rotation of a neutron absorbing disc, one has to find an optimal parameter set for the dedicated application [53]. Afterwards, the duty cycle of the chopper system can be only changed, by exchanging the installed neutron absorbing disc. During a running setup this results in a quite time consuming procedure.

In order to build a chopper system which enables the user to vary the chopper parameters without breaking any vacuum of the existing TOF system, one has to get rid of any rotating discs as installed in former systems, and introduce a linear motion .

7.3.2 Technical realization of a linear chopper system

In order to build a chopper system with variable opening function, a new approach away from the conventional chopper design was realized.

Fig.7.12 shows the scheme of the first prototype of the realized "linear window" chopper, which can be kept quite compact, depending on the used motor system. Instead of a rotating plexi disc, which requires a huge vacuum housing, two quadratic overlapping plexi blades (chopper lids) build the "window" and open and close the neutron guide cross section for the neutron beam.
Using two fast linear motors (P01-23x160) from Lin Mot, the blades can be moved

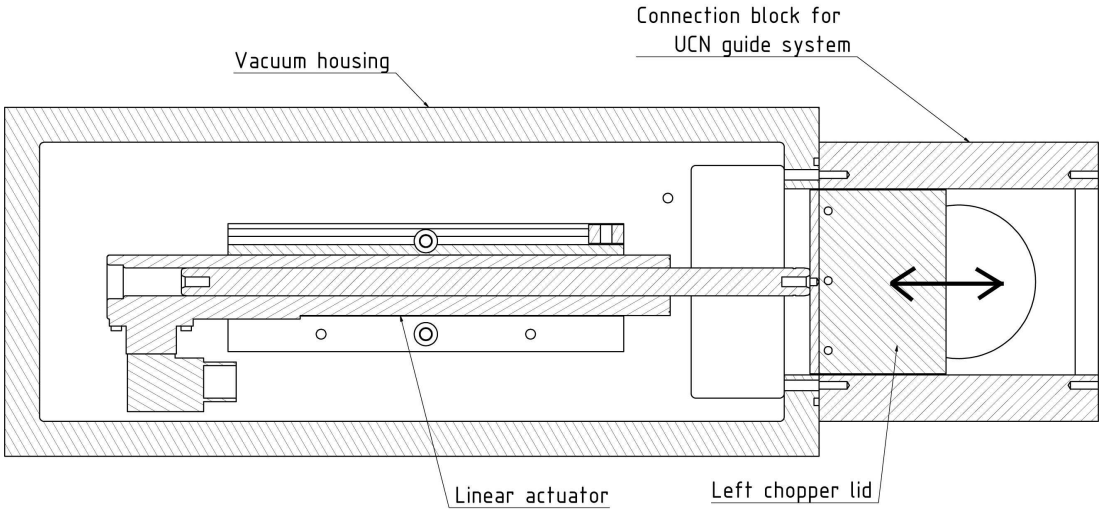

Figure 7.12: Sectional view of the shutter design. Due to the finite page size, only one motor housing is shown.

against each other with a maximal measured speed of 1.5m/s. Each linear motor is controlled by its own controller, which can be programmed (speed, opening position, acceleration) independently from each other by means of a serial interface and a special software. Including several digital I/Os it is possible, to synchronise the movement of both motors (both plexi blades) with an external 24V trigger signal.

The external trigger electronic

The so far described chopper setup itself is working without any additional hardware. Nevertheless, to carry out a TOF measurement, one has to be sure, that the timing of the chopper and the connected data aquisition system are working in phase with each other.
In coventional disc choppers, the syncronisation, the start of the data aquisition system is commonly realized with a signal of a photoelectric barrier. Just a few milliseconds before the neutron beam is open, this photoelectric barrier sends a trigger pulse and starts therefore the data aquisition system. The time between the trigger pulse and the real neutron beam opening, the so called offset δt is later used to recalculate the real time of flight spectrum. For given chopper geometries this offset depends only on the frequency of the chopper disc rotation.
In the presented linear chopper system, however, the syncronisation of the chopper and the data aquisition is done for higher flexibility in another way. With the help of a free programmable micro controller board based on an atmel μ-controller and several digital I/Os, it is possible to send phase constant trigger signals to chopper and data aquisition.
Besides the variable opening function which can be programmed inside the controllers of the linear motors, this way, also the offset and the duty cycle can be adjusted to the demands of the TOF application.

7.3.3 Experimental characterization at the ILL Grenoble

The first test and characterization of the prototype chopper was performed at the UCN turbine at the Institute Laue Langevine (ILL) in Grenoble within a short beamtime of three days. Fig.7.13 shows the test setup, which was installed similarly to conventional disc chopper setups at the test beam line of PF2. For flight path, a standard nocado stainless steel tube with a length of 1.5 m and also 0.1 m (determination of the openingfunction) was used. The neutrons were be detected with the two dimensional version of the Cascade U detector, see also appendix A which enabled us, due to his special readout electronics, to perform additionally the below described pseudo random measurements.

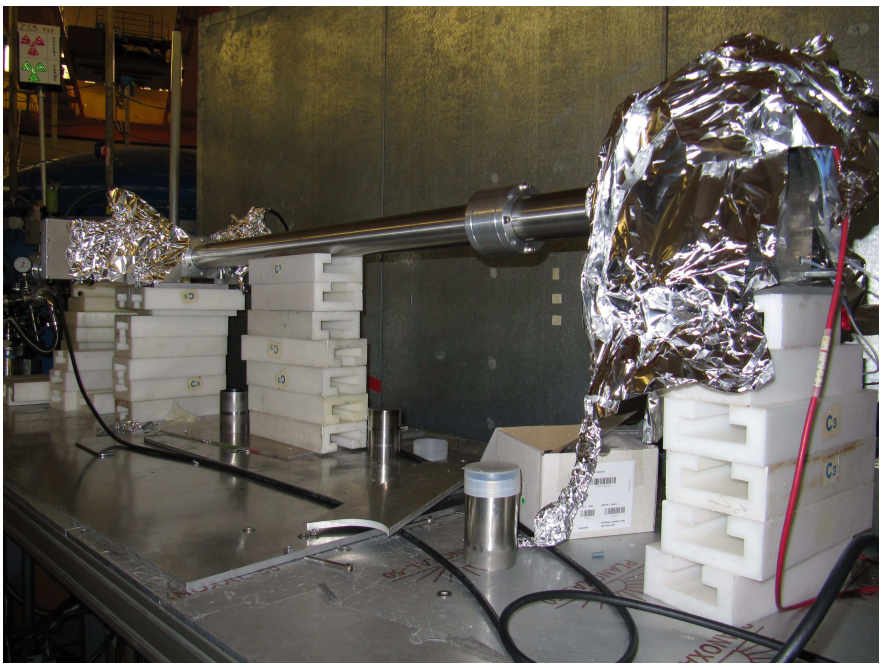

Figure 7.13: Pseudo random chopper test setup installed at the test beamline of PF2 at the ILL (Grenoble). In order to decrease electronic noise, which unfortunately existed at niveau D during our beamtime, chopper (left side) and detector (right side) were covered with aluminium foil.

The opening function

As described in detail in appendix B, the opening function is due to its finite size of great importance for the final deconvolution analysis of the measured TOF data. In the chopper existing geometry, as shown in Fig.7.12, the opening function can be

approximately described rectangular (for small slit width).

$$openfun(t) = \frac{1}{\Delta t_{open}} \Theta\left(t + \frac{\Delta t_{open}}{2}\right) - \Theta\left(t - \frac{\Delta t_{open}}{2}\right) \tag{7.11}$$

with Δt_{open} the opening time of the slit.

To determine the opening function, as described in appendix B, the neutron detector was installed as close as possible (100 mm) to the chopper exit. A picture of the setup is shown in Fig.7.14.

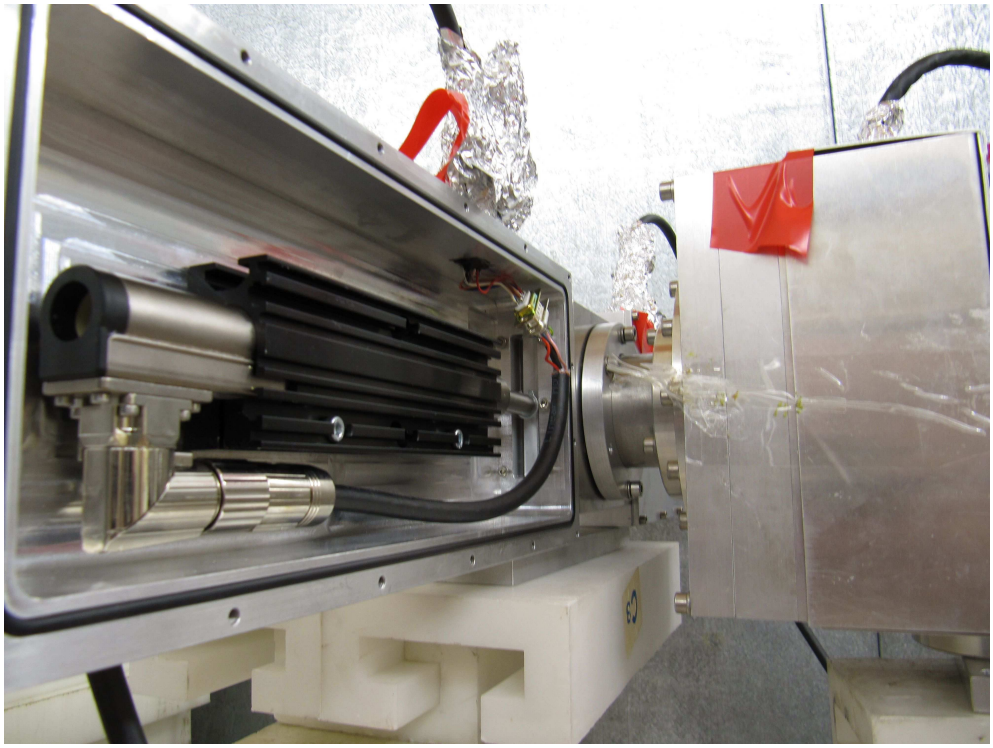

Figure 7.14: Look inside one of the linear motor vacuum housings. The linear motor is enclosed by a radiator block (black).

To demonstrate the performance of a TOF system equipped with such a chopper, opening functions for several chopper parameter settings were measured.

The opening function can be manipulated in two different ways:

- Variation of the slit size by programming the "open" position inside the motor controller
- Variation of the external trigger signal length. The chopper starts opening as long as the trigger input is set high.

1.Variation of the end position

The conventional disc chopper [53] with duty cycles around 5% possess standard slit width between 10 and 20 mm. To compare the new linear chopper opening functions with the conventional dic chopper, see Fig.B.3, determined in a first test opening functions for three different slit widths of 2 mm, 12 mm and 22 mm. To asure that the motor reached his end position, the chopper blade trigger signal length was optimized.

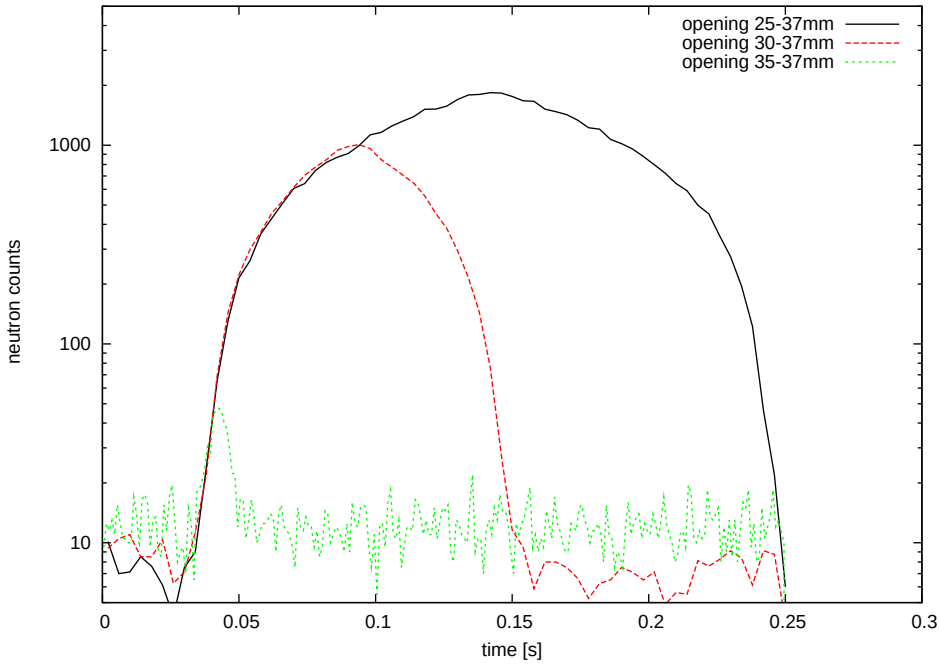

Figure 7.15: Measured opening functions for three different motor end positions. Start Position (chopper closed) was constant at 37 mm Black: Endposition set to 25 mm (Opening width = 22 mm). Red: Endposition set to 30 mm (Opening width = 12 mm). Green: Endposition set to 35mm (Opening width = 2mm). Velocity of the motor was set to 0.1 m/s.

While the closed lid position was kept constant at 37 mm, the end position was varied (25 mm, 30 mm, 35 mm).

This resulted in opening width corresponding to

$$\Delta s_{open} = 2 \cdot (x_{end} - x_{start} - 1) \tag{7.12}$$

where x_{end} and x_{start} are the finish and the start position of the motors. Due to the overlap of the two chopper blades 2 mm have to be subtracted.

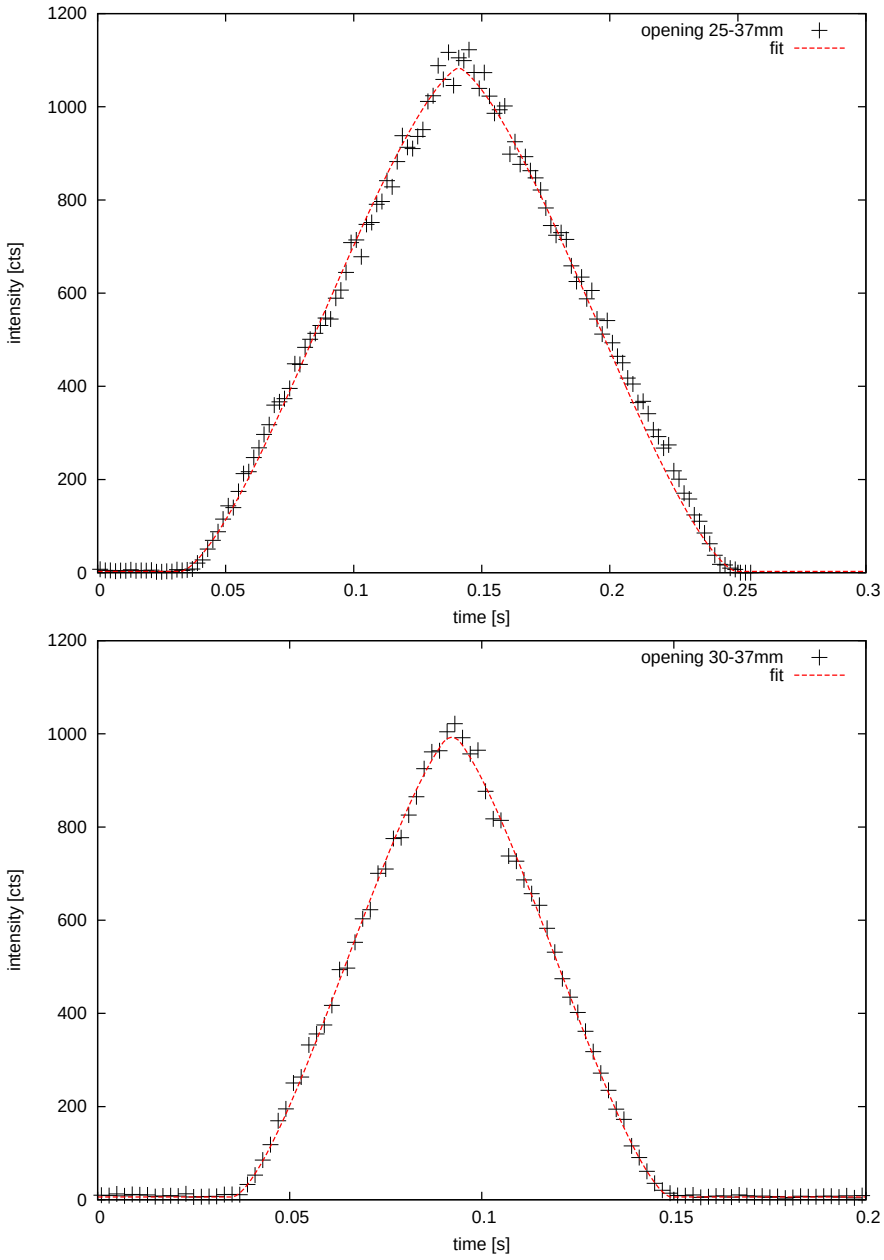

Figure 7.16: Fit of eqn.7.11 to the data. For example two fits are shown. Upper plot: Opening function for 22 mm slit. Lower Plot: Opening function for 12 mm slit.

1.Variation of the trigger signal length

As mentioned already, the chopper blades are synchronized by an external signal from a μ controller. By keeping the motor end position constant, this variable trigger signal enables the user to stretch the triangular opening function to a trapezoid (trigger length larger than opening time), or to decrease the opening width (trigger length smaller than opening time). The measurements presented in Fig.7.17 where performed under realistic motor speed conditions ($v_{blade} = 1.2\ m/s$). In order to obtain an impression of maximal resolution from the tested chopper, the end position of the motor was additionally set to the minimum of 35 mm, corresponding to a slit of 2 mm.

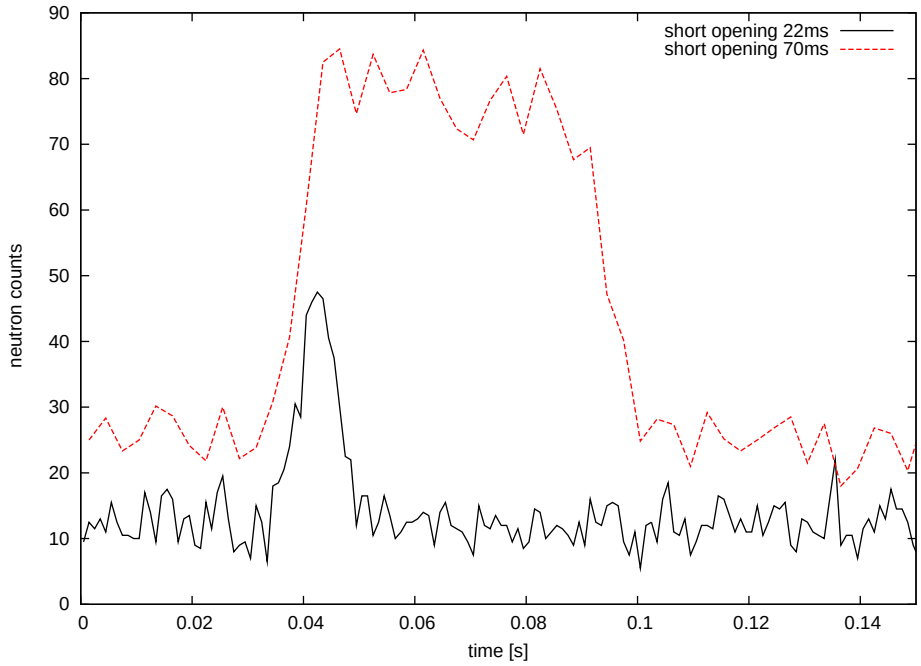

Figure 7.17: Variation of the opening function as function of the trigger signal length. Black: Triger signal length set to 10 ms. Red: Triger signal length set to 60 ms. Both opening function had a slit width of 2 mm. The motor speed was set to 1.2 m/s.

As result of this test, one can conclude, that an increase in the trigger length by about a factor of 3, increase also the opening time by the same factor. Additionally, the form of the opening function can transformed from triangular to trapezoid. For minimum opening time, we determined a value of $\approx$ 15 ms.

Determination of the chopper Offset

The procedure of the chopper offset determination is explained in detail in Appendix B. In this paragraph only the possibility of the external manipulation of the offset will be desribed and experimentally verified. As discussed already in a previous paragraph, the delay time between the trigger of data aquisition system and the trigger to the chopper

are flexible programmable. Therefore, it is possible to adjust the offset specially to the application.

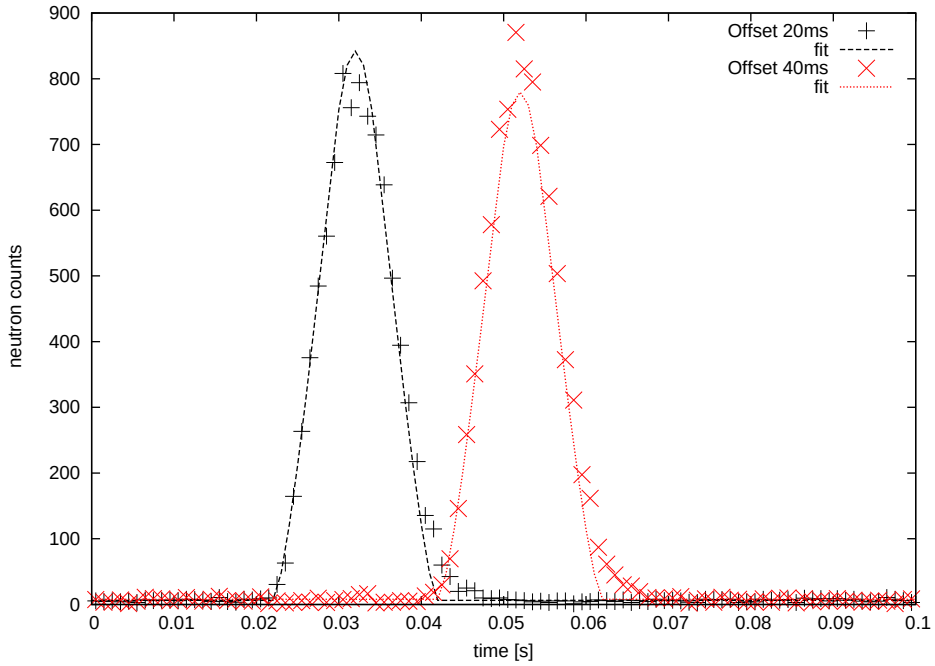

Figure 7.18: Variation of the dwell time by adjusting the delay between the motor and the data aquisition trigger signal. Black: Delay time 20 ms. Red: Dealy time 40ms. The final offset is measured as explained in Appendix B.

For example, Fig7.18 shows two measurements of the same opening function. Adding 20 ms to the used delay time, shifts also the maximum of the opening function (red curve) by 20 ms.

7.3.4 The neutron optical wall potential of boron carbide B_4C

As already mentioned in the previous section 7.2, compound materials based on boron-11 are of great interest for coatings of future UCN equipment. Besides cubic boron nitride (cBN), we got also interested in boron carbide, B_4C, the initial target material used for the production of cBN layers. With the given scattering length for ^{11}B and the additional scattering length of $b(C) = 6.646$ fm [81] for carbon, one expects for a bulk density of $\rho(B_4C \approx 2.5$ g/cm^3 a neutron optical wall potential of $V \approx 235$ neV. This number is sligthly smaller than the neutron optical wall potential of nickel and beryllium ($V \approx 250$ neV), but from theory coatings with boron carbide, should result in a very low loss parameter η of $\approx 10^{-7}$ ($\sigma_a = 0.0035$ barn). Additionally, due to its non ferromagnetic properties, this material can be used for coating of non depolarizing neutron guides which are useful for the adaption in high magnetic fields of superconducting neutron polarizers. With the development and investigation of the surface characteristic it's may be also possible to replace existing non depolarizing supermirror coatings

based on non magnetic NiV or NiMo compounds.

Measurement of the neutron optical potential of B_4C by time-of-flight

As first experimental application of the new chopper system, the transmission of ultra-cold and very cold neutrons through a silicon wafer (thickness $\approx 380\mu m$) coated with a layer of 250 nm of enriched $^{11}B_4C$ (enrichment 96.5%) was investigated. Analoque to the described method in section 7.2, the presented TOF setup was used. The flight path had a length of 1500 mm. The data presented in Fig.7.19 was accumulated within a measurement time of 1 hour.

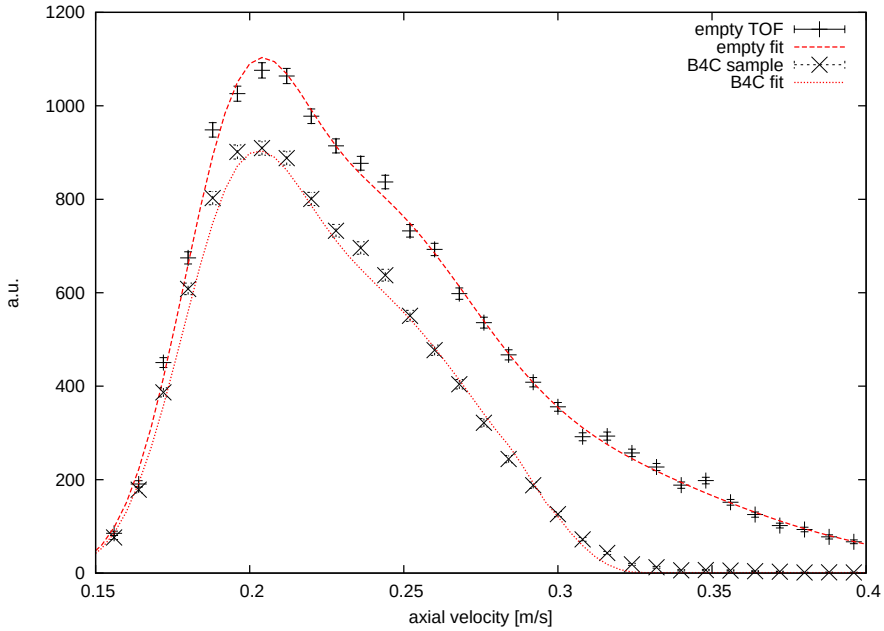

Figure 7.19: Time-of-flight data of very slow neutrons through a 380 μm silicon wafer coated with 250 nm of B_4C and the fit to the data. The corresponding time-of-flight-data without sample used to calculate the spline fitting function for unfolding the data with the time acceptance of the chopper are also shown in the plot. The measured data were corrected for the chopper time offset δt = 71 ms

Using the standard deconvolution and analysis procedure, described in section 7.2, we obtained in a first rough analysis with a reduced χ^2 of 5.2 for the optical potential a value of (220 $\pm$ 2) neV. The broader angular distribution of the neutron beam at the ILL PF2 testbeam line (in comparison to the UCN C beamline in Mainz) caused some diffusive scattered neutrons which lead to a small number of delayed neutrons and therefore a worse χ^2. For the loss parameter η, we obtain experimentally a value, $\eta = (5.7 \pm 0.5) \times 10^{-4}$, in agreement with the theoretically expected 5.6×10^{-4}. From our fit, we extract a mean free path of (300 $\pm$ 5) nm which is in good agreement with the produced layer thickness.

7.4 A pseudo random time-of-flight system for ultracold neutrons

Time-of-flight measurements with UCN, especially at the existing UCN source in Mainz (at 100kW reactor power), are mainly limited by their poor countrate. Standard single slit measurements with duty cycles in the range of a few percent result in mesaurement times of 1 hour and more depending on the UCN flux and sample. In this section, the pseudo random method, which for the first time was used in the 1960's in thermal neutron spectroscopy [84], will be introduced and adapted to the TOF measurements with slow neutrons. Using this method, a gain in countrate of one order can be expected.

7.4.1 Theoretical aspects

In an ideal time-of-flight experiment, one measures the time elapsed between the trigger signal at the beginning of the flight path and the detector response. Without a change in velocity of the neutron during flight, one can directly derive from the arrival time the velocity distribution parallel to the flight path.

single slit method

The conventional way to obtain a time-of-flight makes use of a standard single slit chopper, [53]. Here, the neutron beam is chopped by a disc with one opening slit. Additionally, a trigger signal is sent to the data aquisition system which sets the start-

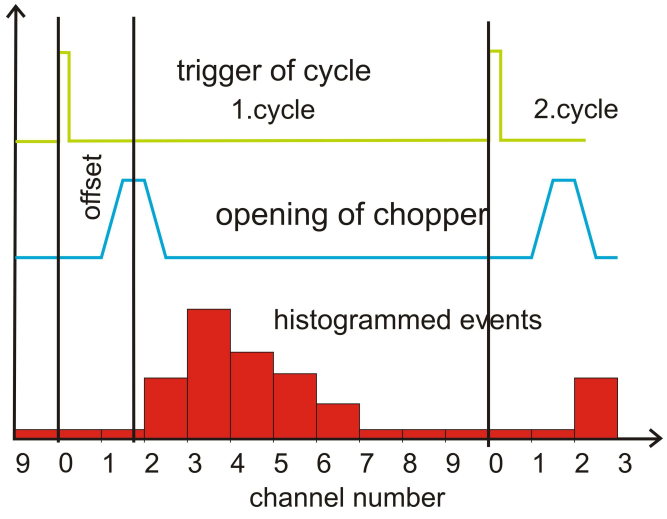

Figure 7.20: Time scheme of a conventional single slit Time-of-flight setup. Once per chopper cycle a trigger signal (green) resets the time event histogramm (red) channel to zero. The chopper disc (blue) opens the beam with a predefined offset delay time just after the trigger signal.

ing time of the center of beam opening. The detected neutrons are assorted in time

channels according to the time elapsed after the trigger signal. With the next trigger signal the data aquisition starts again at the first channel, i.e. the spectra accumulated during each cycle with a length of T are summed up and, in principle, it is only possible to resolve time differences modulo T. The finite width of the slit superimposes a time uncertainty onto the measured time-of-flight spectrum, which can be derived as a convolution of the real time of flight spectrum $F(x)$ with the specific opening function $Openf(x_0)$ of the slit.

$$G(x) = \int F(x - x_0) \cdot Openf(x_0)\ dx_0 \tag{7.13}$$

pseudo random method

In this TOF method, the neutron beam intensity is enhanced by allowing the beam to pass not only through one slit per cycle, but through a sequence of unit slits distributed over the chopper cycle with a length of T. Using a well defined periodic binary sequence a_i of ones (slit) and zeros (no slit), e.g. Fig7.21, it is possible, to recover the initial neutron TOF spectrum, which is convoluted with the overlapping neutron bunches of the different slits.

The sequence a_i, impressed on the chopper in our case is due to its finite length a pseudo-random binary sequence (PRBS) of length $N = 2^n - 1$, which has k slits corresponding to , i.e. the duty cycle is enhanced by a factor k compared to the single slit measurement (see also Fig.7.20. Its randomness reveals itself in the autocorrelation of the sequence, which is delta function like, i.e. maximal at $\tau = 0$ and constant otherwise:

$$A(\tau) = \sum_i a_i a_{i+\tau} = \begin{cases} 2^n - 1, \tau = 0, \\ 2^n - 2, \tau \neq 0 \end{cases} \tag{7.14}$$

where the indices must be taken modulo N. Unlike a true random sequence, a_i is finite and the modulation of the beam is periodical with period N.
Associated with a_i one implements a second sequence x_i with elements $x_i \in -1; 1$

$$x_i = 2 \cdot a_i - 1 \tag{7.15}$$

The crosscorrelation, which is given by

$$C_{ax}(\tau) = \sum_i x_i a_{i+\tau} = \frac{1}{2}(N+1)\delta_{\tau 0} \tag{7.16}$$

connects explicitly the sequence x_i with the modulation sequence a_i. This cross correlation can later be used to reveal the real time of flight data.

Extraction of the single slit spectrum from the pseudo random data

The convolution of a time-of-flight spectrum with a given opening function of the chopper can be represented by a matrix multiplication. The binary sequence of ones and zeros, used to form a pseudo random sequence, given by a_i, is from here on denoted as

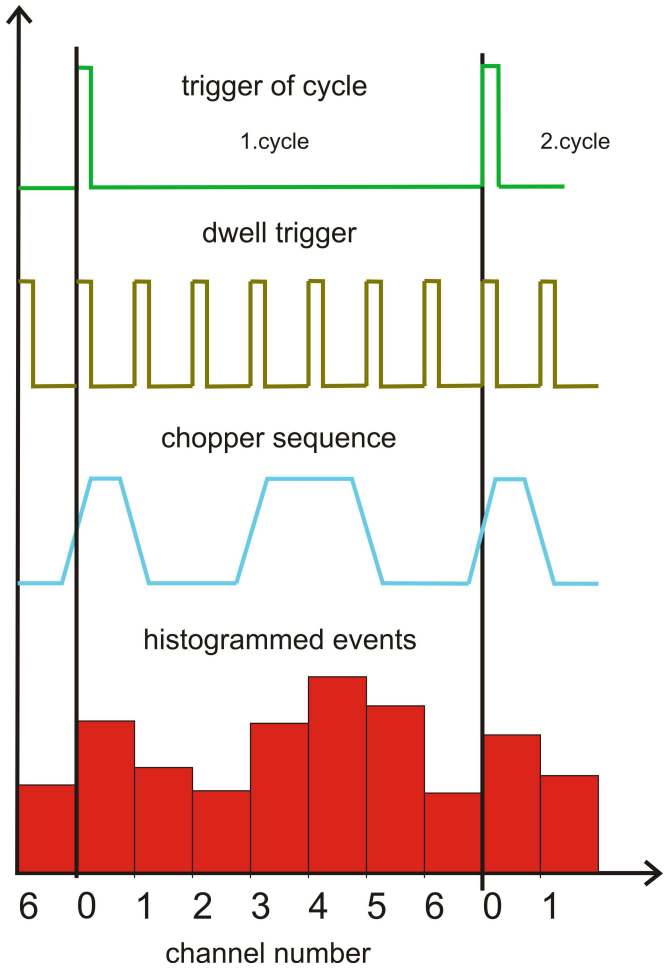

Figure 7.21: Time scheme of a pseudorandom time-of-flight setup. Once per chopper cycle (after a time T) a trigger signal (light green) resets the time event histogrammer (red) channels to zero. The chopper disc (blue) opens the beam with a predefined binary pseudo random sequence (e.g., 1,0,1,1,0,0,1,0,1,0), used later to recalculate the single time-of-flight spectrum. To save the phase stability of the chopper and the time hystgrammer, a second trigger (dwell time trigger, dark green) is used.

the vector $\hat{a}$. The order of the elements in this sequence is the timewise order in which the beam is open. Writing the time-of-flight spectrum also as vector $\hat{f}$, the convoluted pseudo random signal $\hat{s}$ is given by:

$$\hat{s} = M(\hat{a})\hat{f} \tag{7.17}$$

Fig.7.22 shows in an illustrative way the previous matrix multiplication.

Herein, the first row $\mathrm{M}(\hat{a})_{1,j}$ of the matrix $\mathrm{M}(\hat{a})$ determines the signal in the first channel of the obtained pseudo random spectrum. In the first channel, the signal from neutrons is stored which have a time-of-flight in the interval f1 and pass through the first opening a1. Furthermore, this channel contains the signal from those corresponding to f2, but

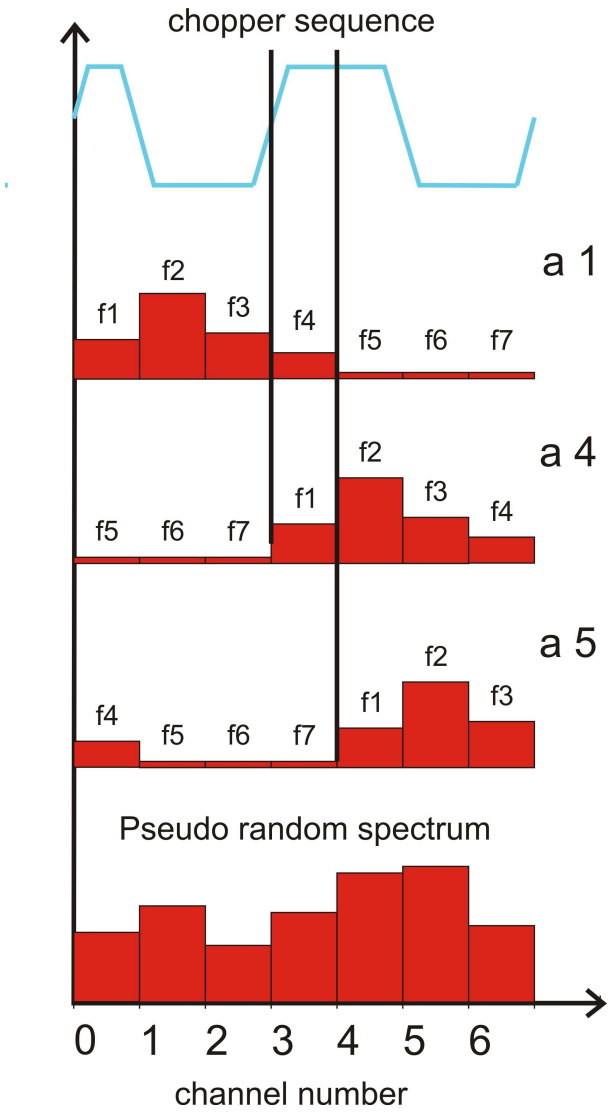

Figure 7.22: General illustration of eqn. 7.17. The vector $\hat{s}$ is calculated as the sum of all single slit TOF histograms, a1,a4,a5 .

having passed through the last opening a_N just before the new trigger signal was given. In this manner the whole matrix is given as:

$$M(\hat{a}) = \begin{pmatrix} a_1 & a_N & a_{N-1} & \cdots & a_2 \\ a_2 & a_1 & a_N & \cdots & a_3 \\ \vdots & \vdots & \vdots & \vdots & \vdots \\ a_N & a_{N-1} & a_{N-2} & \cdots & a_1 \end{pmatrix} \tag{7.18}$$

The cross correlation of the signal is its multiplication with the inverse matrix of $\mathrm{M}^{-1}(\hat{a})$. The rows of $\mathrm{M}^{-1}(\hat{a})$ are the cyclic permutations of the sequences $\hat{x} = 2\hat{a}-1$ (see eqn.7.15) corresponding to the columns of $\mathrm{M}(\hat{a})$.

To process the obtained raw data, the raw spectrum has to be multiplied with the in-

verse of the matrix whose elements are the M_{ij} times the $N \times N$ unity matrix.

To visualize this mathematical operation, a standard gaussian distribution (see Fig.7.23) is convoluted by matrix multiplication with the correlation matrix of a 23 bin pseudo random sequence.

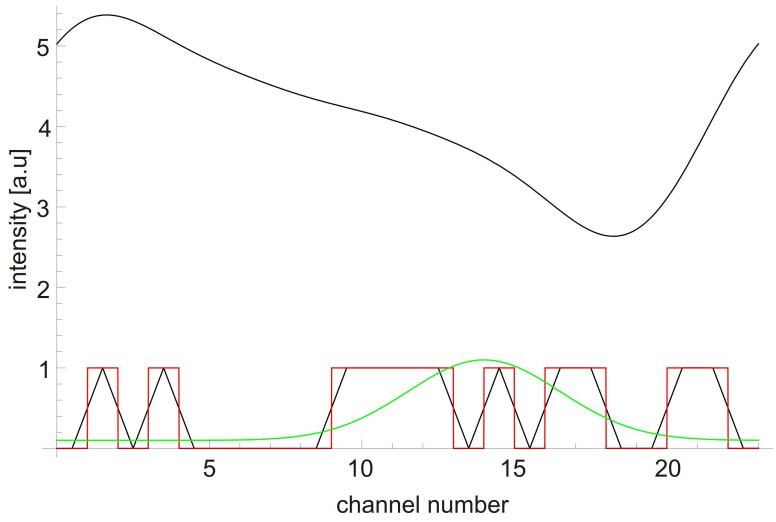

Figure 7.23: Result (black curve) of the convolution of a 23 binary sequence (black curve under the red ideal opening function), including already a realistic shape of the opening function with a gaussian distribution (green curve).

Error Analysis

Consider a time-of-flight measurement with N channels of width Δt and a chopper cycle with a period $T = N\Delta t$. Including a background intensity u_n over all channels , the signal response in channel n accumulated during M chopper cycles is given by

$$r_n = M\sum_m a_{n-m} f_m + u_n \tag{7.19}$$

with $u_j = u/n$. According to eqn. 7.15, the single slit spectrum times the gain in intensity due to the k slits can be calculated via the cross correlation

$$F_l = M f_l = M\sum_{j=1}^{N} x_{l-j}(r_j - u_j) \tag{7.20}$$

With the assumption that the errors of r_j and u_j are poisson distributed, one can derive from standard error propagation the error of F_l as

$$\Delta F_l = \sqrt{\sum_{j=1}^{N} x_{l-j}^2 (r_j + u_j)} \tag{7.21}$$

$$= \sqrt{\sum_{j=1}^{N}(r_j + u_j)} \tag{7.22}$$

$$= \sqrt{(r+u)} \tag{7.23}$$

where r and u represent the total number of detected events. The relative error of each time channel is therefore

$$\frac{\Delta f}{n_{pr}} = \frac{\sqrt{r}}{n_{pr}} \tag{7.24}$$

with n_{pr} being the detected events in the channel. In comparison with the statistical error per time channel of the single slit method

$$\frac{\Delta f_{SS}}{n_{SS}} = \frac{1}{\sqrt{n_{SS}}} \tag{7.25}$$

the pseudo random method gives a smaller error correlated with the number of chopper openings k.

7.4.2 First experimental realization of a Pseudo Random chopper for ultracold neutrons

The main experimental challenge in the pseudo random technique is given in the synchronisation of the chopper openings and the dwell time of the data aquisition system, see also Fig.7.21. In comparison with the single slit mode, the dwell time channels in pseudo random mode cannot be consecutively increased inside the data aquisition system. To prevent the data aquisition from phase shifts with respect to the chopper, the dwell time channels have to be increased by the chopper itself.
Fortunately, the 2D Cascade detector is aditionally to the existing chopper cycle trigger equipped with a second trigger input which enables the switching of the dwell time by external signals.
From Fig.7.22 it's quite obvious, that any jitter in this synchronisation would cause immediately not recalculateable results of the pseudo random spectrum and therefore to huge errors in the extraction of the single slit TOF events.

In order to synchronize a conventional disc chopper system (with a multislit disc) with any data aquisition system would recommend:

- a high accuracy during production of the slits,
- a well balanced disc, to avoid mechanical jitter of the rotating disc.

Asumming chopper discs out of plexiglass, this challenge is almost impossible.

A way out, is the use of the described linear "window" chopper system. Using a third TTL output of the described μ-controller board and a more complex programm code,

the final success only depends on the speed and its connected resolution of the choppersystem, see also eqn. 7.10.

The first pseudo random sequence

To guarantee a definite and simple extraction of the initial time-of-flight distribution from the measured pseudo random data, one has to find first of all an adequate binary sequence, which has to fulfill in our case two important requirements:

- Because of easier microcontroller programming, the binary sequence should start with 0 and finish with 0.
- The cross correlation matrix should be easyly invertible

In order to test the functionality of the proposed pseudo random chopper at already useable resolution, we decided to use a binary sequence with a length of $N = 31$. Unfortunately, there exists in literature no binary sequence with the defined requirements. Therefore, an optimization routine in ***Mathematica*** was written [85], with the goal to find an optimal binary pseudo random sequence under 5 billion sequences diced by a random generator. As final result, the following sequence was programmed into the used μ-controller board.

$$(0,1,0,0,0,0,0,1,1,0,1,1,0,0,1,1,1,1,0,1,0,0,1,0,1,0,1,1,1,0,0) \tag{7.26}$$

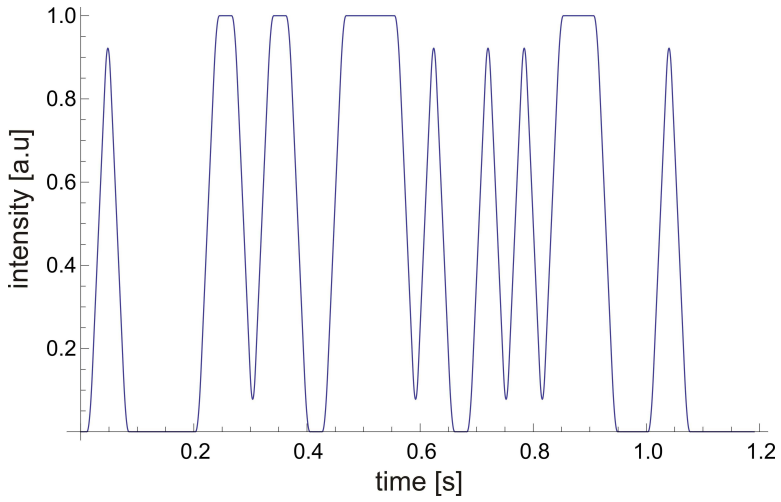

Figure 7.24: Realistic binary sequence with a length of 31 channels. The opening function used in this sequence has a t_{rise} of 9ms and a total length of 32ms. After 992ms, the cycle starts again.

Due to the triangular shape of the chopper opening function, the programmed chopper sequence can be approximated by Fig.7.24.

Experimental proof of principle

After the succesfull test and characterization of the linear window chopper at the UCN test beamline at the UCN turbine at the ILL (institute Laue Langevin), there was still enough time to test also for the first time TOF technique described on the last few pages. With the preinstalled setup, shown in Fig.7.13 and a flightpath of 1500 mm we took in a

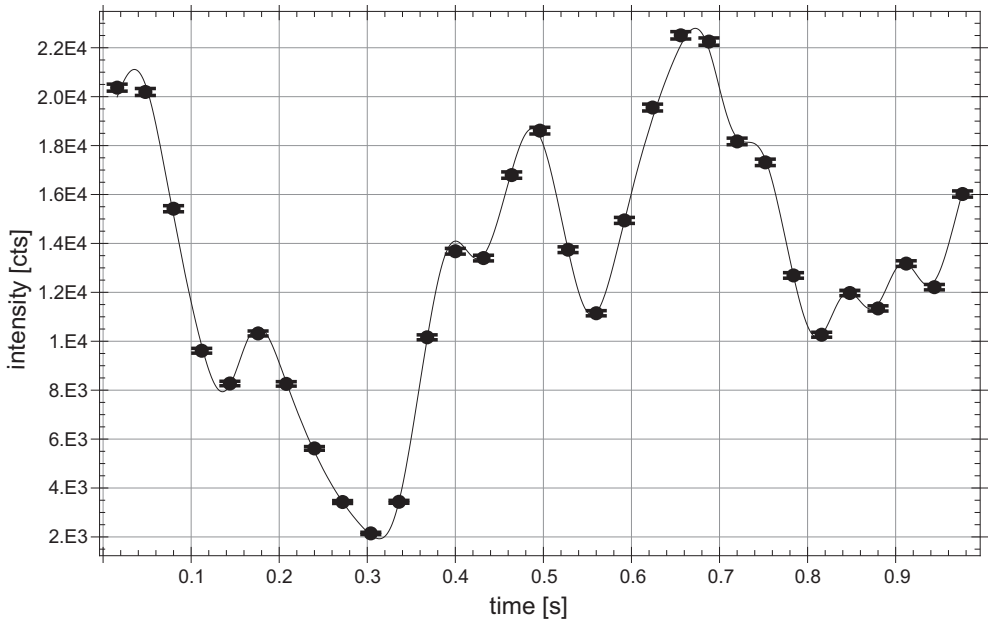

Figure 7.25: First measured pseudo random spectrum of the neutron spectrum of the test beam line PF2 obtained within a measurement time of 2 min.

In order to compare the pseudo random data with a single slit measurements, one has to accumulate a standard TOF spectrum using the same opening function as for the pseudo random mode. Within a data acumulation time of 1 h and an opening function with a rising time of 9ms and a total length of 32ms the following single slit spectrum, Fig.7.26 was taken. By comparing both extracted spectra, one can arrive at two conclusions:

1. The extracted spectra have both a maximum at 0.13 s, corresponding to a peak velocity of 11.5 m

2. Due to the short flight path and the only resolution of 31 channels, the pseudo random spectrum occupies due only one third of the time axis. Therefore it is impossible to see any more details like in the single slit spectrum with a dwell time of 2.5 ms and 500 channels. In order to obtain higher resolution, longer flight paths and a higher number of channels are important for following tests.

As expected from our test convolution result, see Fig.7.23, the proof of principle can only be delivered after the succesfull extaction of the single slit spectrum with the known inversion matrix, see also Fig.7.27.

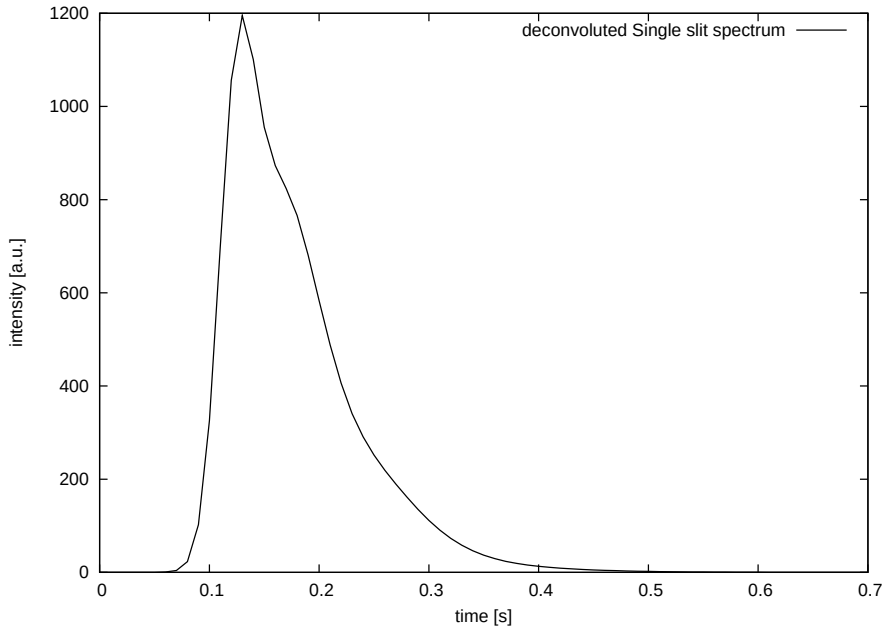

Figure 7.26: Deconvoluted time-of flight-spectrum of the PF2 test beam. The deconvolution of the data was done by using a mathematical routine which is explained in more detail in appenidxC

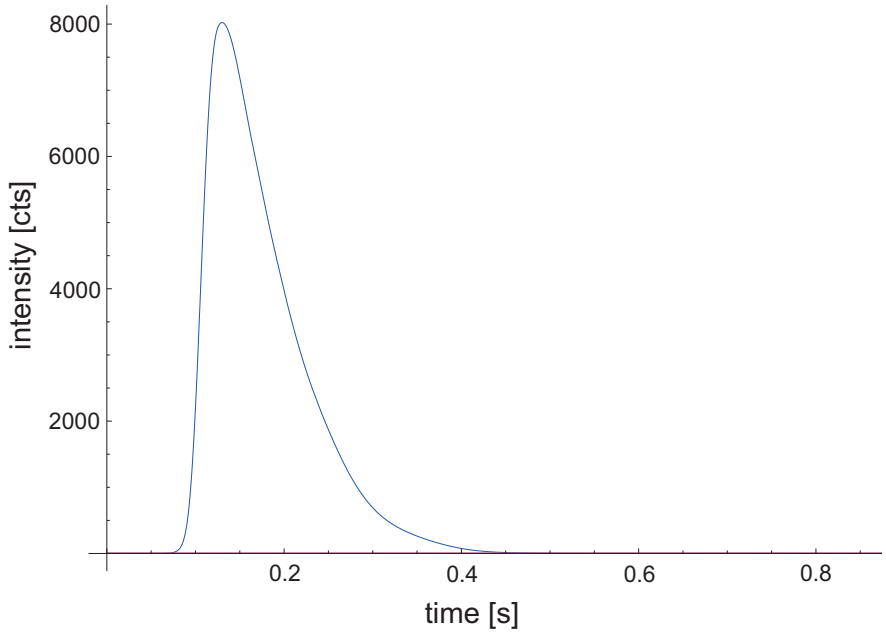

Figure 7.27: Single slit spectrum extracted from the measured pseudo random spectrum of Fig.7.25. The x-axis represents the time axis and the y axis the intensity.

The neutron optical wall potential of boron carbide B_4C measured by Pseudo Random TOF

For the final proof of the principle and to show the advantage of the proposed methode, we measured like in single slit mode, the transmission of slow neutrons through the characterized boron carbide (B_4C) sample. Similar to the single slit measurement, the sample was installed in the foil holder in front of the chopper. The data shown in Fig.7.28 was accumulated in a measurement time of 2min.

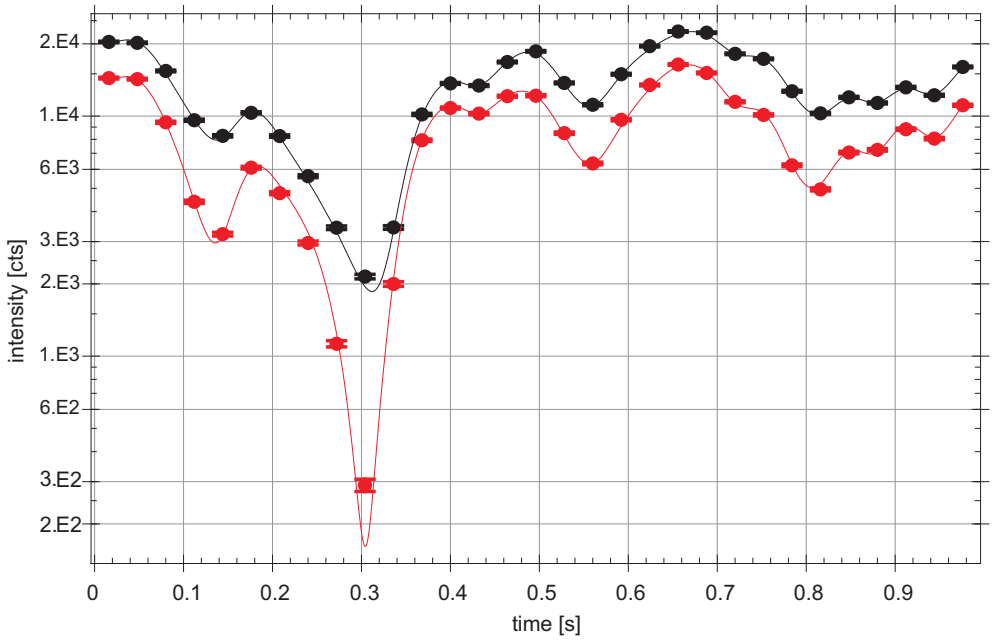

Figure 7.28: Transmission measurement of a B_4C sample (red points) obtained with the pseudo random method within a measurement time of 2 min. The fit of the B_4C sample was done by combining the empty measurement (black points) with the quantum mechanically calculated transmission function, see also section 7.2

In order to analyze the data, the pseudo random spectrum with the empty foil holder, Fig.7.25 was combined in a *Mathematica* fit routine [85] with the quantum mechanical calculation of the transmission function, section 7.2. With a reduced $\chi^2 = 8.5$ we obtained with an energy resolution of 6% a density for the the mesured B_4C-sample of $96.7 \pm 1\%$ bulk density. This number is in good aggrement with the result presented above.

7.5 Straight and bent guide parts for ultracold neutrons

Comparing measured time-of-flight spectra with the results of the implemented Monte Carlo code, see also appendix E, huge discrepancies in transmission for faster neutrons are observed. The fact that the transmission properties of the used straight neutron guide parts are quite well charaterized [62], we suspected a lower transmission of the installed bent section to be the reason for the worse TOF results.
This lower quality can be mainly explained by the higher surface roughness, which is an artefact of the forming process. To obtain higher transmission, the roughness of the inner surface has to be improved. Because of an impossible further polishing, we decided to produce new bent sections out of glass, which offer in comparison with the stainless steel tubes surface roughnesses in the range of a few Å. To increase the low neutron optical potential of glass, the assembled bents were coated with a high reflective NiMo layer in the existing sputter facility [60].
In order to test the performance of the new bent sections, two TOF measurements were carried out at the UCN source C at the reactor TRIGA Mainz. Fig.7.30 shows as a result two deconvoluted velocity distributions where the nocado and the glass bent were used as deflection of the neutron beam.
A significant gain factor of ≈ 2 in neutron output especially for neutrons with velocities higher than 9m/s can be reached with higher quality surfaces.

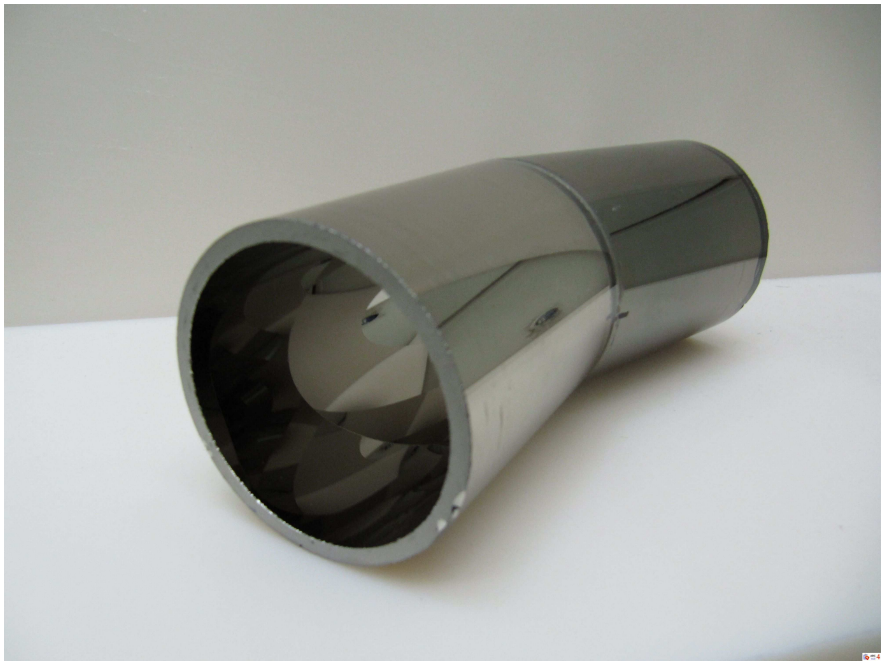

Figure 7.29: First self made glass bent coated in the new sputter facility in Mainz.

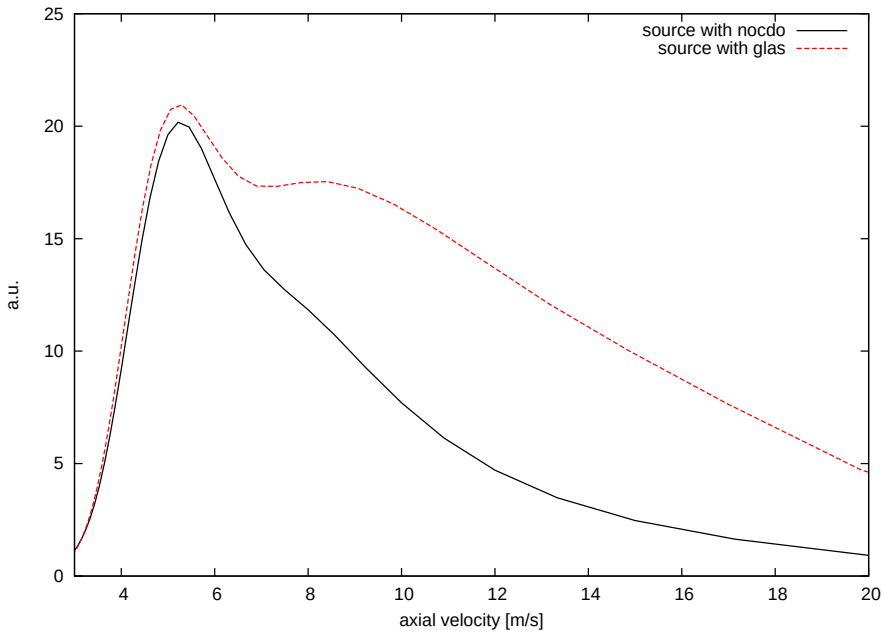

Figure 7.30: Deconvoluted spectra of the source output with different bent parts.

7.6 Conclusions and outlook

Future UCN experiments will certainly gain in performance due to new growing UCN facilities around the world. Besides these highly intensive neutron beams, also new techniques have to be developed, which will improve also the systematics of these experiments. Having access to our own UCN source at the reactor TRIGA Mainz, we had been able to test in the framework of this thesis several interesting ideas, which may improve existing and future experiments.

The neutron optical potential value V of the highly resistive natural cubic boron nitride was determined experimentally for the first time via the energy dependent transmission of very slow neutrons through a cBN layer, $V_{\mathrm{trans}} = (305 \pm 15)$ neV and by cold neutron reflectrometry, $V_{\mathrm{refl}} = (300 \pm 30)$ neV. Both values agree with each other and are in excellent agreement with theoretical expectations, $V = 308$ neV, obtained from eqn. 7.1 and for the fraction of the cubic phase, which was determined independently by infrared spectroscopy to be about 90 % [70, 71, 72] for the specific PVD process. Using isotopically enriched ^{11}B, c^{11}BN can be an interesting coating material for the future nEDM2 experiment, which is at the moment in construction at the PSI.

Furthermore, the optical potential value V of isotopically enriched $^{11}B_4C$ was measured for the first time. Using the same transmission method as done for cBN, a neutron optical potential of $V_{\mathrm{trans}} = (218 \pm 15)$ neV could be determined. Due to its nonmagnetic properties and its high neutron optical potential, $^{11}B_4C$ can be an alternative coating material for nondepolarizing ultracold neutron guides. In a next investigation step, the loss parameter η, which is expected to be of the order of $\approx 10^{-7}$ ($\sigma_{\mathrm{a}} = 0.0035$ barn) has to be evaluated in an independent storage measurement.

Besides the investigation of new coating materials, an infrastructure for the production of neutron optical components was implemented in a dedicated laboratory. This infrastructure resulted in the establishment of improved straight and bent guides for ultracold neutrons, which helped to increase notably the performance of the existing UCN source.

Finally, a new TOF technique based on a pseudo random chopper was succesfully implemented for UCN transmission applications at the ILL in Grenoble. With its huge duty cycle of close to 50% this method will help to increase the statistical accuracy and maybe the energy resolution of future TOF setups and simultaneously decrease the necessary measurement time. Especially the UCN output of the existing UCN source C at the reactor TRIGA Mainz operating at 100kW will gain a factor of 15 within standard transmission measurements.

Appendices

Appendix A

UCN detectors and their characteristics

The neutron is, as his name reveals, an uncharged particle. Standard particle detectors based on ionisation processes obtain only a signal from an arriving neutron, if this neutron is converted in an absorption process into charged particles which can be detected. Several substances can used as neutron converters in neutron detectors:

^{3}He + n	$\rightarrow$	^{3}H + p + 764 keV	$\sigma_{th} = 5330b$
^{6}Li + n	$\rightarrow$	^{3}H + α + 4.78 MeV	$\sigma_{th} = 940b$
^{10}B + n	$\rightarrow$	^{7}Li + α + 2.79 MeV (6%)	$\sigma_{th} = 3838b$
	$\rightarrow$	^{7}Li* + α + 2.31 MeV (94%)	
		$\rightarrow$ ^{7}Li + γ(0.48 MeV)	
^{155}Gd + n	$\rightarrow$	^{156}Gd* $\rightarrow$ ^{156}Gd + γ + e^{-} (29 $-$ 181 keV)	$\sigma_{th} = 61000b$
^{157}Gd + n	$\rightarrow$	^{158}Gd* $\rightarrow$ ^{158}Gd + γ + e^{-} (29 $-$ 181 keV)	$\sigma_{th} = 254000b$
^{235}U + n	$\rightarrow$	fission products + ca. 160 MeV	$\sigma_{th} = 680b$
^{239}Pu + n	$\rightarrow$	fission products + ca. 160 MeV	$\sigma_{th} = 1017b$

Table A.1: Neutron converters and their associated nuclear reactions.

In practice, only the first three elements are commonly used for neutron detectors. During our investigations, we used two different types of UCN detectors, a ^{3}He counter and a fast GEM based detector.

The ^{3}He counters

purchased from Dubna are the today commonly used UCN detectors in the world. Neutrons are detected in the gas detector volume after passing through a 100 μ aluminium window. The gas is a mixture of ^{3}He at 18 mbar, CO_2 at 10 mbar and as much argon as needed to get a total pressure in the detector volume of 1.1 bar. Due to the high neutron capture cross-section of ^{3}He, only little amounts of the gas are needed to obtain a high detection efficiency for UCN.
Besides the high detection efficiency of close to 100% and robustness, the only drawback

of the ^{3}He counter is its poor time resolution which can be explained by the unknown interaction position of the absorbed neutrons inside the gas volume.

Two Cascade-U detectors

are currently in use at the UCN source in Mainz, a one dimensional detector which was used during our first pulsed experiments and a more advanced stand-alone version which, including its own electronics, can be read out directly via USB connection.
Cascade-U stands for Cascade detector for ultracold neutrons [86]. It is a neutron detector using a ^{10}B solid state converter. Customizing the thickness of the converter layer (see also fig.A.2), the Cascade detector reaches detection efficiencies in the range of 90%. The boron layers are vapor deposited on the 100 μm detector entrance foil made of aluminium. After several transmission measurements, which have been done in Mainz, the standard aluminium foil was exchanged by an aluminium magnesium compound (AlMg3) which resulted in a 20% increase of the ultracold neutron transmission and therefore a relative increase of 20% in detector efficiency. α and ^{7}Li particles leaving the boron layer produce ionization tracks while moving through counting gas. By introducing a charge transparent Gas Electron Multiplier (GEM) foil, invented at CERN in 1997, electron clouds from the ionization process can be amplified and accelerated without losses to the detection electrode.
As can be seen in Fig.A.1, the basic substrate of GEM foils is Kapton (50-100 μm thick), that is coated on both sides by a thin layer of copper (5-15 μm thick). The charged particle transparency is garanteed by a regular pattern of through going holes, 50 μm in diameter and at a lattice spacing of about 150 μm. The acceleration of electrons through the GEM onto the detection electrode can be achieved by applying an adequate electrical potential between both copper layers. The electrical fields are formed in such a way, that charges from above the GEM will be channeled and imaged undistorted to below the GEM.

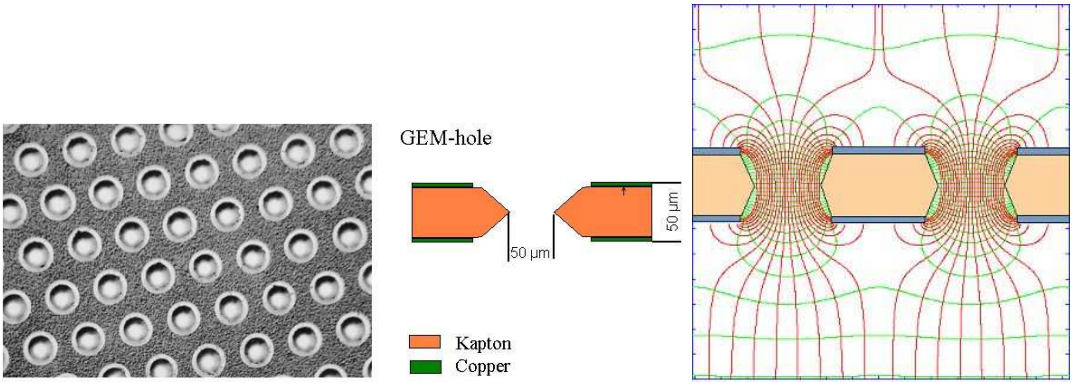

Figure A.1: Left: Hole distribution and geometry of the used GEM foil. Right: Electric field lines close to a hole.

As in the ^{3}He counter, there is CO_2 in the detector, acting as quenching gas.
Together with a standard preamplifier (VV50) developed by the electronic department of the institute of physics in Heidelberg a countrate of 300kHz can be accepted without any dead time problems. A partitioning of the drift electrode in combination with

highly integrated readout electronics can even increase the countrate to the range of a few MHz and allows also a 2D spatial resolution of 1.5cm^2. Additional information about the technical realization can be found elsewhere [86]. The detector is constantly flushed with a gas mixture of argon and CO_2 (with a ratio of 82/18) which is commonly available as welding gas with its brand name Sagox18 .

Working in close collaboration with the neutron detector group of the Institute for Physics in Heidelberg, we investigated the conversion and detection efficiency of ultracold and very cold neutrons for different boron layers and helped therefore to find the optimal coating thicknesses which have been so far only calculated.
The measurements were done at the existing UCN source in Mainz. For velocity dependent determination, the already discussed TOF setup with a flight path of 1500 ± 5 mm was used. The measurements were performed in two consecutive days. For normalization of the obtained Cascade TOF spectra, a TOF spectrum with a standard ^{3}He detector was taken in addition to each Cascade run. Five standard Cascade entrance windows coated with different boron thicknesses (50 nm, 100 nm, 200 nm, 300 nm and 1 μm) had been available and were installed for measurement one after another. After deconvolution of the spectra we obtain the following results.

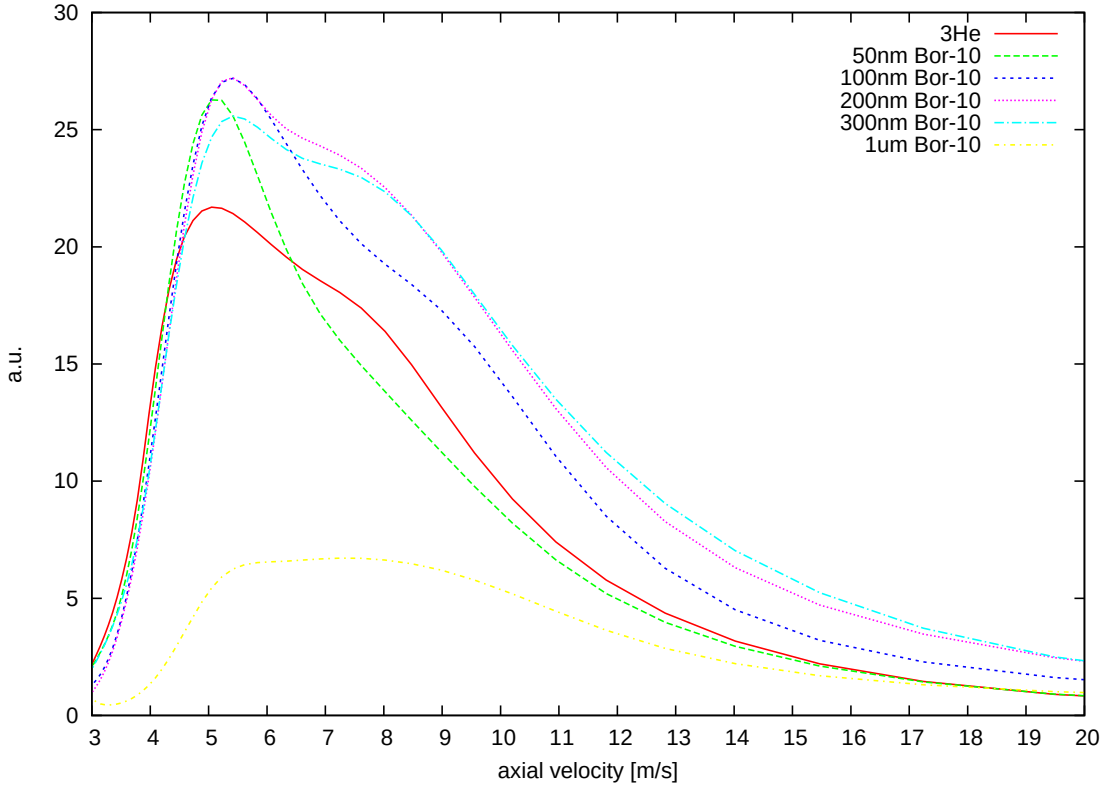

Figure A.2: Time-of-flight spectra measured with different boron layer thicknesses.

As expected from the calculations, the detection efficiency for ultracold neutrons drops down for boron coatings thicker than 300 nm. This result can be explained by the short mean free path of the α and Li decay products in the converter layer. Ultracold neu-

trons up to 6.5 m/s are completely absorbed in the first 100 nm of the boron coating. Indeed, increasing the thickness higher than 200 nm, increases the detection efficiency for faster neutrons (VCN) but also decreases the probability of ultracold neutrons to be counted. It's even possible to customize the boron coating in a way (50 nm) that only ultracold neutrons are detected.
As optimal converter thickness for our purpose we have choosen the preinstalled entrance window with a ^{10}B layer of 200 nm.

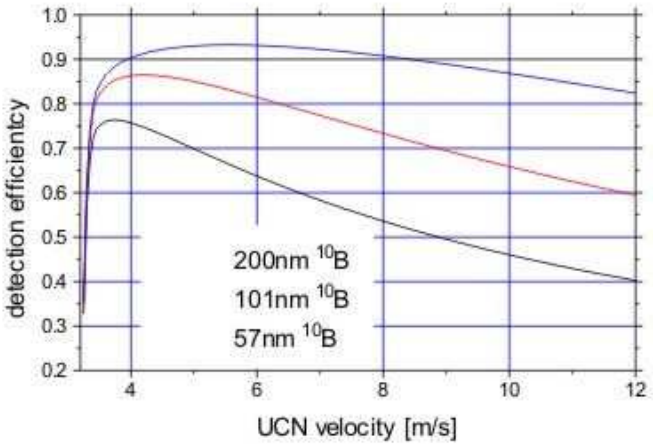

Figure A.3: Calculated absorption of UCN inside ^{10}B layers with different thicknesses .

As already discussed in the previous section about ^{3}He detectors, ^{3}He reaches a theoretical efficiency of close to 100%. Therefore one could think that the Cascade apparent in Fig.A.2 for the optimal boron converter has an efficiency of 120%.
As already explained, the ultracold neutron transmission and hence detector efficiency depends strongly on the used material of the entrance windows. It is conceivable that the entrance window of the ^{3}He counter reduces its efficiency on the order of 20%.

Appendix B

Determination of the chopper characteristics

A time-of-flight chopper can be characterized by two properties which are important for the exact deconvolution of the measured TOF data:

1. The opening function represents the shape of the neutron pulse which exits the chopper disc.

2. The time offset is the delay of the real neutron pulse after the trigger pulse for the data aquisition system

For the time of flight investigations, presented in this thesis, two different disc chopper systems were used:

- A three disc chopper (Fig.B.1) which was developed and built by the UCN group at the Paul Scherrer Institute (PSI) [50].
- A single disc chopper (Fig.B.1) which was built by J.Zenner during his diploma thesis in Mainz [53].

The characterization of both chopper systems was performed at the UCN source C at the TRIGA Mainz.
In all measurements, the same amount of solid deuterium (4 mol) was used as UCN converter.

B.1 Determination of the offset

Time calibration of the two systems was obtained by comparing

(i) at a given distance the spectra taken at two different chopper frequencies;

(ii) at a given chopper frequency the TOF spectra taken at the two different distances.

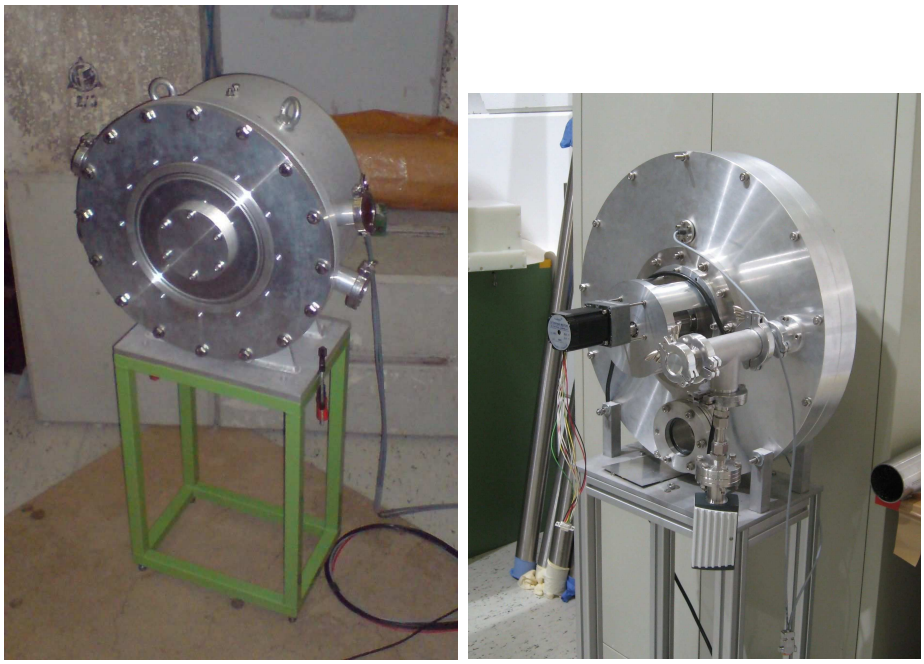

Figure B.1: Choppersystems used for the investigation of a solid deuterium and solid hydrogen UCN source. Left: Three disc chopper of PSI. Right: single disc chopper of Mainz

We obtained eight partially dependent calibration measurements by comparing the TOF spectra at different chopper frequencies, three pairs at each distance: (a)1.00 Hz, 0.75 Hz, (b)1.0 Hz, 0.50 Hz, and (c) 0.75 Hz, 0.50 Hz, and in addition three calibration measurements (one per frequency) by comparing the TOF spectra at the two different distances. In all eight TOF spectra, two Gaussians and a flat background were fitted to the data, see, *e.g.*, Fig.B.2. This procedure results in a suitable parametrisation of the experimental data. The χ^2 per degree of freedom of the fits were in all cases between 1.1 and 1.9. These values reflect the rather simplified parameterization of the spectra by two Gaussians.

With the time calibration using different chopper frequencies, *e.g.*, 1.00 Hz and 0.75 Hz at 1.6 m flight path, we find for the time of the first Gaussian peak in the 0.75 Hz data $t+1.33\cdot\delta t = (0.390\pm0.003)$ s and $t+\delta t = (0.330\pm0.007)$ s at 1.00 Hz, cf. Fig.B.2. Here, δt is the time difference between the electronic trigger signal from the chopper and its real opening time [50] for a chopper frequency of 1 Hz. Since the electronic signal is produced by a photoelectric barrier triggered by an interrupter on one of the rotating chopper discs, the value of δt depends on the chopper frequency. The factor 1.33 [=(1 Hz)/(0.75 Hz)] in front of the parameter δt originates from the normalization of δt to 1 Hz. Thus, from the above numbers, we get $0.33 \cdot \delta t = (0.060 \pm 0.0076)$ s and therefore $\delta t = (0.180 \pm 0.022)$ s.

Similar and partially more precise values for δt are obtained from new data which was taken for a solid deuterium converter of 6.1 mole. Averaging all available and

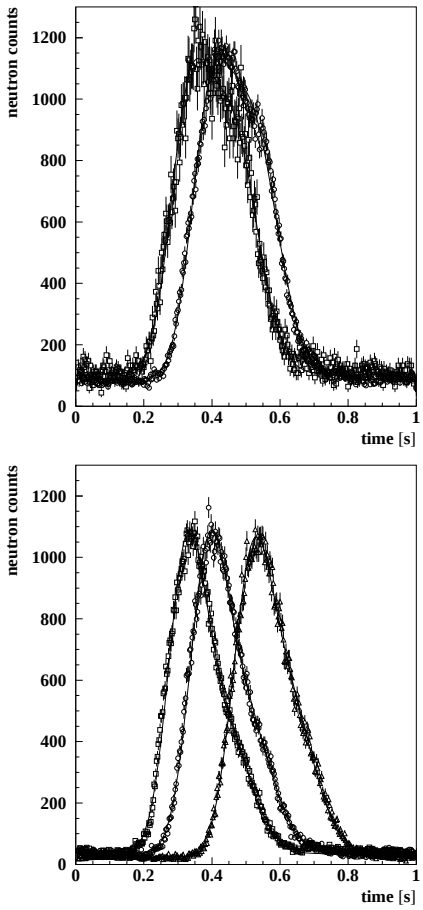

Figure B.2: Time-of-flight spectra obtained with the PSI chopper for a flight path of 1.616 m. Top: converter volume 4 mole, chopper frequencies of 1.00 Hz (open squares) and 0.75 Hz (open circles). Bottom: converter volume 6.1 mole, chopper frequencies of 1 Hz (open squares), 0.75 Hz (open circles) and 0.50 Hz (open triangles). Two Gaussians and a flat background were fitted to each of the data sets (solid lines). The time spectra at different chopping frequencies have to be corrected by a frequency dependent time offset, see text.

independent information we find $\delta t(1\text{Hz}) = (0.191 \pm 0.003)$ s (four independent measurements) from evaluating δt from the different frequencies at the two distances, and $\delta t(1\text{Hz}) = (0.192 \pm 0.007)$ from evaluating at one distance the different frequencies. These values were obtained from a fit with (i) a χ^2 per degree of freedom of 0.7 for the former method, corresponding to a confidence level of 0.45, and (ii) a χ^2 per degree of freedom of 0.3 for the latter method, corresponding to a confidence level of $\sim$0.8.

Using the same methods, J.Zenner obtained for the single disc chopper an offset of $\delta t(1\text{Hz}) = (0.11 \pm 0.03)$ s [53].

B.2 Measurement of the opening function

The opening function can be measured by driving the chopper disc with a very low frequency (few mHz) and using a short flight path (20cm) to the detector. By keeping the neutron travelling time shorter than the chopper disc speed, it is possible to take a neutron "image" of the rotating chopper disc. For example, Fig.B.3 shows the measured opening function of the single disc chopper (Mainz) as a function of time. The similar measurement of the PSI chopper opening function can be found elsewhere [50, 87].
The parameters of the analytical opening functions, described in [53], were fitted with a $\chi^2 = 1.29$.

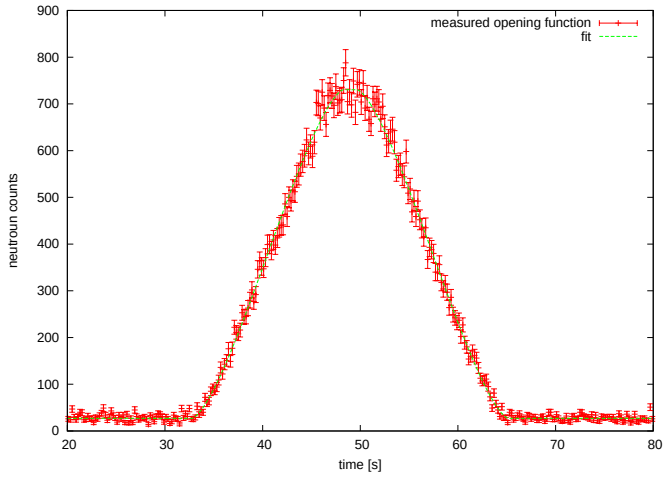

Figure B.3: Measured opening function of the Mainz single disc chopper.

Appendix C

Deconvolution of the time of flight data

The deconvolution of the TOF spectra and the conversion into velocity distributions was performed in two steps.

In the first step, we deconvoluted the measured data by a recursive deconvolution method based on a *mathematica* routine [85]. Before starting the deconvolution process, an analytical description of the measured data is of importance. Besides the use of standard two Gauss fits, which worked for several cases in the framework of this thesis, there should also a more general description be mentioned. This general description of the measured TOF spectra makes use of a cubic spline fuction based on nine supporting points (a_x) and a constant background (b), see for example Fig.C.1.

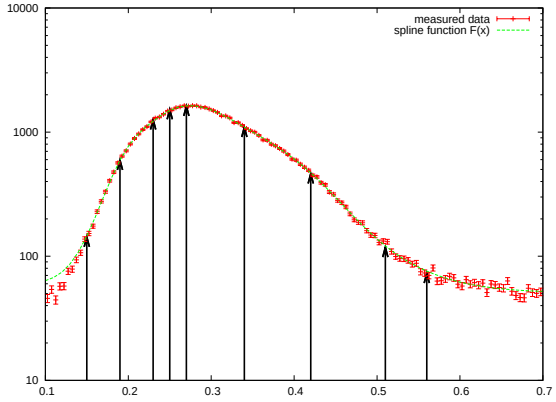

Figure C.1: Analytical description of the measured data by a cubic spline function using 9 supporting points (arrows). Background constant $b = 51$ is not visualized.

This analytical expression $F(x)$ is then convoluted with the chopper opening function via

$$G(x) = \int F(x - x_0) \cdot Openf(x_0)\ dx_0 \tag{C.1}$$

Using the standard least square fitting technique $G(x)$ including the nine supporting points is varied until we obtain a minimal chi-square. After substraction of the measured offset δt we obtain a deconvoluted TOF spectrum $F(x)$, which convoluted with the opening function of the used chopper represents the measured data.
The data represent the neutron event distribution dN/dt.
In order to obtain a velocity distribution dN/dv_{p} parallel to the guide axis, we perform a second step:

(i) we multiply the data with the derivative $|dt/dv_{\mathrm{p}}| = t^2/d$, where d is the flight path
(ii) we convert the TOF axis to $v_{\mathrm{p}} = d/t$.

Appendix D

Monte Carlo simulations with MCNP, prediction of the UCN production in solid deuterium

To understand the measured results at the prototype UCN source, chap.4.3.2, two steps had to be done.

1. Description of the neutron flux and its spectral distribution inside the converter cup

2. Description of of loss channels of the produced ultracold and very cold neutrons on their way from the production point to the detector.

In chap.2.3.1 the downscattering cross section for neutrons inside the converter material, including some first predictions of production are given. As can be deduced from Fig.2.4, a calculation based on eqn.2.21 depends strongly on the initial neutron spectrum $\frac{d\Phi}{dE_0}$. Hence, to understand the behaviour of the neutron spectrum inside the converter (premoderation effect), Monte Carlo simulations in steps of 1mol solid deuterium were performed with the standard particle tracking code of *MCNP 4.2*. This way it was possible to estimate the neutron fluxes and the spectral distribution inside beamport C and D of the reactor TRIGA Mainz.
Starting with the first simulations, which have been performed by Yury Pokotilovsky, who implemented the actual realistic three dimensional reactor model (Fig.D.1) of the TRIGA Mainz in *MCNP*, the model was extended with a more realistic geometry of the frozen converter. As can be seen in Fig.D.1, this geometry file includes all necessary reactor installations in a rather simplified geometry. The neutron and gamma cross sections for the implemented materials especially the deuterium and also hydrogen were taken from the standard library files. Unfortunately, due to the not usual application of solid hydrogen and its isotopes, only cross sections for the liquid states have been available. Refering to [**?**], where extensive studies of cold, very cold and ultracold neutron spectra for both solid and liquid deuterium are presented, we estimate an error of 20% for the MCNP simulation results achieved with the cross section of liquid hydrogen and deuterium.

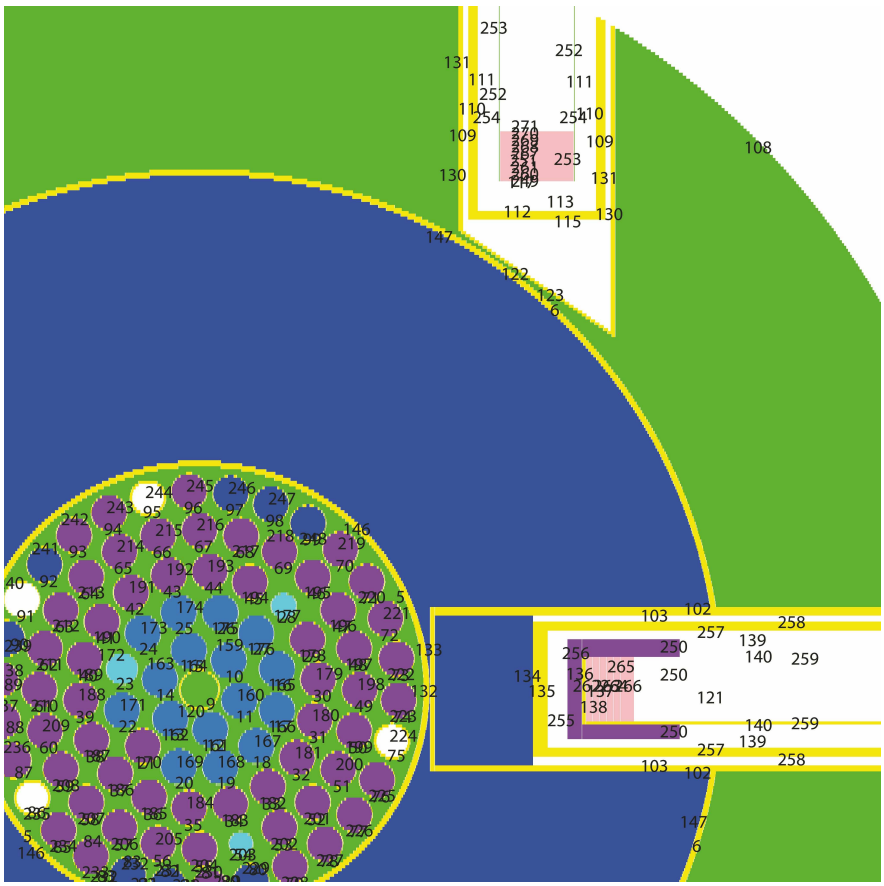

Figure D.1: Cut through the 3D realistic reactor model of the reactor TRIGA Mainz under MCNP. The numbers in the picture represent the partnumbers of each geometric element implemented in the code.

Therefore, all final calculation can be understood as a first estimation of the premoderation of the thermal neutrons inside the solids UCN converters.
Reliable criticality simulations are of course time consuming. To obtain reasonable results in a tolerable computing time (office computer), 4000 single tracking runs were performed for each source configuration.

Results of the MCNP calculations

Starting with the empty beamports, the thermal neutron fluxes have been calculated. To achieve some reliability of the implemented model, these results have been compared with experimentally determined thermal neutron data measured via neutron activation of gold. Within an error of 10% the measured and the simulated fluences are in good agrement with each other.
Based on this calculation, it is possible to analyze the thermal neutron spectrum for the empty beamport C. Fitting a standard Maxwell distribution using eqn.2.18, we obtain a neutron temperature of 350K which is sligthly higher than the moderator temperature.

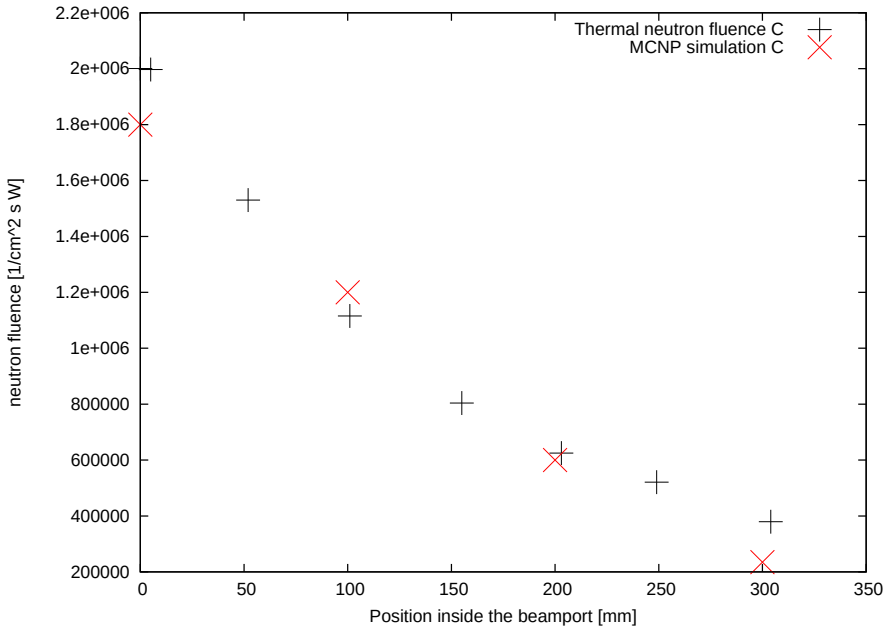

Figure D.2: Measured and simulated thermal (black points) neutron fluence normalized for 1 W reactor power as a function of the distance d from the front end (nose) of the beamtube C. The errors of the measurement are about 5%.

MCNP calculation of neutron premoderation in solid deuterium

To investigate the spectral change of the initial neutron spectrum inside the solid deuterium, the converter cup of beamport C was divided in 7 discs with a thickness of 7mm, each corresponding to 1mol of solid deuterium with a density of $0.2 g/cm^3$. Starting from 1mol, seven independent simulation runs (1mol steps) have been performed up to the maximal reachable quantity of 7mol. Due to the finite geometry of our solid deuterium crystal and the large scattering length of thermal neutrons inside deuterium ($\approx$ 5cm), the premoderation of the neutron spectrum is not completed and has to be described by the sum of two Maxwellian distributions.

$$\frac{d\Phi}{dE} = A1 \cdot \frac{E}{(k_B T_1)^2} \cdot e^{-\frac{E}{k_B T_1}} + A2 \cdot \frac{E}{(k_B T_2)^2} \cdot e^{-\frac{E}{k_B T_2}} \tag{D.1}$$

Analysing the neutron spectra inside each mol of solid deuterium (up to a crystal size of 7 mol), we obtain for beamport C 28 spectram, presented in the following table:

With the help of these fit parameters (tab.D.5), it was possible to calculate according to eqn.2.22 the final production of ultracold (E_{kin}<190neV) and very cold neutrons for the crystals between 1 and 7mol (in 1mol steps). In contrast to the mentioned debye approximation, used for the description of the phonon density of states in chap.2.3.1, a more realistic density of states model, based on the measured neutron dispersion curve from Nielsen [27] was implemented.

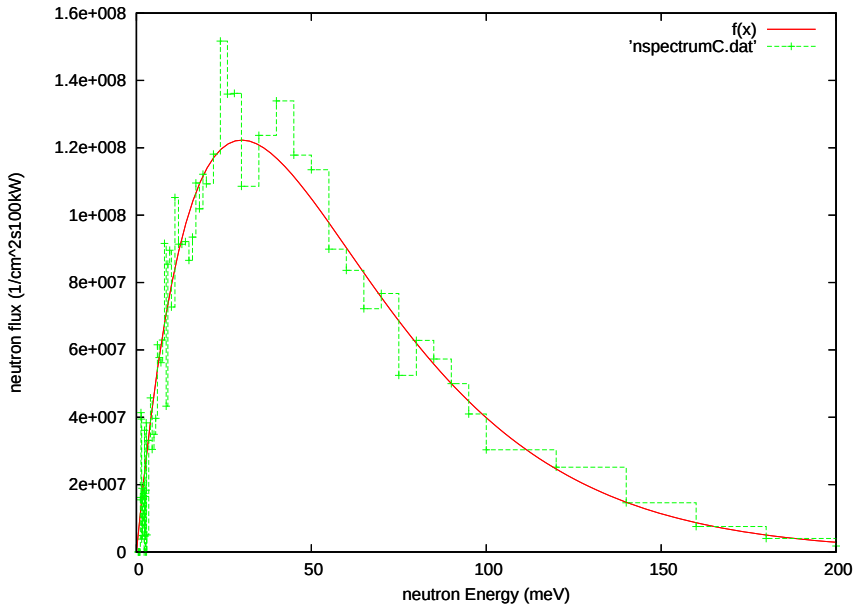

Figure D.3: Calculated neutron spectrum (green points) of beamport C at the deuterium position. For the fit, a Maxwell Boltzmann distribution was used

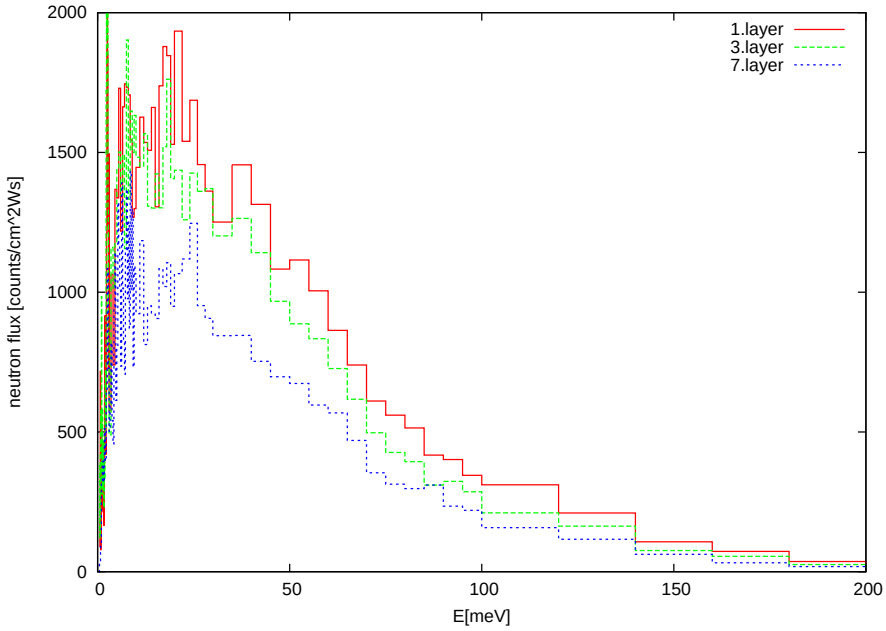

Figure D.4: Neutron spectra for 3 different layers inside a 7mol crystal.

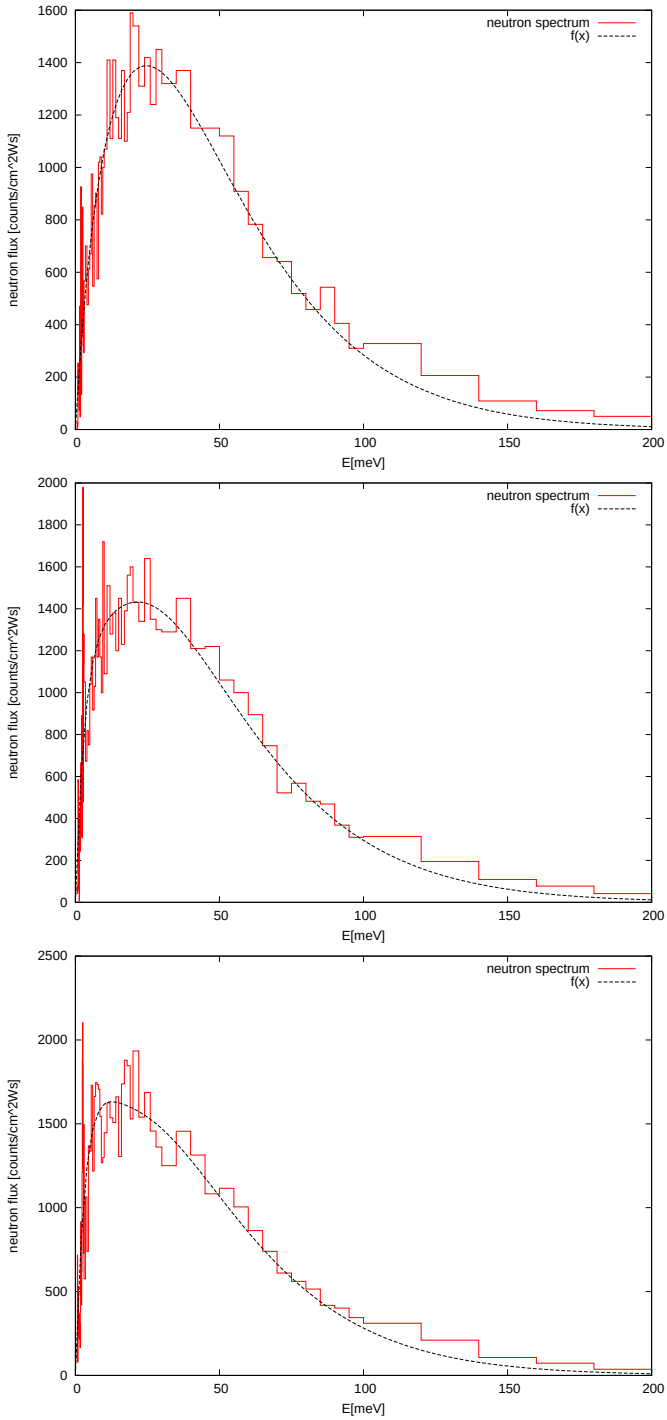

Figure D.5: Change in neutron temperature inside the first 7mm of solid deuterium with increasing amount of sD_2. Upper plot: 1mol solid deuterium. Center plot: 3mol solid deuterium. bottom plot: 7mol solid deuterium.

Table D.1: Fit parameters of the neutron spectra inside solid deuterium

	A1	T1	A2	T2
1mol:	142.8	293.5	4.27	61.8
2mol:				
1.mol:	166	282	172	36
2.mol	130.5	302	4.27	80
3mol:				
1.mol:	147.9	296.8	25.6	55.6
2.mol	153.1	282.3	310	40
3.mol	151.8	270.5	158.2	40.7
4mol:				
1.mol:	164	283	345.5	38
2.mol	157	275	367.5	31.5
3.mol	143	277	354	48.5
4.mol	151	258	685	35
5mol:				
1.mol:	159	285	492	44
2.mol	175	264	699	37
3.mol	161	265.6	665	33.3
4.mol	141	271	676	34.7
5.mol	117	284	524	33.2
6mol:				
1.mol:	178	279	474	45
2.mol	179	263	776	37
3.mol	163	266.6	592	42
4.mol	145	273	761	39
5.mol	127	279	616	41
6.mol	119	275	545	35.7
7mol:				
1.mol:	161	287	376	60
2.mol	151	283	465	58
3.mol	158	268.6	580	46.1
4.mol	151	263.7	544	44.3
5.mol	148	256	518	43.7
6.mol	113	280	340.5	58
7.mol	100	286	255.7	62.8

Appendix E

Monte Carlo simulations of a realistic source model, prediction of UCN transmission

For the analysis of the measured TOF data, a Monte Carlo model of the UCN source C was developed. This C code allowed us to simulate the energy dependent transport meachnism of slow neutrons from the production position inside the converter to the detector. The geometrical model of the UCN source for Monte Carlo simulation includes the following parts:

- the converter cup with internal length 60 mm attached to
- the source neutron guide with length 3.5 m (everywhere the internal diameter of neutron guides and cross-sections for neutrons passage is equal to 66 mm);
- The source neutron guide ends with an aluminium foil of 100μm thickness followed by a straight section with a length of 46 cm ;
- This neutron guide section ends with a 45 degrees bent to which a time-of-flight spectrometer is connected.

Ultra- and very cold neutrons can be created inside the solid deuterium converter in the velocity range from 0.01 to 20 m/s. The neutron intensity increases quadratically with velocity. The angular distribution inside the solid is set isotropic. The initial creation positions are homogeniously distributed inside the converter volume.
Elsewhere, inside the source, including the converter the neutron trajectories are built with parabolic increment corresponding to the movement in the gravitational field of the earth. The accuracy of this method was proven by comparing the results with the trajectories obtained from the solutions of the differential equations of motion for given initial parameters using the Runge-Kutta 4th integration method [88] (additionally the energy conservation law is controlled).

Simulation parameters of the converter

Inside the converter, e.g., solid deuterium the program takes all losses into account which have been already mentioned in chap.2.3.2

- neutron absorption on a deuterium atom
- capture and upscattering on hydrogen contamination
- upscattering on ortho- and para- deuterium
- incoherent and elastic scattering.

The corresponding cross-sections are used to calculate the mean free paths of ultracold and very cold neutrons inside solid deuterium. The actual neutron path length is simulated in accordance to the distribution $\sim exp(-l/L_{mfp})$, where L_{mfp} is a cumulative mean free path. In the case of neutron loss, the process of neutron creation is repeated with new initial parameters and position.
In the case of elastic scattering on the lattice, an isotropic scattering law simulates prolonged trajectories with new direction angles. Finally, when the neutron reaches the converter-vacuum boundary, the quantum reflection probability, refraction and Fermi potential acceleration, see also sect.4.2, are calculated and applied to the continuing trajectory.

Simulation parameters outside the converter

The interaction of neutrons escaping from the converter with the walls of the neutron guide is simulated by standard specular and diffusive reflection laws. Diffuse reflection is introduced according to the Knudsen law as next order reflection character for ultracold neutrons, which was considered by [45, ?]. The diffuse reflection parameter of $\sim$ 6% and also the losses per wall collision, $\sim 2 \div 4 \times 10^{-4}$ were taken from [62].
For the neutron transmission through the aluminium separation foil at the end of the neutron guide, several physical aspects like

- multiple quantum reflections
- refraction
- deceleration on the Fermi potential of aluminium
- absorption due to capture reaction
- elastic scattering

were taken into account.

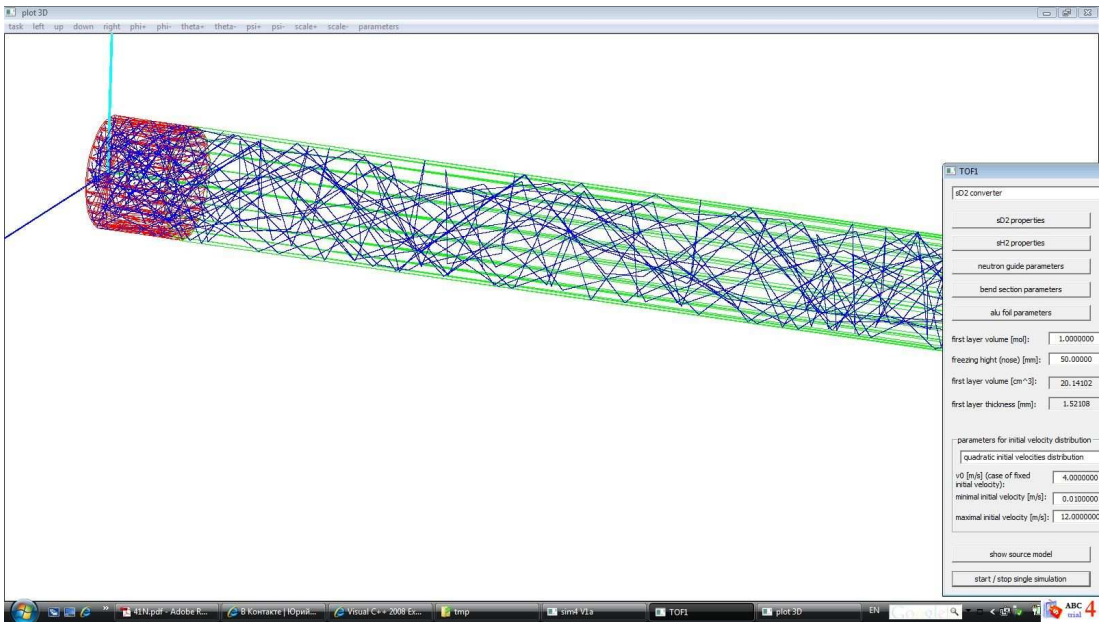

Figure E.1: Picture of the 3 dimensional visualization of the neutron tracking during simulation. For example only the converter part (red) and a short guide piece (green) are shown.

The TOF setup

Just before the TOF spectrometer, neutrons are deflected with a 45 degree bent section out of the thermal neutron beam. In order to simulate the neutron transmission through a bent section, the bent section was simplified as a part of a torus. Unfortunately, it turned out that the code could not reproduce the very cold neutron transmission of our conventionally used stainless steel bents.
This discrepancy was finally attributed to the not adequate model of neutron transmission through a stainless steel bent section, which is mainly dominated by the unknown inner surface roughness. Attempts to describe the scattering of neutrons using some realistic macroscopic waviness and introducing a Debye-Waller factor for wall quantum reflection were not successful.
Therefore, an artificial "blackness" factor for very cold neutron transmission was implemented in the code.
Further experimental work confirmed the assumption of large losses for very cold neutrons. By comparing TOF spectra (Fig.E.2), obtained with our conventionally used stainless steel bents and specially prepared bent sections made from glass, see sect 7.29, the working principle of the Monte Carlo transport code could be succesfully proven.

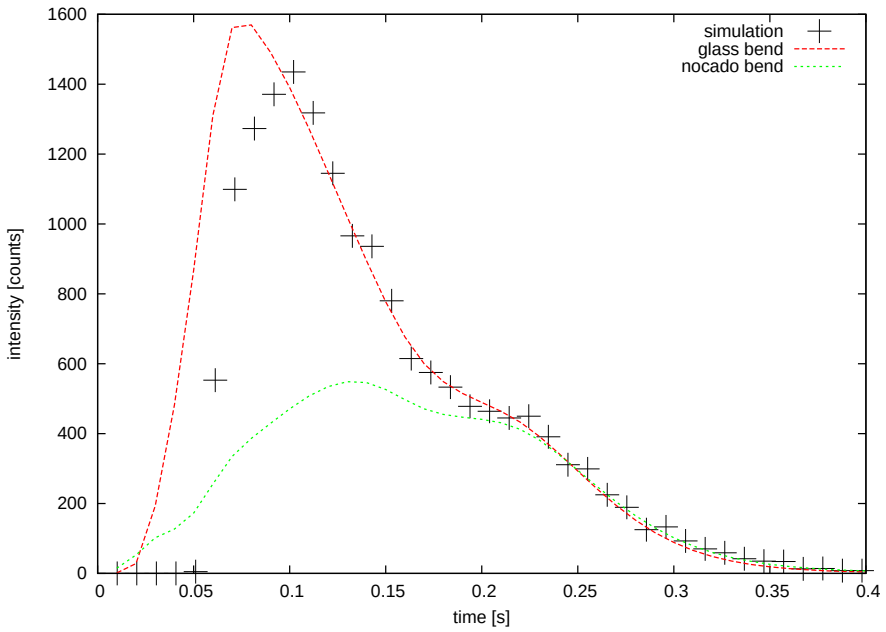

Figure E.2: Comparison of two measured time-of-flight spectra (red: with glass bent, green: with nocado bent) with a time-of-flight spectrum simulated with the implemented Monte Carlo transport code. For the simulation, the neutron intensity was quadratically increased with velocity up to a maximal velocity of 20m/s. Higher velocities need a further improvement of the tracking code and are also not of interest.

Bibliography

[1] Ya.B.Zel'dovich,Sov.Phys.JETP 9,1389(1959)

[2] V.I.Lushikov et.al., JETP Letters 9,23 (1969)

[3] A. Steyerl, Physics Letters B 29, 33–35 (March 1969).

[4] R. Golub and J. M. Pendlebury Physics Letters A 62, 337–339 (September 1977).

[5] A. Steyerl. NIM 125, 461–469 (April 1975).

[6] A. Steyerl, et.al., Phys.Lett. A 116, 347 (1986).

[7] P. G. Harris, et.al, Nucl. Instr. and Meth. A 440, 479-482, (2000)

[8] K. F. Smith, et.al, Physics Letters B, 234, 1-2, 191-196, (1990)

[9] A. Pichlmaier, et.al, Nucl. Instr. and Meth. A, 440, 3, 517-521, (2000)

[10] A. Serebrov, et.al, Physics Letters B, 605, 1-2, 72-78, (2005)

[11] H. Abele, et.al, Nucl. Phys. A, 827,1-4, 593-595, 15 August 2009

[12] K.Bodek, et.al, Nucl. Instr. and Meth. A, Available online 5 August 2009

[13] A. Anghel, et.al, Nucl. Instr. and Meth. A, doi:10.1016 (2009)

[14] C. Y. Liu, et.al., APS Meeting Abstracts pages 210 (October 1998).

[15] A. Saunders, et.al.,Physics Letters B 593, 55–60 (July 2004)

[16] U.Trinks, Nucl. Instr. and Meth. A 440 p.666-673 (2000)

[17] Y. Masuda, et.al., Physical Review Letters 89, B4801+ (December 2002).

[18] C. A. Baker, et.al., Physics Letters A 308, 67–74 (February2003).

[19] Ph. Schmidt-Wellenburg, Production of ultracold neutrons in superfluid helium under pressure, Thesis 2009.

[20] H. Abele, Progress in Particle and Nuclear Physics 60 (2008) 1–81

[21] H. Abele, et.al, Phys. Rev. Lett. 88, 211801 (2002)

[22] I.Altarev, et.al, Phys. Rev. Let. 100, 014801 (2008)

[23] V.F. Ezhov, Nucl. Instr. and Meth. A, Available online 6 August 2009

[24] K.-J. Kügler, et.al, Nucl. Instr. and Meth. A, 228, 2-3, 240-258, (1985)

[25] Yu.N. Pokotilovski, et.al, Physica B: 403, 10-11, 1942-1948, 1 May 2008

[26] Z.Ch. Yu, et.al., Z.Phys.B 62, 137-142(1986).

[27] M. Nielsen, Phys. Rev. B 7, 1626 - 1635 (1973)

[28] A.Frei, Produktion von ultrakalten Neutronen mit einem festen Deuteriumkonverter, Thesis 2008

[29] C.-Y. Liu, A. R. Young, and S. K. Lamoreaux, Phys. Rev. B 62, R3581 - R3583 (2000).

[30] Yu.N. Pokotilovski, Nucl. Instr. and Meth. A 356, p. 412 (1995)

[31] H. Menke, N. Trautmann, W.-J. Krebs, Kerntechnik 17, No. 6 (1975).

[32] A.Schwab, Diploma thesis 2010

[33] I. F. Silvera, Rev. Mod. Phys. 52, 393 (1980).

[34] K. Bodek et.al, Nucl. Instr. Methods A 533 (2004) 491.

[35] C. Y. Liu, et.al, Nucl. Instr. Methods A 508 (2003) 257

[36] A.R.Müller, Characterization of solid D2 as source material for ultra cold neutrons and development of a detector concept for the detection of protons from the neutron decay, Thesis 2008.

[37] M. Prager, H. Grimm, I. Natkaniec, Phys. Chem. 7, 2587 (2005).

[38] C. L. Morris, et.al, Phys. Rev. Lett. 89, 272501-1 (2002).

[39] G. Ljungdahl and S. W. Lovesey,Phys. Script. 53, 734 (1996).

[40] E. Fermi and L. Marshall, Phys. Rev. 71, 666 (1947).

[41] A. Steyerl, H. Vonach,Z. Physik 250, 166 (1972).

[42] H. Rauch, et.al,Phys. Rev. Lett. 83, 4955 (1999).

[43] J. Felber, R. Gähler, R. Golub, Phys. Rev. Lett. 85, 5667 (2000).

[44] F. Atchison, B. Blau, M. Daum, P. Fierlinger et al.,Phys. Rev. C 74, 055501 (2006).

[45] V. K. Ignatovich, The Physics of Ultracold Neutrons,Oxford Series of Neutron Scattering in Condensed Matter·5, Clarendon Press, Oxford (1990).

[46] Z-Ch. Yu, S. S. Malik, R. Golub, Z. Phys. B 62, 137 (1986).

[47] F. Atchison, B. Blau, M. Daum, P. Fierlinger et al.,Nucl. Instr. and Meth. in Phys. Res. B 260, 647 (2006).

[48] Private communication with Peter Geltenbort (PSI, 2007)

[49] I. Altarev *et al.*, Nucl. Instr. and Meth. in Phys. Res. A578 (2007) 450.

[50] P. Fierlinger *et al.*, Nucl. Instr. and Meth. in Phys. Res. A 557, 572 (2006).

[51] F. Atchison *et al.*, Phys. Lett. B 642, 24 (2006).

[52] F. Atchison *et al.*, Nucl. Instr. and Meth. in Phys. Res. B 260, 647 (2007).

[53] J. Zenner, Konstruktion und Test eines Setups zur Polarisation ultrakalter Neutronen , Diploma Thesis 2009.

[54] S. K. Lamoreaux, R. Golub, J. Phys. G: Nucl. Part. Phys. 36 (2009)

[55] R. W. Pattie, Jr., et.al, Phys. Rev. Lett. 102, 012301 (2009)

[56] F. Atchison, et.al, Nucl. Instr. and Meth. in Phys. Res. A, Available online 5 August 2009

[57] F. Schmidt, Phys.Rev. B 10, 10 (1974)

[58] F. J. Webb, et.al, Nucl.Sci.Eng., 9, 120 (1961)

[59] R. G. Bohn, C. F. Mate, Phys. Rev. B 2, 2121 - 2126 (1970)

[60] M. Meister, Aufbau eines Sputterlabors und Herstellung von Leitern ultrakalter Neutronen, Diploma Thesis 2009

[61] W. Schmid, Erzeugung ultrakalter Neutronen in einem festen Deuteriumkonverter, mastersthesis 2005

[62] I. Altarev *et al.*, Eur. Phys. J. A37 (2008) 9.

[63] H. Frey, R. Haefer, Tieftemperaturtechnologie, VDI Verlag, 1981

[64] R. E. MacFarlane, Cold moderator scattering kernel methods,Form 836, Los Alamos National Laboratory, 10/1996

[65] T. Mitsuyasu, et.al, Nucl. Instr. and Meth. in Phys Res. A 537 610–613 (2005)

[66] S. Grieger et al., J. Chem. Phys. 109 (1998), p. 3161

[67] J. R. Granada, et.al, Nucl. Instr. and Meth. in Phys Res. B 256 164-172 (2008)

[68] D. Evans, Cryogenics 35, 163-166 (1995)

[69] E. Fermi, Ricerca Scientifica 7 (1936) 13.

[70] M. Keunecke *et al.*, Thin Solid Films 398-399 (2001) 142.

[71] X. Jiang *et al.*, J. of Appl. Phys. 93 (2003) 1515.

[72] G. Lehmann *et al.*, Appl. Phys. A: Materials Science & Processing, 74 (2002) 41.

[73] http://www.ncnr.nist.gov/resources/n-lengths/

[74] K. Yamamoto *et al.*, Surface and Coatings Technology 142-144 (2001) 881.

[75] K. Yamamoto *et al.*, Thin Solid Films 377-378 (2000) 331.

[76] http://www.n-cdt.com

[77] Private communication with Ulrich Schmidt (Heidelberg, 2007)

[78] A. Steyerl, Z. Physik 254 (1972) 169.

[79] A. Steyerl, Z. Physik **252**, 371 (1972).

[80] F. Atchison *et al.*, Nucl. Instr. and Meth. in Phys. Res. B260 (2007) 647

[81] V. Sears, Neutron News 3 (1992) 29.

[82] The Particle Data Group, Phys. Lett. B592 (2004) 14.

[83] A. H. Rosenfeld, Ann. Rev. Nucl. Sci. 25 (1975) 555.

[84] K. Sköld, Nucl. Instr. and Meth. 63, 1 (1968), p.114-116

[85] Private communication Dr.Ulrich Schmidt, Physikalisches Institut Heidelberg (June 2009)

[86] http://www.physi.uni-heidelberg.de/Forschung/ANP/Cascade

[87] L. Goeltl-Simmenauer, Measurements and Procedures for the Construction and Characterization of Ultra-Cold Neutron Guides, Diploma Thesis 2008

[88] E. Hairer, S. P. Norsett, G. Wanner: Solving Ordinary Differential Equations I, Springer Verlag